# Additive Manufacturing of
# 3D Nano-Architected
# Metals and Ceramics

Thesis by

Andrey Vyatskikh

In Partial Fulfillment of the Requirements for

the degree of

Doctor of Philosophy

Caltech

CALIFORNIA INSTITUTE OF TECHNOLOGY

Pasadena, California

2020

(Defended  May 6th, 2020)

Andrey Vyatskikh
ORCID: 0000-0002-6917-6931

# ACKNOWLEDGEMENTS

# ABSTRACT

Additive manufacturing (AM) represents a set of manufacturing processes that create complex 3D parts out of polymers, metals, and ceramics. AM of metals and ceramics is widely used to produce parts for aerospace, automotive, and medical applications. At the micro- and nano-scales, AM is poised to become the enabling technology for efficient 3D microelectromechanical systems (MEMS), 3D micro-battery electrodes, 3D electrically small antennae, micro-optical components, and photonics. Today, the minimum feature size for most commercially available metal and ceramic AM is limited to ~20-50 μm. Currently, no established processes can reliably produce complex 3D metal and ceramic parts with sub-micron features.

In this thesis, we first demonstrate a nanoscale metal AM process that can produce ~300 nm features out of nanocrystalline, nanoporous nickel using synthesized hybrid organic-inorganic materials, two-photon lithography, and pyrolysis. We study microstructure and mechanical properties of as-fabricated nickel architectures and compare their structural strength to established AM processes. We then show how this process can be extended to other metals and metalloids, including Mg, Ge, Si, and Ti.

This study extends further into nanoscale AM of transparent, high refractive index materials for micro-optics and photonic crystals. We develop an AM process to 3D print fully dense nanocrystalline rutile titanium dioxide ($TiO_2$) with feature dimensions down to ~120 nm. We carefully study and model the relationship between feature dimensions and process parameters to achieve a <2% variation in critical dimensions. We then use this

understanding of the process to fabricate and study 3D dielectric photonic crystals with a full photonic bandgap in the infrared.

Finally, a microscale AM process of titanium dioxide is demonstrated for photocatalytic water treatment. We show how synthesized hybrid organic-inorganic materials can be applied for stereolithography to print $TiO_2$ architectures with 100 μm features. We use the developed 3D printing process to investigate the effect of 3D architecture on the efficiency of photocatalytic water treatment.

This work establishes a versatile and efficient pathway to create three-dimensional nano-architected metals and ceramics and to investigate their properties for applications in 3D MEMS, micro-optics, photonics, and photocatalysis.

# PUBLISHED CONTENT AND CONTRIBUTIONS

Chapter 2 and Chapter 3 have been adapted, in part, from:

(1)     **A. Vyatskikh**, S. Delalande, A. Kudo, X. Zhang, C.M. Portela, J.R. Greer, Additive manufacturing of 3D nano-architected metals, Nat. Commun. 9 (2018) 593. doi:10.1038/s41467-018-03071-9.

(2)     **A. Vyatskikh**, S. Delalande, J.R. Greer, *Additive Manufacturing of Architectured Materials*, U.S. Patent. No. US15/719,338, Assignee: Caltech

Contributions: performed material synthesis, photopolymer formulation, TPL fabrication, pyrolysis, SEM, EDS, morphology characterization, part of nanocompression experiments and analysis, and wrote the manuscript

Chapter 4 has been adapted, in part, from:

(3)     **A. Vyatskikh**, R.C. Ng, B. Edwards, J.R. Greer, Additive manufacturing of titanium dioxide for dielectric photonic crystals, in: Proc.SPIE, 2019. https://doi.org/10.1117/12.2507076.

(4)     **A. Vyatskikh**, R.C. Ng, B. Edwards, J.R. Greer, Additive Manufacturing of High Refractive Index, Nano-architected Titanium Dioxide for 3D Dielectric Photonic Crystals, Nano Lett. 20 (2020) 3513–3520. doi:10.1021/acs.nanolett.0c00454.

Contributions: performed material synthesis, photopolymer formulation, TPL fabrication, pyrolysis, SEM, EDS, morphology characterization, modeling of voxel dimensions and experimental validation, ANOVA of geometric dimensions, FTIR spectroscopy, and wrote the manuscript

Chapter 5 has been adapted, in part, from:

(5)     **A. Vyatskikh**, A. Kudo, S. Delalande, J.R. Greer, Additive manufacturing of polymer-derived titania for one-step solar water purification, Mater. Today Commun. 15 (2018) 288–293. doi:10.1016/j.mtcomm.2018.02.010.

Contributions: performed material synthesis, photopolymer formulation, SLA fabrication, pyrolysis, SEM, EDS, morphology characterization, analysis of mechanical data, and wrote the manuscript

Not directly adapted in this thesis:

(6)     X. Zhang, L. Zhong, A. Mateos, A. Kudo, **A. Vyatskikh**, H. Gao, et al., Theoretical strength and rubber-like behaviour in micro-sized pyrolytic carbon, Nat. Nanotechnol. (2019). doi:10.1038/s41565-019-0486-y.

(7)     X. Zhang, **A. Vyatskikh**, H. Gao, J.R. Greer, X. Li, Lightweight, flaw-tolerant, and ultrastrong nanoarchitected carbon, Proc. Natl. Acad. Sci. (2019) 201817309. doi:10.1073/pnas.1817309116.

(8)     C.M. Portela, **A. Vyatskikh**, and J.R. Greer, *Fabrication and Design of Composites with Architected Layers*, U.S. Patent No. 16/206,163, Assignee: Caltech.

(9)     J.R. Greer, **A. Vyatskikh** et al., *Three-Dimensional Architected Pyrolyzed Electrodes for Use in Secondary Batteries and Methods of Making Three-Dimensional Architected Electrodes,* U.S. Patent No. 16/151,186, Assignee: Caltech.

# TABLE OF CONTENTS

# LIST OF ILLUSTRATIONS

# LIST OF ABBREVIATIONS

| | |
|---|---|
| **AANR** | All-angle negative refraction |
| **AFSM** | Additive friction-stir manufacturing |
| **AM** | Additive Manufacturing |
| **ANOVA** | Analysis of variance |
| **DED** | Directed Energy Deposition |
| **DIW** | Direct ink writing |
| **DLP** | Digital Light Processing |
| **DLW** | Direct laser writing |
| **DMLS** | Direct Metal Laser Sintering |
| **EBF3** | Electron Beam Freeform Fabrication |
| **EBM** | Electron Beam Melting |
| **EDS** | Energy-Dispersive X-Ray Spectroscopy |
| **EFAB** | Electrochemical fabrication |
| **EHD** | Electrohydrodynamic fabrication |
| **ET** | Exposure Time |
| **FCT** | Face-centered tetragonal |
| **FDM** | Fused Deposition Modeling |
| **FFT** | Fast Fourier Transform |
| **FIBID/FEBID** | Focused ion/electron beam-induced deposition |
| **LENS** | Laser Engineered Net Shaping |
| **LIFT** | Laser-induced forward transfer |
| **LP** | Laser Power |
| **MEMS** | Microelectromechanical systems |
| **PDF** | Powder Bed Fusion |
| **PhC** | Photonic crystal |
| **PWE** | Plane Wave Expansion |
| **ROS** | Reactive oxygen species |
| **RPD** | Rapid Plasma Deposition |
| **SEM** | Scanning Electron Microscopy |
| **SLA** | Stereolithography apparatus |
| **SLS** | Selective Laser Sintering |
| **SODIS** | Solar disinfection of drinking water |
| **TCE** | Transparent conductive electrode |
| **TEM** | Transmission Electron Microscopy |
| **TPL, 2PL** | Two-photon lithography |
| **UC** | Ultrasonic Consolidation |
| **FTIR** | Fourier Transform Infrared Spectroscopy |

# CHAPTER 1 : INTRODUCTION AND STATE-OF-THE-ART

**Introduction**

Additive manufacturing (AM) represents a set of processes that enable layer by layer fabrication of complex 3D structures using a wide range of materials that include ceramics [1], polymers [2], and metals [3]. Metal AM has revolutionized the production of complex parts for aerospace, automotive and medical applications [4,5]. Light and strong titanium parts made by Rapid Plasma Deposition (RPD) are being implemented in modern aircrafts [4]. Joints in hip replacements, called acetabular cups, are widely produced using electron beam melting (EBM), which allows for incorporation of a porous shell that improves bone tissue growth into the implant, i.e. osseointegration [5]. The search for optimal application- and material-specific methods has given rise to dozens of commercially available AM processes. We provide a brief overview in Established AM processes section of this chapter.

Today's resolution of most commercially available metal and ceramic AM processes is limited to ~20-50 μm [6]; printing 3D features below these dimensions is technically challenging [7]. Many unique phenomena arise in metals with micro- and nano-dimensions, e.g. light trapping in optical meta-materials [8] and enhanced mechanical resilience [9–15]. Accessing these phenomena requires developing a process to fabricate 3D metallic and ceramic architectures with macroscopic overall dimensions and individual constituents in the sub-micron regime (see Significance of micro- and nanoscale AM of metals and ceramics for a detailed discussion). To understand strategies

in developing new nanoscale AM processes we first provide a very brief description of AM processes that are commercially available today.

**Established AM processes**

Precursor technologies to AM date back to the end of the 19th century with works in 3D photosculpture by François Willème in 1860 [16] and to the introduction of laminated manufacturing for topography visualization by Joseph Blanther in 1892 [17]. Modern history of AM began in 1987 with introduction of SLA-1, the first commercially available AM machine by 3D Systems [18]. Since then, dozens of AM processes have been adopted by the industry for prototyping and manufacturing of polymer, metal, and ceramic parts [1–3]. These include parts for automotive, aerospace, and medical industries, as well as jewelry, tooling, and even art and museum displays. ISO/ASTM 52900 provides some guidance to the cornucopia of AM processes available today. Specifically, it outlines seven categories of AM processes: material extrusion, binder jetting, sheet lamination, vat photopolymerization, material jetting, directed energy deposition (DED), and powder bed fusion (PBF) (Figure 1.1).

**Material extrusion** (Figure 1.1a) refers to AM processes that selectively dispense a filament material through a nozzle or an orifice, such as Fused Deposition Modeling (FDM) of thermoplastic materials [19]. **Binder jetting** (Figure 1.1f) describes processes that involve selective deposition of a liquid bonding agent onto powder materials to create a green part that can be later sintered together, with examples including Digital Part Materialization [20,21] and Digital Metal [6,22]. **Sheet lamination** (Figure 1.1e) describes layer-by-layer

bonding of sheets of material to create a 3D object, from laminating paper using glue [16] to

Ultrasonic Consolidation (UC) of metal sheets [23].
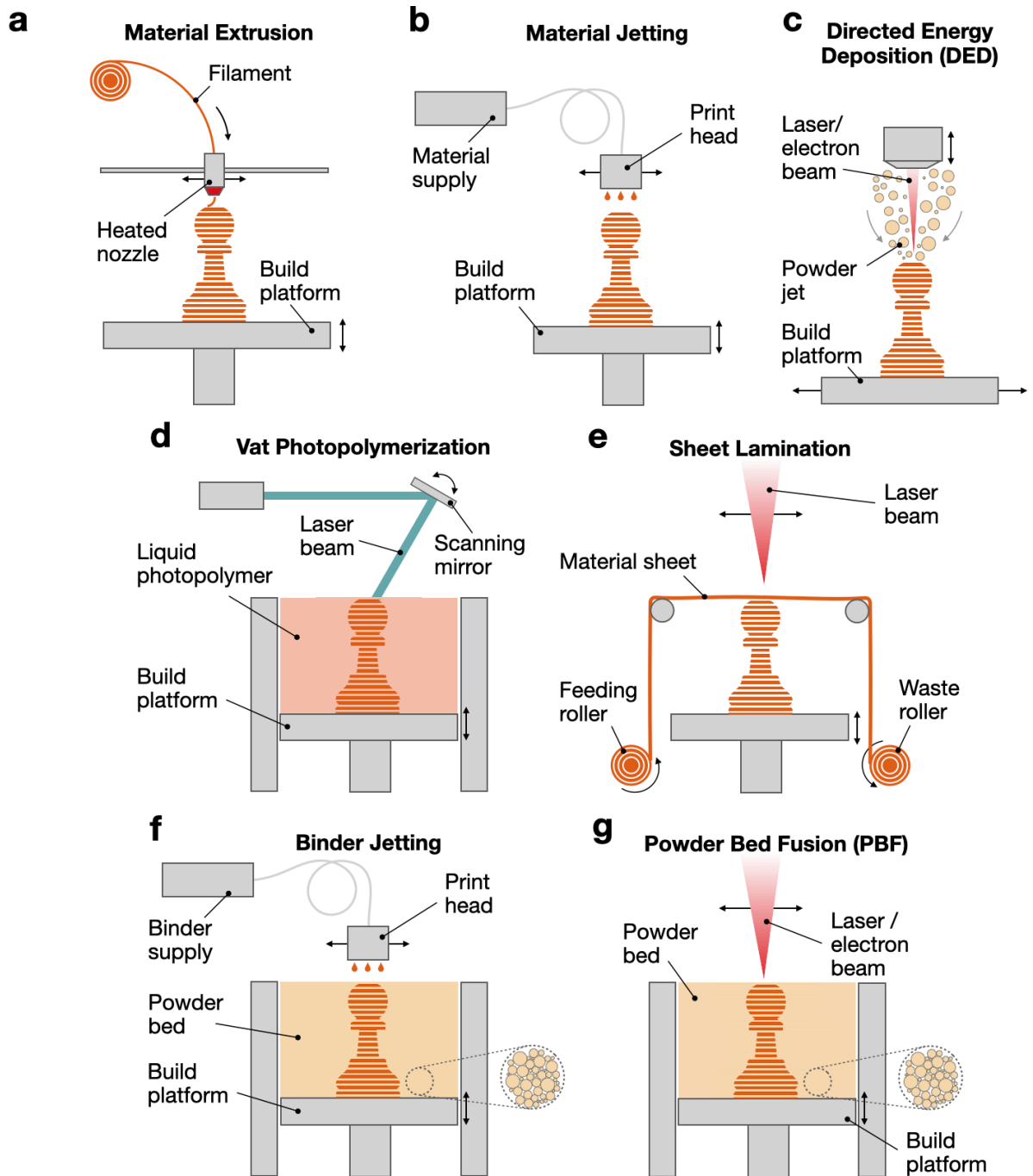


Figure 1.1. Established AM processes

**a** Material Extrusion **b** Material Jetting **c** Directed Energy Deposition (DED) **d** Vat Photopolymerization **e** Sheet Lamination **f** Binder Jetting **g** Powder Bed Fusion (PBF)

In **vat photopolymerization** (Figure 1.1), a liquid photopolymer is selectively cross-linked using a light-activated process, which can be controlled by a laser source in stereolithography (SLA) and two-photon lithography (TPL) and by UV light shaped using Digital Light Processing (DLP) [2,24]. **Material jetting** (Figure 1.1b) refers to selective deposition of droplets of build material, as opposed to a bonding agent in binder jetting [25]. **Directed energy deposition (DED)** (Figure 1.1c) locally fuses materials using focused thermal energy, such as laser-driven consolidation of powder in Laser Engineered Net Shaping (LENS®) [26]. Finally, **powder bed fusion (PBF)** (Figure 1.1g) describes beam-based selective thermal fusion of regions of a powder bed, such as powder melting using a laser source in Selective Laser Melting (SLM) or a focused electron beam in Electron Beam Melting (EBM) [5,20]. A detailed review of these AM processes can be found in [1–3].

Up until a few years ago, only powder bed fusion, binder jetting, sheet lamination, and DED have been capable of producing metal and ceramic parts. Recently, the other three AM categories have been extended to metals and ceramics. Material extrusion of metal wires melted by a plasma arc became a basis of RPD [4] and Electron Beam Freeform Fabrication (EBF3) [27]. 3D printing of silicon oxycarbide was achieved by vat photopolymerization of siloxane-based photoresins followed by pyrolysis [28]. Material jetting has also been adopted for metals by using inkjet and electrohydrodynamic (EHD) fabrication approaches [29,30].

All of these process categories provide access to metal and ceramic 3D printing, but they utilize different physical mechanisms for selective material consolidation in three dimensions. This results in different process capabilities, including process resolution,

minimal feature size, and process throughput. Next, we provide a discussion of these process characteristics and a comparison between established AM processes.

**Minimum feature size and throughput in AM**

Important characteristics of an AM process include minimum feature size and throughput. **Minimum feature size** represents the size of a discrete material deposit and is characterized by typical in-plane (x and y) and out-of-plane (z) dimensions. Representative in-plane dimensions are often measured using the size of an as-fabricated slender feature, such as a cylinder or a beam. Given the layer-by-layer nature of AM, minimum out-of-plane dimensions typically correspond to the minimum layer thickness. This minimum feature that can be reproduced by the process is typically referred to as **voxel** [7]. As discussed below, voxel volume becomes important for estimating process throughput at the relative scale of the process.

**Process throughput** describes the rate of material deposition typical for the process. The fabrication time is mainly a function of the part volume, so volumetric throughput ($mm^3$/hr) becomes an important parameter to evaluate whether a part can be fabricated within a reasonable time. However, comparison between processes with vastly different feature sizes in terms of volumetric throughput has limited utility, as illustrated below.

Figure 1.2 shows a comparison between the established metal AM processes in terms of minimum feature range and volumetric throughput (see Appendix B: Comparison of minimum feature sizes for metal additive manufacturing technologies for data and references). Here, the minimum feature range corresponds to the range of both in-plane and

out-of-plane dimensions. This comparison spans processes with the range of minimum features between few micron and ten millimeters, a more than three orders of magnitude difference. Figure 1.2 demonstrates a correlation between the process resolution and the volumetric throughput. Manipulating larger material deposits leads to higher material deposition rates, which typically results in higher volumetric throughputs for processes with lower resolution. At the extremes of this range, RPD is capable of depositing 3-12 mm features at $>10^6$ mm$^3$/hr, while the throughput of electrochemical fabrication (EFAB) is $<10^2$ mm$^3$/hr with feature dimensions between 4-10 μm. However, this does not mean that RPD can more efficiently print the structure of the same complexity than EFAB.
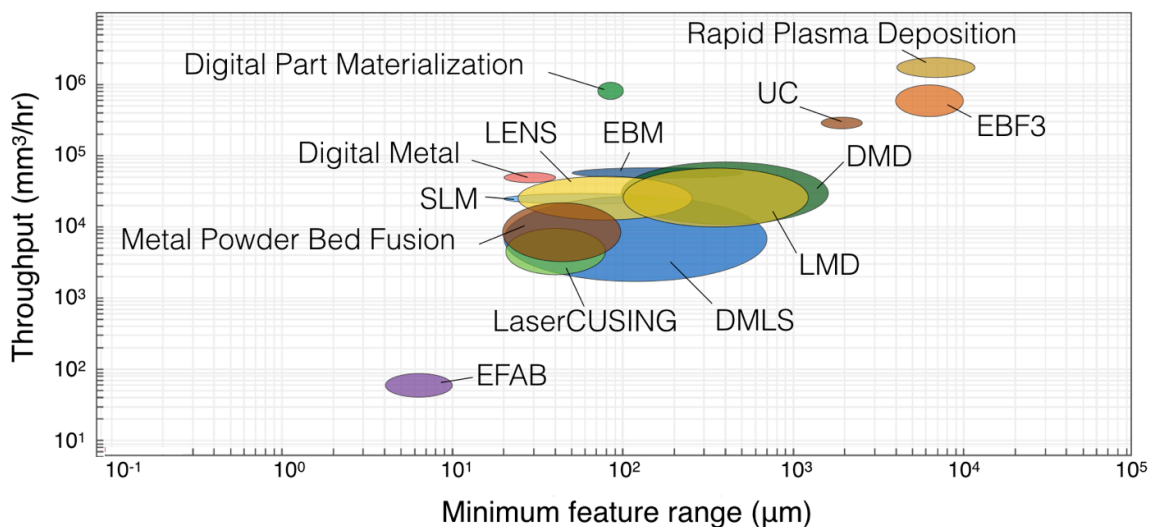


Figure 1.2. Resolution vs throughput for established metal AM processes

Please see Appendix B: Comparison of minimum feature sizes for metal additive manufacturing technologies for data and references

To quantify process throughput in terms of complexity of the part, a metric 'voxels s$^{-1}$' has been proposed to compare the write speeds of metal AM processes with different resolutions [7]. Writing with higher resolution requires a larger number of voxels to define the same

geometry, which translates into longer processing times and lower volumetric throughputs. Comparing the speed between processes with different resolutions can be accomplished by normalizing the write speed ($\mu$m s$^{-1}$) by the feature size ($\mu$m) or by normalizing the volumetric throughput ($\mu$m$^3$ s$^{-1}$) by the voxel volume ($\mu$m$^3$) [7]. This proves to be a more useful metric in terms of rate of underlying mechanism of material consolidation. We return to comparison of established and emerging AM processes using 'voxels s$^{-1}$' in Resolution, feature size, and throughput section of Chapter 2.

**AM Process Framework**

With more than two dozen AM processes commercially available or in development, it is challenging to provide generalizations about the processes beyond the ISO/ASTM categories introduced above. Also, some of the more recent AM processes, such as electrochemical fabrication (EFAB) [31] and laser-induced photoreduction [32,33], cannot be described by either of the categories. Here, we propose a classification framework that describes AM processes according to the underlying principle of creating a 3D geometry. This framework includes the material feedstock, the energy source, and the shape definition approach (Figure 1.3). These key elements of every AM process are discussed further.
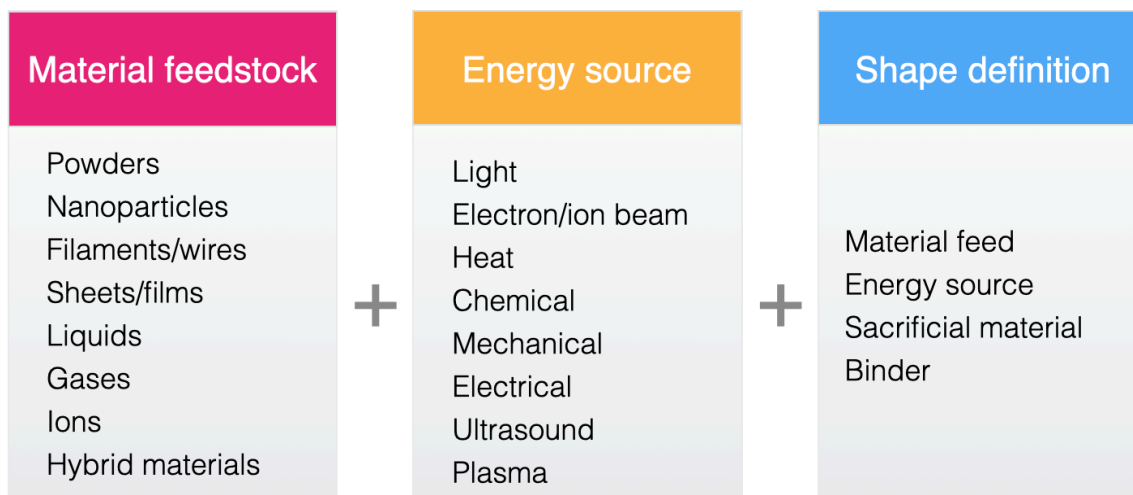
Figure 1.3. AM framework showing key elements of an AM process

*Material feedstock*

AM processes involve layer-by-layer consolidation of smaller portions of a material to build a larger complex 3D part. Material feedstock refers to the type of a material that is being supplied for this gradual consolidation. Metal and ceramic **powders** can be directly sintered or melted together using powder bed processes, such as Selective Laser Sintering (SLS) and EBM, or DED processes, such as LENS® [6,26,34]. **Nanoparticles** are generally not utilized in these types of processes due to challenges in their manipulation in dry form, safety concerns, and potential cold sintering, but are frequently used in deposition in the form of nanoparticle inks, suspensions, or in composites [35–37]. **Filaments** can be melted and extruded through a nozzle in FDM, and **wires** can be supplied to a locally heated melt pool in RPD [4,19]. Selective cross-linking of **liquid** photopolymers is a basis of SLA [2,24], and metal ion solutions are used for electroplating in EFAB [31]. **Hybrid** and sol-gel materials can be blended with photopolymers or directly extruded [38–42]. Finally, **precursor gases** can be selectively decomposed into carbon or metal/carbon composites using a focused ion or electron

beam in FEBID/FIBID [43]. We further discuss energy sources available in AM to join material feedstocks.

*Energy source*

AM processes require an energy source that allows for material consolidation. The choice of energy source typically defines the underlying physical mechanism of joining the material. **Light** can be used for photoinitiated polymerization in SLA and TPL, to induce sintering and melting in SLS and DED, or to directly reduce metal ions from the solution [2,24,26,32,33]. **Focused electron beam** can be utilized for thermal consolidation in EBM or for material decomposition in FEBID [5,43]. **Heat** can be applied for melting a filament in FDM or for direct consolidation of inks in Xjet [6,19,22,25]. **Mechanical** energy is supplied for material welding in additive friction-stir manufacturing (AFSM) setups [44]. **Chemical** energy is utilized in the solidification of a liquid bonding material in binder jetting [20,21]. **Electrical** energy is used in electroplating-based processes for reduction of metal ions from a solution [45,46]. **Ultrasound** is utilized in joining laminated layers of metal using Ultrasonic Consolidation (UC) [23]. Finally, **plasma** is used for localized material welding in RPD [4]. Depending on the energy source, localized energy delivery can serve as an efficient strategy for shape definition. We further discuss shape definition approaches in AM.

*Shape definition*

There are four shape definition approaches that are typically used in AM: material feed, energy source, binder, and sacrificial material. They differ in terms of using either primary or secondary materials to set the part shape. Here, we will define the primary material as the material that will ultimately comprise a 3D printed structure, and the

secondary material as the auxiliary one that serves shape definition purposes, but is ultimately removed from the part. When a primary printing material is used, the shape can be defined by either localized **material feed** or by localized **energy delivery**. For example, a combination of Powders+Light as the material feedstock and the energy source can either be used in powder bed processes, where the shape definition is controlled by light delivery from the laser source, or by localized delivery of the printed material to the melt pool created by the laser source, which is utilized in DED [6,26,34]. When a secondary material is used for shape definition, it could either **bind** the primary material together, e.g. a liquid bonding agent in binder jetting, or serve as a **sacrificial material** that sets the template for the primary one, e.g. an electroplating template in EFAB [20,21,31]. We return to the role of the energy source and the shape definition approach on the process throughput in Increasing Throughput of AM section of Chapter 6.

Figure 1.4 shows how three established metal AM processes, namely RPD, EBM, and EFAB, fit into the AM process framework. RPD relies on melting of mm-sized wires using a plasma arc, and the shape is defined by locally delivering the material to the melt pool using a robotic arm [4]. EBM selectively melts a powder layer using a focused electron beam, and the individual layer geometry is defined by steering the beam across the powder bed [5]. EFAB uses a lithographically defined pattern of sacrificial material that serves as a template for electroplating, and the resulting pattern of electrochemically reduced metal is then refined by electropolishing [31]. All three processes can be described by a distinct combination of the material feedstock, the energy source, and the shape definition approach: RPD is Filaments/wires+Plasma+Material feed, EBM is

Powders+Electron beam+Energy source, and EFAB is Ions+Electrical+Sacrificial

material (Figure 1.4). For every process, the choice of material feedstock has direct

implications for the minimal feature size attainable by the process, as discussed further.
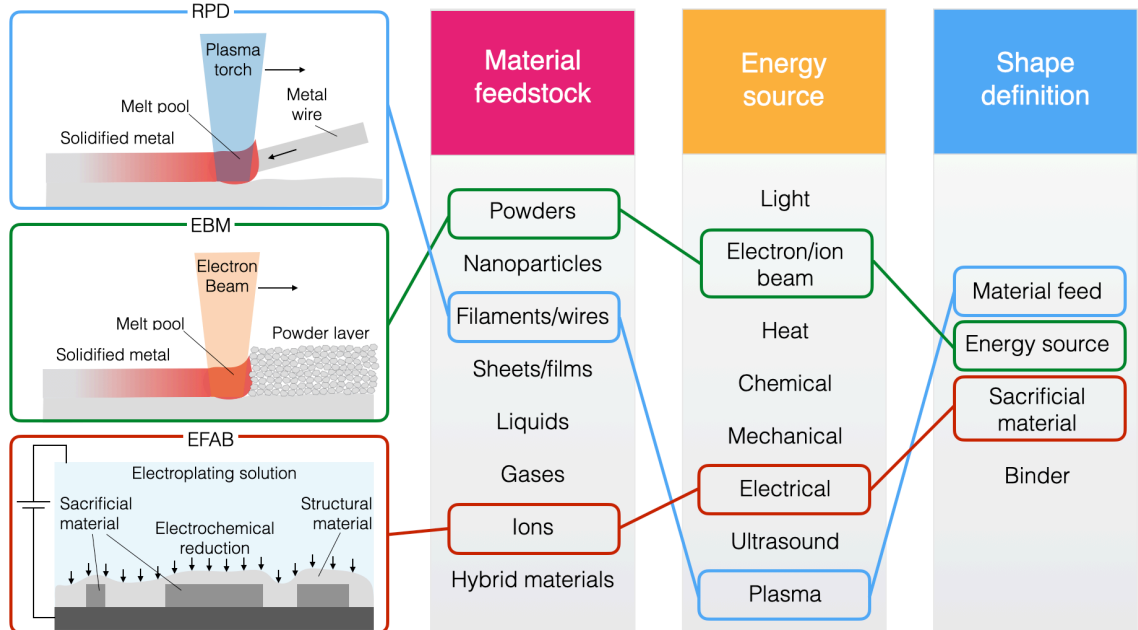


Figure 1.4. Example of using AM framework to analyze three established
metal AM processes: RPD, EBM, and EFAB

**Role of Material Feedstock in Minimal Feature Size of AM**

Minimum feature size is generally limited by the material feedstock, i.e. the method of

supplying metal in powder, wire, sheet or ink form during fabrication. This limitation stems

from the fact that the smallest feature replicated by the AM process cannot be smaller than

the minimal amount of material that can be manipulated by the process. The effect of material

feedstock choice on the minimal feature size is illustrated in Figure 1.5 using the previously

introduced AM framework.
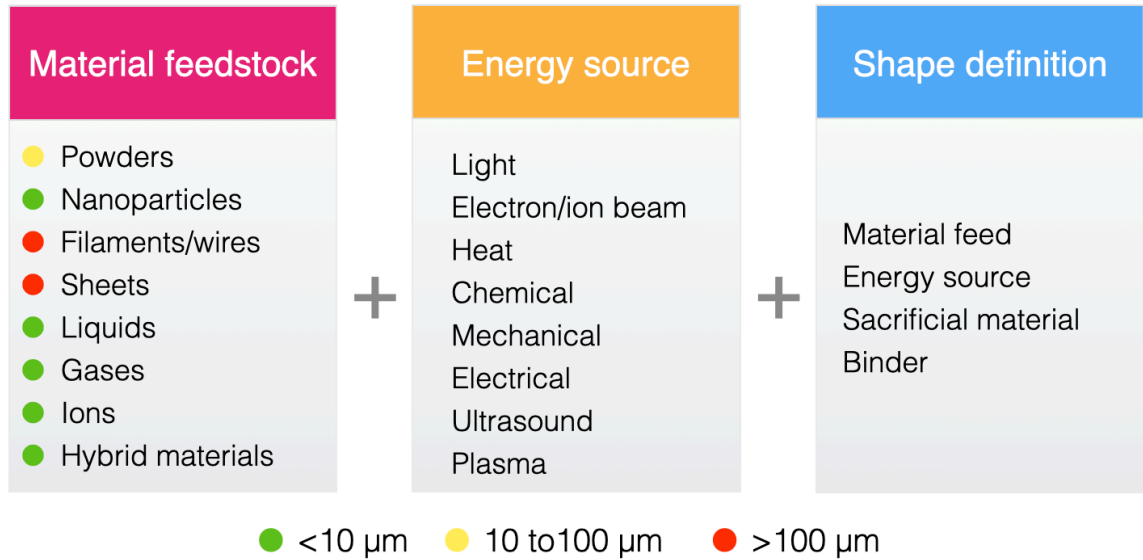
Figure 1.5. AM process framework showing the role of the material feedstock on the minimal feature size

Inkjet-based methods [29,30] manipulate 40-60 μm droplets of metal inks, limiting the smallest features to at least the size of a solidified droplet. Wire- and filament-based processes, such as Plasma Deposition [4] and Electron Beam Freeform Fabrication (EBF3) [27], rely on locally melting a >100 μm-diameter metal wire, which produces millimeter-sized features. Powder-based processes, such as Selective Laser Melting (SLM) and Laser Engineered Net Shaping (LENS) [26], consolidate ~0.3-10 μm metal powder particles, which limits the smallest feature size to about 20 μm [6,34].

Overcoming these resolution limitations requires a capability to manipulate nanoscale quantities of metals in a stable and scalable 3D printing process. The following section gives a brief overview of these nanoscale metal and ceramic AM processes and of the corresponding material feedstocks.

**Nanoscale Metal and Ceramic AM techniques**

We begin this discussion by defining what we mean by 'nanoscale' and 'microscale AM'. Here, we will refer to the processes with <1 μm minimal feature sizes as to 'nanoscale AM' and to processes with <100 μm minimal feature sizes as to 'microscale AM'.

Material feeds to fabricate 3D metal and ceramic structures with <100 μm features include nanoparticle inks, ion solutions, droplets of molten metal, and precursor gases (see Figure 1.5). Direct ink writing (DIW) of metal nanoparticle inks through a micrometer-sized nozzle followed by laser annealing can produce wires with sizes down to 600 nm [37]. Electrohydrodynamic printing (EHD) also allows for manipulation of nanoparticles by controlled ejection of sub-micron droplets of nanoparticle suspensions driven by an electric field [35,47,48]. Meniscus-confined electroplating uses local electrochemical reduction of metals in the area of contact between an electrolyte-filled pipette and a conductive substrate to produce sub-micron features [49]. Metal ion solutions are also used in laser-induced photoreduction where focused laser irradiation can drive local photochemical reduction and deposition of micron-sized metallic features [32,33]. Focused electron and ion beam-induced decomposition (FEBID/FIBID) utilizes decomposition of precursor gases by the focused beam to produce sub-micron deposits that contain metal, carbon, and organics [50,51]. Other AM techniques that can potentially be extended to produce nanoscale features include laser-induced forward transfer (LIFT) that uses laser-driven ejection of droplets of molten metal from a thin film. A detailed review of micro- and nanoscale metal AM processes can be found in [7].
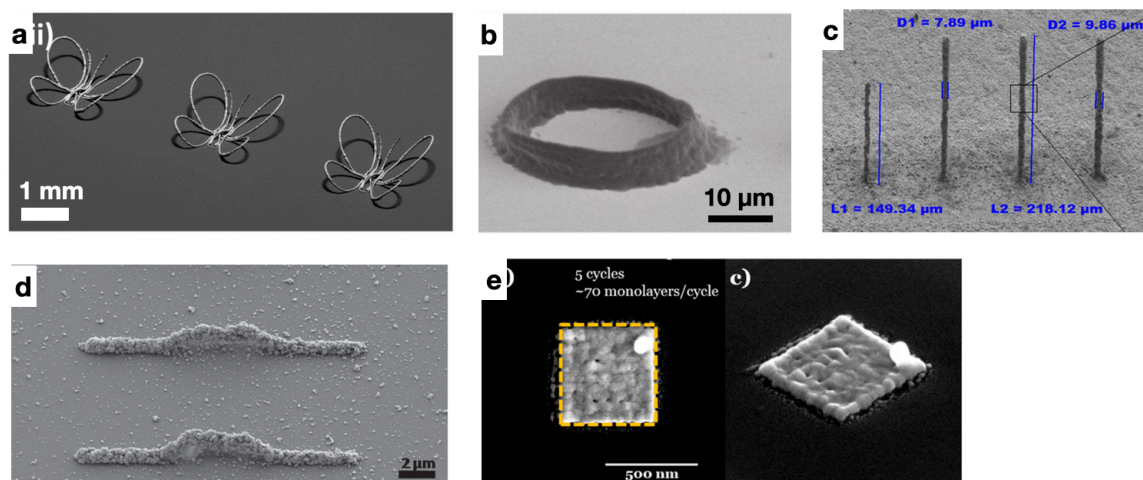
Figure 1.6. Nanoscale metal AM processes using alternative, smaller metal feedstocks

**a** Direct ink writing (DIW) using nanoparticle ink. Adopted from [37] (PNAS, open-access). **b** Electrohydrodynamic (EHD) printing using nanoparticle suspension. Adopted from [47] with permission from John Wiley and Sons. **c** Laser-induced forward transfer (LIFT) using droplets of molten metal. Reproduced from [52] (Springer Nature, open-access). **d** Laser-induced photoreduction using metal salts. Adopted from [53] with permission from John Wiley and Sons. **e** Focused electron beam-induced deposition (FEBID) using precursor gas. Adapted with permission from [54]. Copyright (2015) American Chemical Society

One of the key limitations of the discussed nanoscale and micro-scale AM is low throughput that impedes practical applications of these methods. Processes that use localized electroplating [45,46] or metal ion reduction [32,33] employ a very slow electrochemical process that is limited by the rate of stable electroplating. Electrochemical fabrication (EFAB) allows for manufacturing geometries with 10 μm features and 4 μm layers but is limited to structures with a total height of 25-50 layers due to challenges in stability of electroplating of thick structures [31]. Other technologies, like micro-deposition of metal nanoparticle inks [35–37] or molten metal [55] and focused ion beam direct writing (FIBDW), also suffer from low throughput and are more suited for low-volume fabrication and repair [43]. We return to a detailed comparison between the minimum feature size and

the throughput of nanoscale AM processes in the Resolution, feature size, and throughput section of Chapter 2. We further review state-of-the-art AM techniques to produce materials with particular optical, mechanical, and photocatalytic properties and the significance of these AM processes.

**Significance of micro- and nanoscale AM of metals and ceramics**

At the micro- and nano-scales, AM is poised to become the enabling technology for efficient 3D MEMS, micro-battery electrodes, electrically small antennae, and micro-optical components [6,7,56,57]. Facilitating these technologies requires a fabrication process to manipulate a variety of functional materials in 3D, however the material choice for AM at the nano- and micro-scale is extremely limited. This limitation is especially pronounced when particular material properties, including piezoelectric, magnetic, or optical, are required for the final application [58–60]. The following sections explore the significance of 3D printing three types of materials at micro- and nano-scales: (1) metals, (2) transparent, high-refractive index materials, and (3) photocatalysts.

*Metals*

Nanoscale additive manufacturing of metals provides opportunities for streamlined production of complex sub-millimeter devices, including 3D MEMS [6], 3D microbattery electrodes [56], and microrobots and tools for minimally invasive medical procedures [57]. Specifically, nanoscale metal AM enables technologies that require 3D conductive materials, manipulating electrons, and magnetic nanostructures. Micro- and nano-sized metallic architectures comprise interconnects for transparent conductive electrodes (TCE), including

3D interconnects for flexible TCEs [47,48,61]. Optical metamaterials, including chiral structures and highly absorptive materials, are enabled by metallic 3D architectures [62,63]. 3D architected magnetic materials could enable 3D nanomagnet logic devices [64]. Sub-micron conductive materials in 3D are required for fabrication of nanoscale electron sources [51] and scanning probe single electron transistors [65]. Nanoscale metal AM could enable further device integration on non-planar substrates, e.g. functional devices and sensors in microfluidics, including channel-embedded micro-heaters [66] and 3D nano-architectures for volumetric surface-enhanced scattering [67]. Finally, compact on-chip integration in 3D stacks could be enabled by reliable and high-throughput fabrication of 3D metallic interconnects [49]. Chapter 2 explores the development of nanoscale AM process for nickel and extending the process to other metals.

*High-refractive Index Materials*

A conspicuous example is a lack of AM processes for high refractive index ($n$), low absorption materials with nano-sized dimensions [68], which are typically required for micro-optics and device applications. Polymer materials that can be shaped using direct laser writing (DLW) methods, such as two-photon lithography (TPL), are limited to refractive indices below 1.8 [69]. Hybrid materials for TPL that consist of inorganic silica-type networks with embedded heteroatoms, including Zr, Zn, and Ge, have been demonstrated, but their refractive indices were below 1.6 [39–42]. Direct Laser Writing (DLW) of $As_2S_3$ chalcogenide glasses with $n$ between 2.45 and 2.53 in the infrared has been demonstrated by taking advantage of their photo-induced metastability [59], but the high index mismatch between the lens and the printed material complicated the feature size control. Metal oxides with refractive indices $n$~1.9 have been nano-architected using

DLW of aqueous metal-containing photopolymers followed by calcination, but the low metal ion loading in these resins led to linear shrinkage of up to 87%, which made it challenging to preserve complex 3D geometry [58,70]. TPL of organic-inorganic resists combined with post-lithography thermal treatment has shown promise to create 3D nanolattices of metals and ceramics, but the residual porosity of up to 20% within the beams reduces the effective refractive index [71,72]. An AM process that can repeatably and accurately produce 3D architectures with sub-micron geometrical features out of high refractive index, low absorption material is yet to be developed and would realize multiple micro-optical devices and three-dimensional (3D) dielectric photonic crystals (PhCs) [60].

3D dielectric PhCs have been a focus of extensive research for their unique ability to tailor and manipulate light [73,74]. 3D PhCs with a full photonic bandgap [75,76], 3D chiral PhCs that control light polarization [63], and all-angle negative refractive (AANR) index materials [77] have been demonstrated. Each of these devices is enabled by satisfying stringent optical material requirements and dimensional control. For example, obtaining a full photonic bandgap in woodpile architectures requires constituent materials with a refractive index $n \gtrsim 1.9$ [78], and attaining AANR requires an effective index of $n \geq 2.49$ [79], with individual features smaller than the target wavelength. Creating nano-sized three-dimensional architectures out of high refractive index materials, such as silicon (Si), gallium arsenide (GaAs), and titanium dioxide ($TiO_2$), can only be achieved via sophisticated experimental procedures. Examples include micromanipulation of individually stacked layers [80] or single- or double-inversion of a polymer templates that often result in features with up to 16% porosity [60,76].

Titanium dioxide (titania, $TiO_2$) represents a beneficial material choice for 3D dielectric

PhCs in the visible and the infrared because of its high refractive index and high transparency

[60]. The highest refractive index, between 2.45 and 3.03 for 500-1500 nm wavelengths, is

attained in the rutile phase of $TiO_2$ [81]. The processes for AM of titania demonstrated to

date suffer from high porosity, low refractive index of the constituent material, and poor

repeatability. An ideal AM process for titania would have to repeatably and accurately

produce 3D structures with sub-micron features out of fully dense rutile $TiO_2$. Several

previous studies have described AM processes for $TiO_2$ (Figure 1.7).
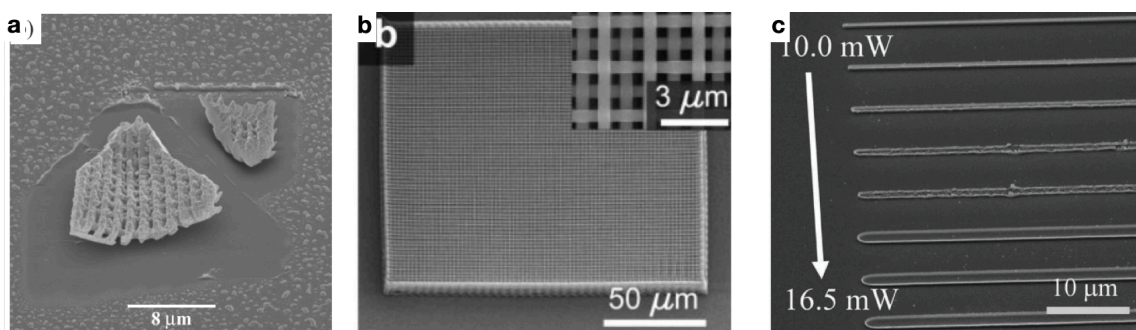


Figure 1.7. Prior art 2D and 3D fabrication processes for titanium dioxide

**a** Femtosecond laser-induced precipitation. Adopted from [71] with permission. Copyright ©
2007 WILEY-VCH Verlag GmbH & Co. KGaA, Weinheim **b** Direct Ink Writing (DIW) of sol-
gel based inks. Adopted with permission from [38]. Copyright © 2007 WILEY-VCH Verlag
GmbH & Co. KGaA, Weinheim **c** Laser-induced decomposition of liquid precursors. Adopted
with permission from [82]. © 2018 WILEY-VCH Verlag GmbH & Co. KGaA, Weinheim

Direct Ink Writing (DIW) of sol-gel inks followed by calcination (Figure 1.7b) has been

shown to produce $TiO_2$ features with sub-micron dimensions that are ~10% porous and

contained about a half of a lower-index anatase phase, which lowered their effective

refractive index by at least 10% [38]. Femtosecond laser processing of liquid $TiO_2$ precursors

(Figure 1.7a) has been used to selectively introduce insoluble regions into the patterned

material by breaking chemical bonds, but the poor adhesion between the sample and the substrate led to the loss of heat-treated 3D structures [71]. Laser-induced decomposition of sol-gel precursors (Figure 1.7c) enabled 2D patterning of $TiO_2$/carbon composites with typical feature widths of 3 μm for crystalline $TiO_2$ and has not been extended to three dimensions [82]. Chapter 4 explores the development of nanoscale AM process for high-refractive index materials.

*Photocatalytic materials*

Access to safe drinking water remains a global challenge as some 663 million people do not have improved water sources available to them [83]. Even in areas where municipally-treated water is available, tenants often cannot afford it, which leads to illegal tapping and recontamination from the sewage water (see Figure 1.8a) [84]. According to The Gates Foundation, poor sanitation contributes to nearly 700,000 child deaths from diarrhea worldwide every year [85]. Low-cost, sustainable, rapid and easy-to-use methods for household water treatment are urgently needed.

To get a clean water supply at home, more than five million people in over 50 countries in the world are currently relying on solar disinfection of drinking water (SODIS) [84]. SODIS is a method of water treatment where a transparent water container (e.g., a plastic bottle) is exposed to direct sunlight (see Figure 1.8b). This leads to inactivation of microorganisms, mainly via ultraviolet (UV)-induced DNA damage and interaction with reactive oxygen species (ROS) [86]. SODIS is a cheap and straightforward approach for water treatment, but it is also time-consuming and often requires up to 48 hours to disinfect water [84].

Figure 1.8. Need for efficient and low-cost household water disinfection technologies

**a** Water collection point potentially contaminated by surface waste water **b** Solar Water Disinfection (SODIS) using water treatment using transparent containers exposed to sunlight. Images adapted with permission from [84]. Copyright © 2012 Elsevier B.V.

The water disinfection rate can be drastically increased by utilizing heterogeneous photocatalysis that allows to harvest solar energy or UV light and unselectively mineralize organic molecules and deactivate bacteria [87–90]. When a semiconducting catalyst is hit by a photon with energy equal or higher than its bandgap, the produced electron-hole pair allows the catalyst to react with water and dissolved oxygen to generate reactive oxygen species (ROS), such as hydroxyl radicals ($^•OH$) and superoxide radicals ($^•O_2^-$) [87].

The ROS then react with organic molecules, producing $H_2O$, $CO_2$, and inorganic ions as final products [91]. High water disinfection rate using this strategy has been demonstrated with $TiO_2$ [88], ZnO [89], and $MoS_2$ [90]. In laboratory and pilot plant settings, the use of these photocatalysts in the form of particle suspensions and multi-functional membranes leads to high water disinfection rates (Figure 1.10) [92]. However, as discussed further, several unique aspects make these forms of photocatalysts inadequate for household use of SODIS.
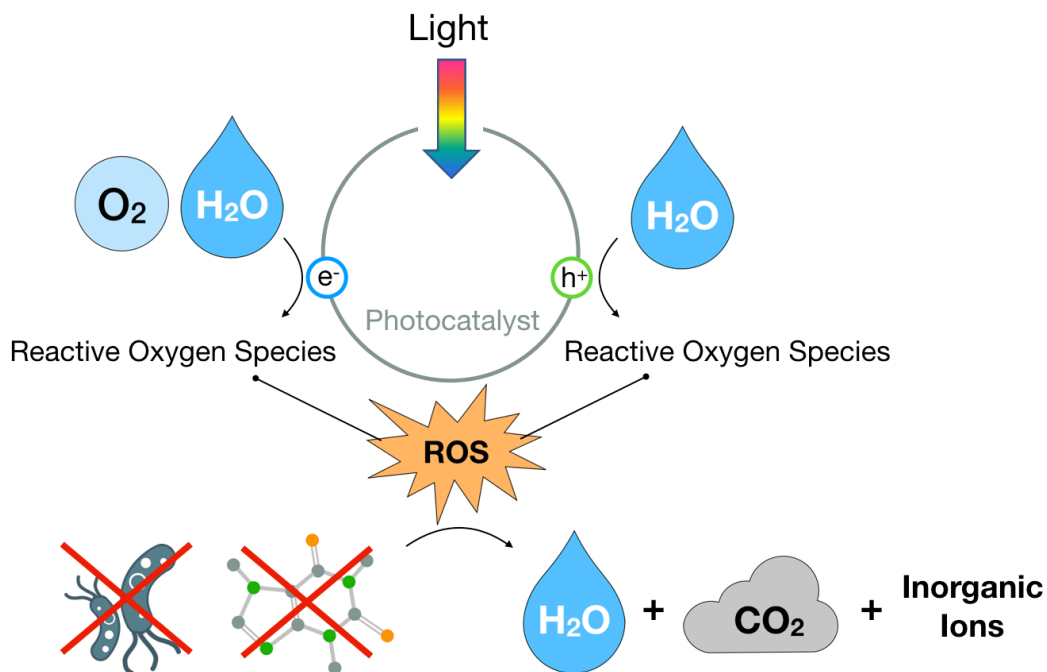
Figure 1.9. Photocatalytic generation of reactive oxygen species (ROS) for water treatment
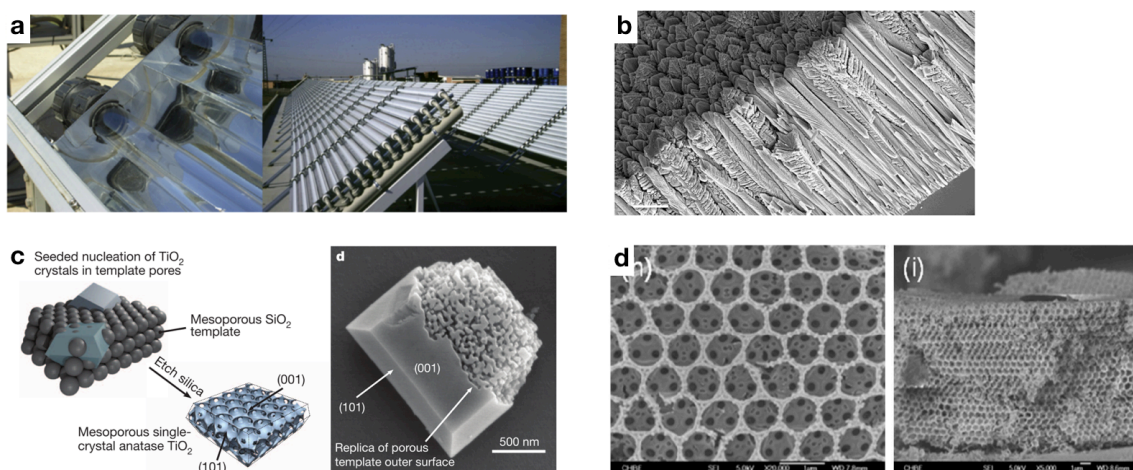


Figure 1.10. Titanium dioxide for photocatalytic water treatment in laboratory and pilot plant settings

**a** Titania nano-powders in pilot-plant flow reactors. Reproduced with permission from [93]. Copyright © 2015 Elsevier B.V. **b** Titanium dioxide coatings. Reproduced from [94] (open-access, Copyright © 2019, Springer Nature). **c** Mesoporous single crystals of $TiO_2$. Reproduced with permission from [95]. Copyright © 2013, Springer Nature **d** Inverse opal $TiO_2$ structures acting as photonic crystals for efficient light harvesting. Reproduced with permission from [96]. Copyright (2015) American Chemical Society

## 1. No ultrafiltration available to recover catalyst particles

Recovering nano-sized catalyst particles from treated water requires a complex filtering procedure, which makes the overall process expensive and impractical, especially in a household [84]. The risks of environmental release can be mitigated by using one of the most well-studied non-toxic photocatalysts, titania ($TiO_2$) [88,97–99]. However, it is necessary to filter out all of these titania particles from the drinking water due to the unknown health effects and unbearable taste [84]. Durable immobilization of catalyst material is of utmost importance to avoid catalyst leakage into the drinking water [87].

Creating highly porous $TiO_2$ structures that are stable under water flow is technically challenging [100]. Various solid substrates have been utilized as rigid supports for titania, including carbon particles [101], silica particles [102], glass fibers and structures [103], and sand [104]. Using a secondary material reduces the available catalytic surface area and limits the mass transfer of the reactants, which renders the process significantly less efficient [105]. In addition, coating a template material or a membrane utilizes thermal treatment of a sol-del-derived amorphous titania layer, which is easily cracked during the process [106], increasing the risk of contamination of the treated water.

## 2. No mixing/stirring available to improve transport of the reactants

The characteristics of an efficient photocatalyst include (i) high surface area that allows for a higher density of active sites and higher reaction rates, and (ii) high porosity that facilitates diffusion of reactants and products [107]. Pilot reactors for SODIS are often slurry reactors, where transport of reactants and products is facilitated by continuously mixing catalyst powder suspensions (Figure 1.10a) [92]. In contrast, using a household

SODIS reactor generally implies that there is no agitation available during most of the treatment. Leaving a catalyst suspension idle in water leads to sedimentation of catalyst particles or any other catalyst-coated template material due to the density mismatch with water [108]. This limits mass transport of the reactants, which significantly reduces the process efficiency [105,108]. Preserving high mass transport and avoiding sedimentation in the absence of mixing/stirring can be allowed by a self-supported catalyst that is structured hierarchically: with nanopores that allow for high surface area and mesopores that facilitate transport (Figure 1.10c, d) [95,109–111]. However, most of hierarchically structured photocatalysts produced so far are prone to natural light screening- an effect that significantly decreases the efficiency of water treatment [111].

3. Requires light access to the whole volume of the catalyst

An efficient photocatalytic reaction requires not only high surface area and good transport of reactants and products, but also light access to the reaction site [112]. Natural light screening occurs in self-supported porous catalysts with stochastic architectures, which leads to impeded light access to the bulk of the photocatalytic structure and, as the result, to lower reaction rates [111]. Deterministic architectures, such as titania inverse opals (Figure 1.10d), allow to efficiently trap the light, but inverse opals are extremely fragile [113], which can result in breakdown of the structure and material release into the water.

Figure 1.11 summarizes the discussed differences between photocatalysts feedstocks and how they relate to surface area, light access, and safety. Household use of a photocatalytic SODIS reactor requires a **high surface-area, strong, self-supported** photocatalyst with

**deterministic architecture** that allows for **light delivery inside the bulk** of the photocatalyst (Figure 1.11). Introducing scalable manufacturing methods that allow to 3D-structure and immobilize photocatalysts can pave the way to creating efficient household reactors for solar water disinfection. Chapter 5 discusses the development of micro-scale AM process to create and study architected titanium dioxide for photocatalytic water treatment.
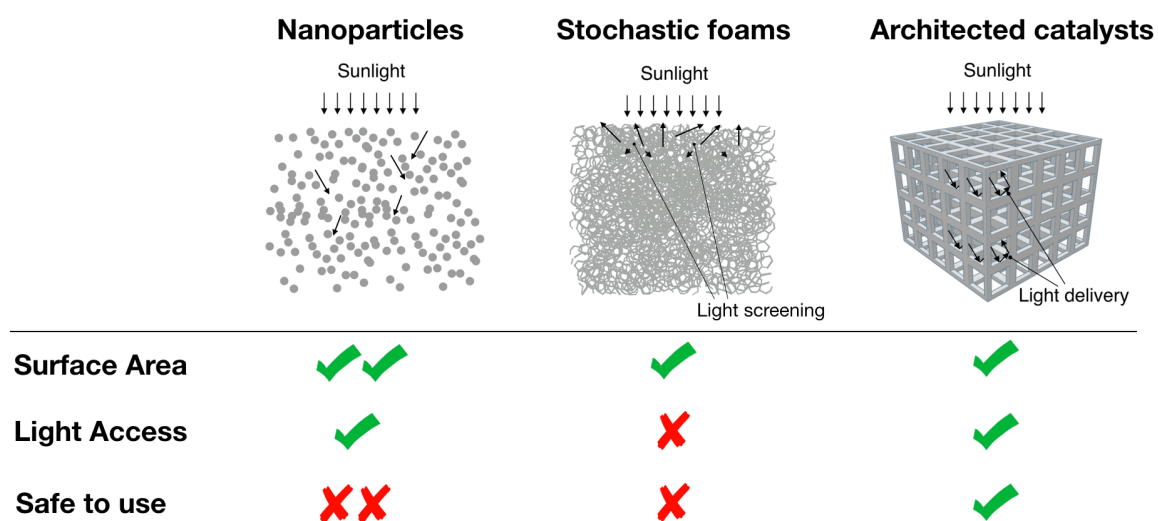


Figure 1.11. Comparison between photocatalyst feedstocks, namely nanoparticles, stochastic and deterministic foams, in terms of surface area, light access and safety

**Thesis outline**

This work is focused on developing micro- and nanoscale AM processes for three types of materials: (1) metals, (2) transparent, high refractive index materials, and (3) photocatalysts (see Significance of micro- and nanoscale AM of metals and ceramics). In Chapter 1 we have introduced AM Process Framework, showed how it can be applied for analysis of established and emerging AM processes, and discussed the importance of material feedstock for nanoscale AM of metals and ceramics. Chapter 2 introduces a nanoscale AM process for

nickel based on hybrid organic-inorganic materials, two-photon lithography, and pyrolysis, and discusses how resolution and throughput of the developed process compares with state-of-the-art nanoscale AM techniques. Chapter 3 provides microstructural characterization of as-fabricated material, mechanical characterization of beam-based lattice architectures created using this AM process, and compares their structural strength to that of parts fabricated using other established and emerging AM techniques. Chapter 4 extends the developed nanoscale AM process to 3D print titanium dioxide, a transparent, high refractive index material in the infrared and the visible. This chapter provides a model to predict and control feature dimensions in this AM process, which enables demonstration of the process for 3D dielectric photonic crystals with a full photonic bandgap in the infrared. Chapter 5 explores microscale 3D printing of photocatalytic materials to investigate the effect of 3D architecture on photocatalytic performance. We finally discuss how this work fits into the AM process framework and how it can be used to help increase AM throughput, introduce new materials for AM, and develop new AM processes.

# CHAPTER 2 : NANOSCALE AM OF NICKEL

**Chapter Summary**

In this chapter, we demonstrate a facile and reproducible process to create complex 3D

metal geometries with 25-100 nm feature dimensions. We synthesize hybrid organic-

inorganic materials that contain Ni clusters and use them to produce a metal-rich

photoresist. We then use two-photon lithography to sculpt computer-designed

architectures out of the resist and pyrolyze them in inert atmosphere at 1000°C and

reducing atmosphere at 600°C to volatilize the organic constituents. Using this approach,

we demonstrate the fabrication of periodic Ni octet nano-lattices with the unit cell size of

2 μm and beams with 300-400 nm diameter as a proof-of-concept. We compare

resolution, feature size, and throughput of the developed AM process to those of

established and emerging metal AM techniques and show how this process can be

extended to fabricate other materials.

**Process for nanoscale metal AM**

We first synthesized nickel acrylate using a ligand exchange reaction between nickel

alkoxide and acrylic acid (Figure 2.1a) and combined it with another acrylic monomer,

pentaerythritol triacrylate, and a photoinitiator (PI), 7-diethylamino-3-thenoylcoumarin,

(Figure 2.1b). Acrylic acid (100 mg) was slowly added to nickel 2-methoxyethoxide

solution (1290 mg) in a glove box and manually agitated. We observed the nearly

immediate change of the solution color from brown to green, which is indicative of a

ligand exchange reaction[114].  The mixture was held at low pressure in the antechamber

of the glove box for 45 min to remove ~60% of 2-methoxyethanol. The resulting

precursor was then taken out of the glove box, mixed with 300 mg of pentaerythritol

triacrylate, and agitated using a vortex mixer for 1 min. 7-diethylamino-3-

thenoylcoumarin (23 mg) was dissolved in 100 mg of dichloromethane, added to the

mixture, which was then agitated using a vortex mixer for 1 min.
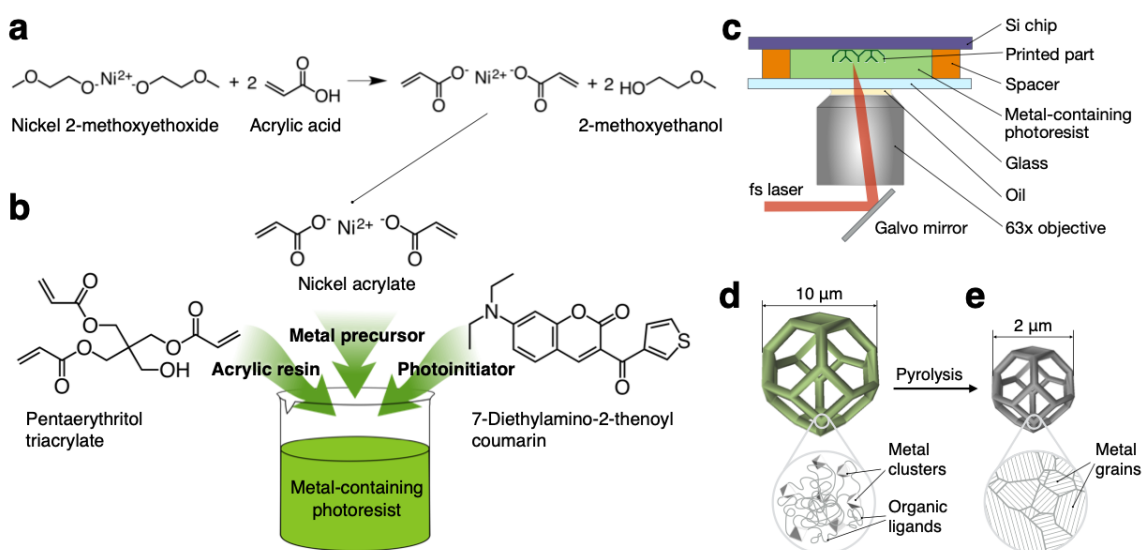


Figure 2.1. Process for nanoscale additive manufacturing of metals.

**a** Ligand exchange reaction used to synthesize metal precursor with cross-linking functionality. **b** Metal precursor, acrylic resin, and photoinitiator are mixed to form a transparent metal-containing photoresist. **c** Schematic of two-photon lithography (TPL) process used to sculpt the scaffold. **d** Schematic of fabrication of metal-containing polymer part that is (**e**) pyrolized to remove organic content and to convert the polymer into a metal.

We then drop cast this photoresist on silicon substrate and used two-photon lithography

(TPL) to sculpt the prescribed 3D architectures (Figure 2.1c). Hybrid organic-inorganic

structures were fabricated on a silicon chip (1 x 1 cm) using a commercially available

two-photon lithography system (Photonic Professional GT, Nanoscribe GmbH). Metal-

containing photoresist was drop cast on a glass slide (0.17 mm thick, 30 mm in diameter)

and confined between the glass slide and a silicon chip using 100 um thick, 2x10 mm ribbons of Kapton tape as spacers. Laser power and scan speeds were set at at 17.5-22.5 mW and 4-6 mm s$^{-1}$, respectively. After the printing process, the samples were developed in 2-methoxyethanol for 1 hour, followed by immersion in PGMEA for 10 min and filtered IPA for 5 min. The samples were then processed in a critical point dryer (Autosamdri-931).

After the non-polymerized resist was washed away and the sample was dried using CPD, the free-standing cross-linked polymer nano-architectures were pyrolyzed to volatilize the organic content. Pyrolysis was conducted in two steps in a quartz tube furnace using 4" quartz tube. As the first step, a heating profile of 2°C/min to 1000°C, hold at 1000°C for 1 hour was applied under 1 L/min argon flow, and the part was let to cool down in the furnace to room temperature. During the second step the part was heated at 2°C/min to 600°C under 1 L/min forming gas flow (5% H$_2$, 95% N$_2$), held at 600°C for 1 hour, and let to cool down to room temperature. This process yielded a replica of the original 3D structure with ~80% smaller linear dimensions made entirely out of metal (Figure 2.1d).

**Morphology**

We demonstrate the feasibility and efficiency of this methodology by first fabricating nanolattices with 10 μm octet unit cells comprised of 2 μm-diameter circular beams out of the synthesized photoresist using layer-by-layer TPL with 150 nm layer thickness. SEM images in Figure 2.2 (a-c) reveal that these nanolattices had fully dense beams and uniformly sized, high-fidelity features.
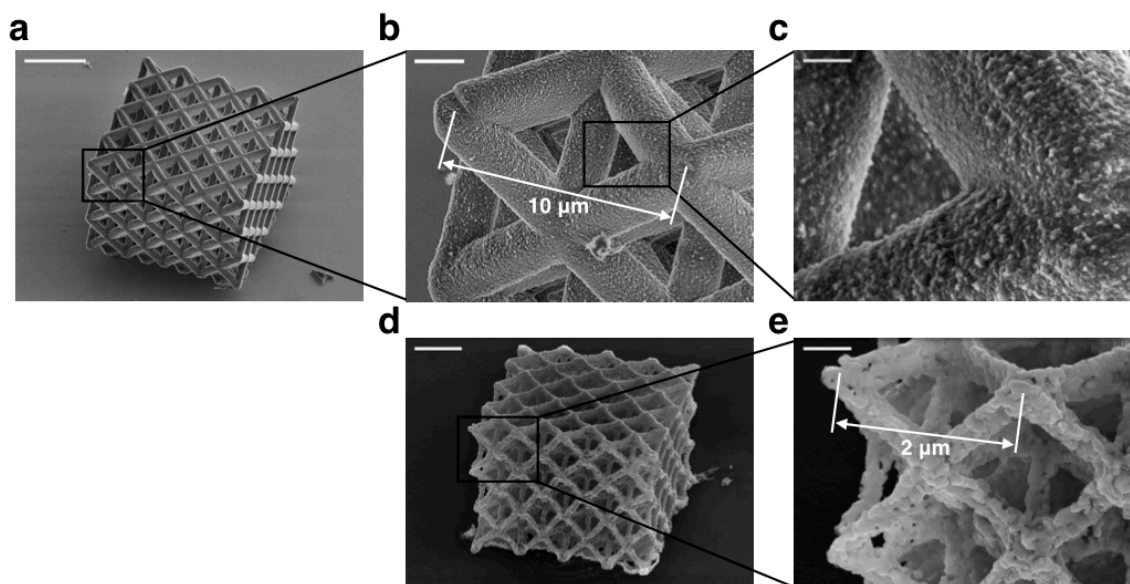
Figure 2.2. SEM characterization of the samples fabricated using nanoscale metal AM.

SEM images of **a-c** a representative octet lattice made out of a nickel-containing polymer at different magnifications and **d, e** a representative nickel nanolattice after pyrolysis. Magnifications in **b** and **d** (scale bars 2 μm) and also **c** and **e** (scale bars 500 nm) are identical. Scale bar is 15 μm for **a**

These nanolattices had four unit cells on each side, 40 μm, and a height of three unit cells, 30 μm, and were supported by vertical springs at each corner and by a vertical pillar the center. These supports served as pedestals that would allow the sample to release from substrate after undergoing an isotropic ~80% shrinkage during pyrolysis (see Figure 2.3).

Pyrolysis was performed in a tube furnace following a two-step procedure: (1) at 1000°C in argon to remove most of the organic content from the samples and to consolidate the Ni metal clusters into denser features, which is accompanied by ~5x linear shrinkage in feature size and (2) at 600°C in forming gas, to reduce the oxygen content in the mostly-Ni samples and to facilitate grain growth.
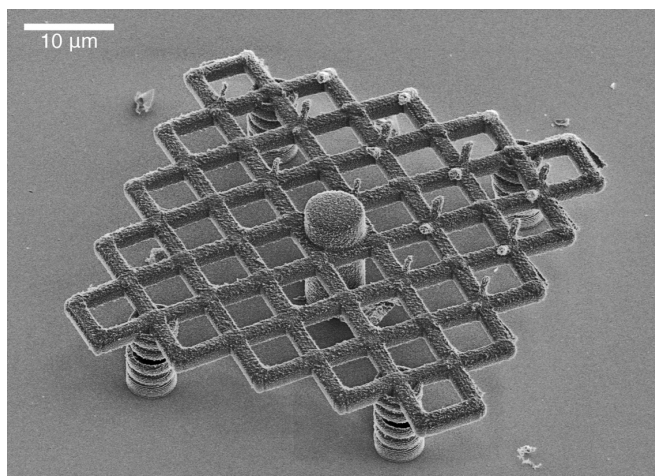
Figure 2.3. SEM image of a representative supporting structure used to decouple the part from the substrate during pyrolysis.

SEM images in Figure 2.2 (d, e) show a representative 3D Ni architecture and convey that the 10 μm unit cells and 2 μm-diameter beams in the original polymer-metal structure shrank to ~2 μm unit cells and ~ 300-400 nm diameter beams in the nickel nanolattice. This also implies that 150 nm layer thickness in the polymer structure corresponds to 30 nm layer thickness in the metal structure. The zoomed-in image in Figure 2.2e shows that the metal beams are ~10%-30% porous caused by pyrolysis.

**Resolution, feature size, and throughput**

Figure 2.4 shows minimal reported printed feature sizes enabled by the method demonstrated in this work and many other metal AM processes available today (see Appendix B). The plotted ranges include both layer thickness and minimum lateral feature size. The minimum z-feature is determined by the resolution of a single layer of material. The minimum lateral feature is defined by multiple factors, which include the energy beam spot size and control over the melt pool. The data in Figure 2.4 demonstrates that the AM process developed in this work is capable of producing

features that are an order of magnitude smaller compared to those produced by other 3D-capable AM processes.
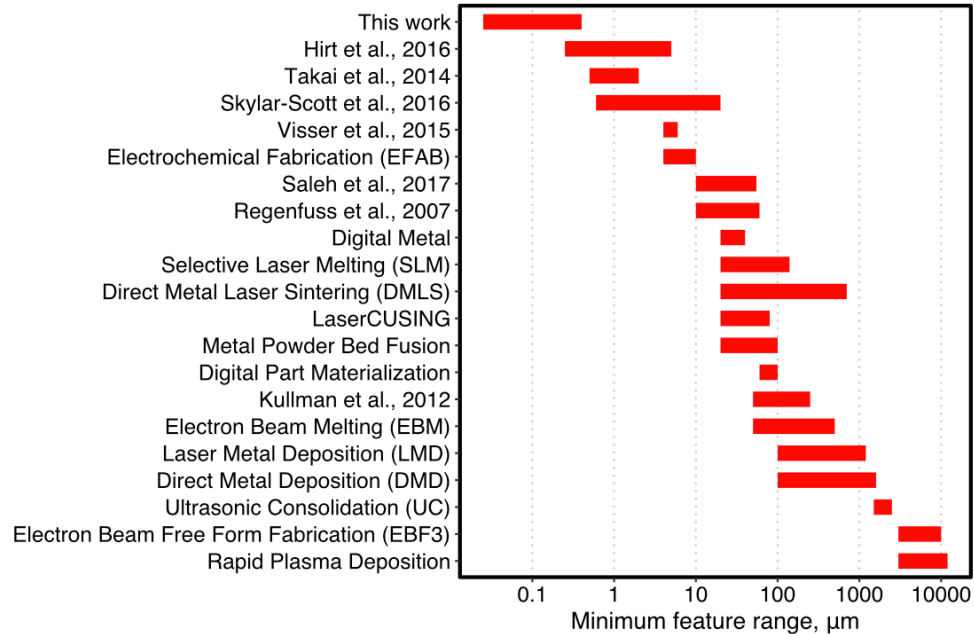


Figure 2.4. Comparison of minimum feature sizes for commercial and potentially scalable metal additive manufacturing technologies.

Using metal-containing photoresist allows to fabricate complex 3D geometries with the resolution that is an order of magnitude finer than that of the state-of-the-art metal AM methods. See Appendix B: Comparison of minimum feature sizes for metal additive manufacturing technologies for data and references

Another key aspect of any metal AM process is the throughput. Using hybrid organic-inorganic photoresist developed in this work allows for writing speeds of 4-6 mm s$^{-1}$, which is ~100 times faster than that for TPL of metal salts [33]. Comparing the speed between metal AM processes with different resolutions can be accomplished by normalizing the write speed (µm s$^{-1}$) by the feature size (µm) or by normalizing the volumetric throughput (µm$^3$ s$^{-1}$) by the voxel volume (µm$^3$) [7]. Figure 2.5 shows a comparison between the throughput (voxel s$^{-1}$) of established and emerging metal AM processes at the corresponding scale of the process, defined here as the minimum feature size (µm) that can be replicated by the process.

For a typical 300-600 nm feature size printed by TPL [115], writing speeds in this work correspond to defining 6700 – 20000 voxels s$^{-1}$, a printing speed that is out of reach for state-of-the-art micro-scale metal AM techniques, i.e. electrohydrodynamic printing (0.05-300 voxels s$^{-1}$), local electroplating (0.04-1.0 voxels s$^{-1}$), focused beam methods (0.01-0.8 voxels s$^{-1}$), and direct ink writing (0.7-3000 voxels s$^{-1}$) [7] (see Appendix C: Comparison of linear and volumetric throughputs of representative micro- and nano-scale metal additive manufacturing technologies).
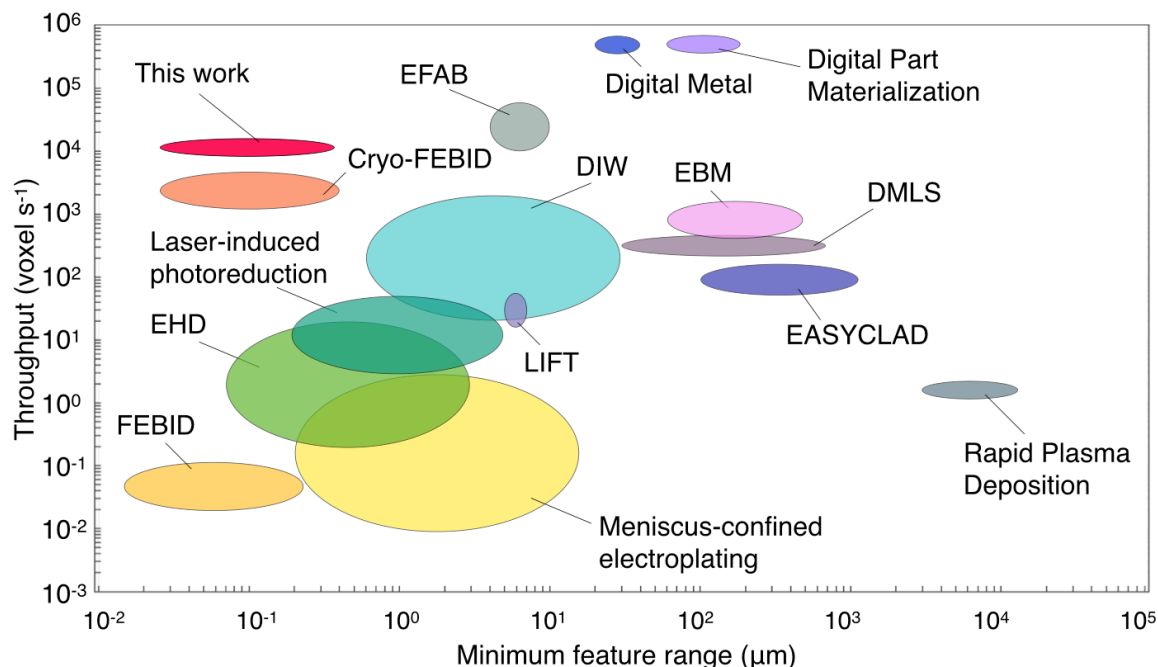


Figure 2.5. Throughput vs minimal feature range for established AM processes and emerging micro- and nanoscale metal AM.

**Extending the developed AM process to other materials**

The developed AM process can also be extended to printing other metals, ceramics, and composites using a similar synthesis route. Figure 2.6 shows examples of incorporating magnesium (Figure 2.6a, b), germanium (Figure 2.6c, d), and silicon (Figure 2.6e, f) into the

hybrid photopolymer and, ultimately, into the post-pyrolysis structure. This approach also allows to combine several hybrid organic-inorganic materials in the photopolymer to create the desired elemental mix within a 3D printed structure (see Ni and Ti-containing structure in Figure 2.6g-i).
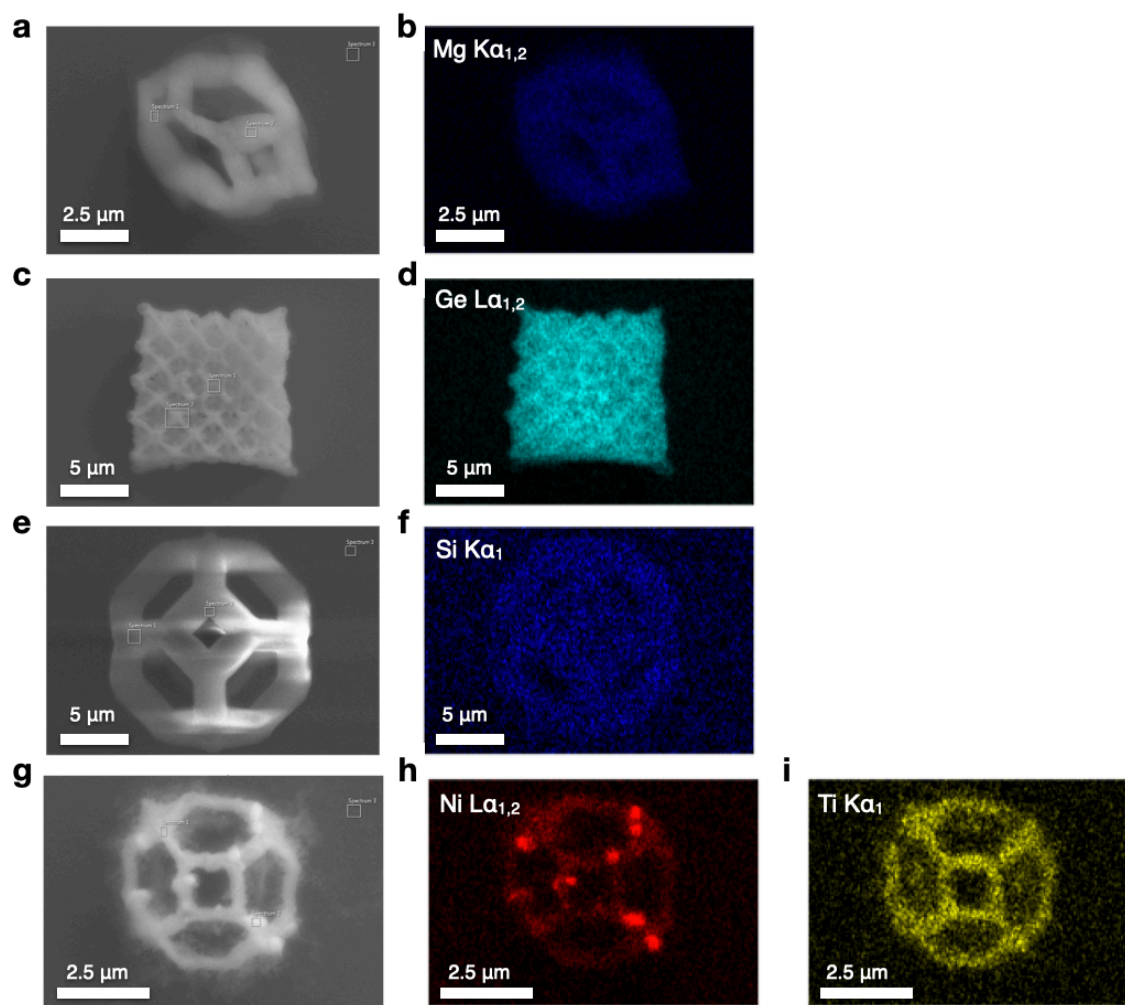


Figure 2.6. Extending the developed nanoscale AM process to incorporate other materials

**a, b** SEM image and EDS map of a magnesium-containing architecture on a Si substrate. **c, d** SEM image and EDS map of a germanium-containing architecture on a Si substrate. **e, f** SEM image and EDS map of a silicon-containing architecture on a GaAs substrate. **g-i** SEM image and EDS maps of nickel- and titanium containing architecture on Si

High scanning speeds and intrinsic advantage of parallelizing light delivery using lithographic methods suggest that the presented AM process lends itself to streamlined and efficient manufacturing of metal nano-architectures. We further examine the microstructure and the mechanical properties of as-fabricated 3D nano-architected nickel.

# CHAPTER 3 : CHARACTERIZATION AND PROPERTIES OF AM NICKEL

**Chapter Summary**

In this chapter, we characterize microstructure, chemical composition, and mechanical properties of nickel fabricated using the developed nanoscale AM process. TEM analysis showed that the microstructure of Ni beams is nanocrystalline and nanoporous, with a 20 nm mean grain size and 10-30% porosity within each beam. Nanomechanical experiments revealed their specific strength to be 2.1-7.2 MPa $g^{-1}$ $cm^3$, which is comparable to that of the metal lattices with 0.1-1.0 mm beam diameters fabricated using alternative metal AM technologies. These findings suggest an efficient pathway to create complex three-dimensional metal structures with nano-scale resolution and structural strength comparable to established AM processes.

**Microstructure and chemical composition**

Chemical composition of the as-fabricated Ni architectures was characterized using Energy-Dispersive X-Ray Spectroscopy (EDS), for which we fabricated individual unit cells with tetrakaidecahedron geometries using the same methodology. EDS characterization was performed using a Zeiss 1550VP FESEM equipped with an Oxford X-Max SDD system using 10 kV electron beam.

Figure 3.1a shows that these structures shrunk from 20 µm-wide unit cells and 2 µm-diameter beams on 6 µm pillar supports to 4 µm unit cells and 0.4 µm-diameter beams after pyrolysis (Figure 3.1b).
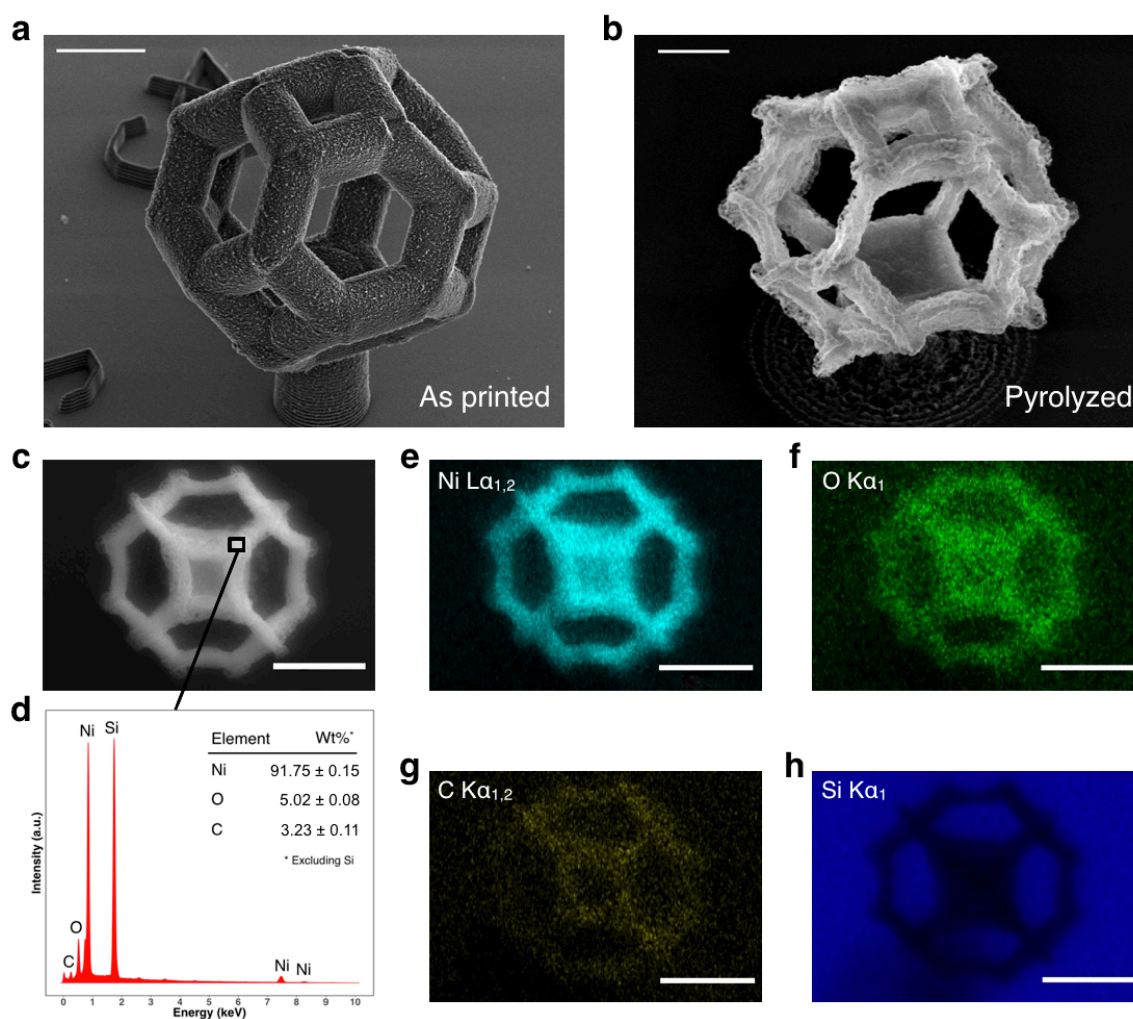


Figure 3.1. Energy Dispersive Spectroscopy (EDS) characterization of fabricated metal nanostructures.

**a** SEM images of supported 20 µm tetrakaidekahedron unit cell on a Si chip before pyrolysis and **b** the same structure after pyrolysis (4 µm width). **c** SEM image of the structure showing where EDS data was collected. **d** EDS spectrum taken within the beam of the structure suggests that the chemical composition is more than 90 wt% nickel. **e-h** EDS maps show high uniformity of the atomic composition throughout the structure. Scale bars are 5 µm for **a**, 1 µm for **b** and 2 µm for **c, e-h**.

EDS spectrum (Figure 3.1d) taken from a beam section shown in Figure 3.1c reveals the chemical composition to be 91.8 wt% Ni, 5.0 wt% O, and 3.2 wt% C. A Si peak from the substrate is also present. EDS maps in Figure 3.1e-h convey a relatively homogeneous distribution of each element within the printed structure, which consists mostly of nickel metal and is not segregated into individual nickel-, carbon-, or oxygen-rich phases.

We also fabricated some few-micron long, 25-100 nm-diameter metal beams that spanned the 1.25 μm-wide opening in a silicon nitride membrane directly on the Transmission Electron Microscopy (TEM) grids (Figure 3.2a) to analyze the atomic-level microstructure of pyrolyzed materials. Figure 3.2b displays a bright-field TEM image taken along a portion of that beam that reveals multiple coalesced grains with mean size of $21.4 \pm 2.0$ nm. The electron diffraction pattern (Figure 3.2d) taken from the region shown in Figure 3.2c conveys a strong Ni signal and a much weaker contribution from NiO. A representative high-resolution TEM (HRTEM) image (Figure 3.2e) of the beam edge contains multiple lattice fringes, which allowed the calculation of interplanar atomic spacings using Fast Fourier Transform (FFT). We identified three distinct spacings: Ni crystals (region 1, spacings of 2.01Å and 2.04Å), $Ni_3C$ particles (region 2, spacings of 1.98Å and 2.14Å), and NiO crystals (region 3, spacing of 2.06Å). Bright-field TEM revealed that Ni crystals occupy >90% of the examined volume, NiO <10%, and $Ni_3C$ <1%, consistent with EDS results (Figure 3.1d). TEM analysis further revealed the presence of nickel (II) oxide nanoparticles with diameters of < 5nm at the surface that were likely formed through surface oxidation in air after sample preparation.
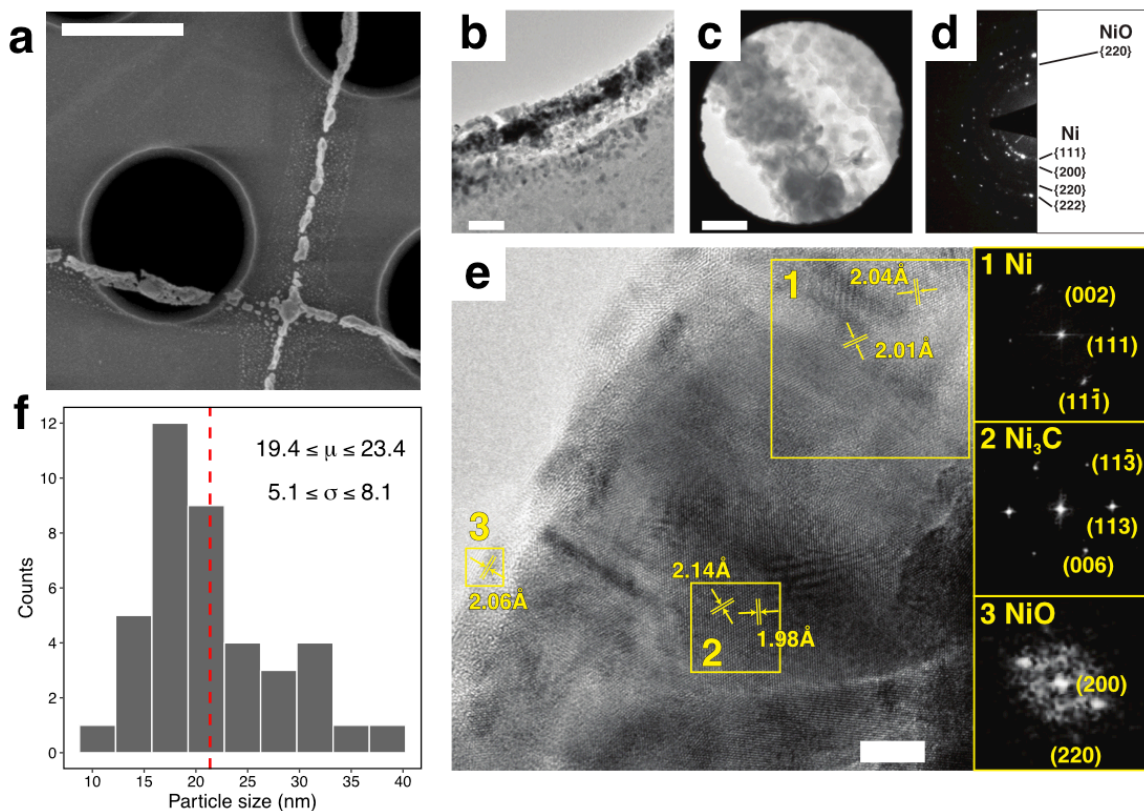
Figure 3.2. TEM characterization of the resulting metal structure.

**a** SEM image of nickel beams fabricated directly on a 200 nm-thick SiN membrane TEM grid **b** Low-magnification TEM of a 100 nm nickel beam overhanging the edge of 1.25 μm hole in a SiN membrane. **c** TEM image of the metal sample region where the diffraction pattern was taken. **d** Electron diffraction pattern shows that the printed beam consists mostly out of polycrystalline nickel with a small amount of nickel oxide. **e** HRTEM image of a printed metal beam. Analysis of atomic plane distances using FFT shows predominantly polycrystalline nickel (region 1) with some amount of nickel carbide within the structure (region 2) and nickel oxide at the surface of the structure (region 3). **f** Grain size histogram for n=40 particles measured from a TEM image showing 95% confidence intervals for the mean grain size ($\mu$) and the standard deviation ($\sigma$). Scale bars are 1 μm for **a**, 100 nm for **b**, 50 nm for **c**, and 5 nm for **e**.

Our pyrolysis is equivalent to carbothermal reduction at 1000˚C followed by reduction by hydrogen and carbon at 600˚C, with no oxygen present in the flowing gas. Literature on this type of thermal treatment reported the composition to be mainly metallic nickel with a minor amount of nickel carbide and/or carbon [116].

**In-situ compression of as-fabricated nickel nanolattices**

We conducted uniaxial compression experiments on ten Ni octet nanolattices with relative densities of 27-42% and beam sizes of 300-400 nm (see Appendix A). The experiments were conducted in-situ, in a SEM-based nanomechanical instrument, comprised of nanoindenter-like module (Nanomechanics, Inc.) inside of SEM chamber (Quanta 200 FEG, FEI), which enabled observing the deformation while simultaneously collecting load vs. displacement data[117] (see Supplementary Movie 1). The collected data was converted into engineering stresses and strains by dividing the load by the sample footprint area and dividing the displacement by the sample height, respectively. Figure 3.3(a-d) shows SEM snapshots obtained during a compression experiment of a representative sample; stress vs. strain data for four representative samples is shown in Figure 3.3e. All stress-strain data appears to be self-consistent and reproducible. A toe region in the initial portion of each experiment (not shown) is representative of deformation before establishing full contact between the sample and flat punch indenter tip. The toe region also included the failure of the supporting pillar, which allowed for establishing full contact between the sample and the substrate.

We found that the stress vs. strain data was typical for cellular solids compressions, with the characteristic elastic loading, plateau, and densification sections[118]. The arrows on the plot are correlated with the images above and demarcate specific stages during compression: initial contact (region A), elastic deformation (region B), layer-by-layer collapse (region C), and densification (region D). The point of full contact was determined using harmonic contact stiffness and SEM video. The slope of the elastic loading segment, up to 10-15%

strain (region B), was used to estimate structural stiffness of the nanolattices, which ranged from ~47 to 174 MPa.
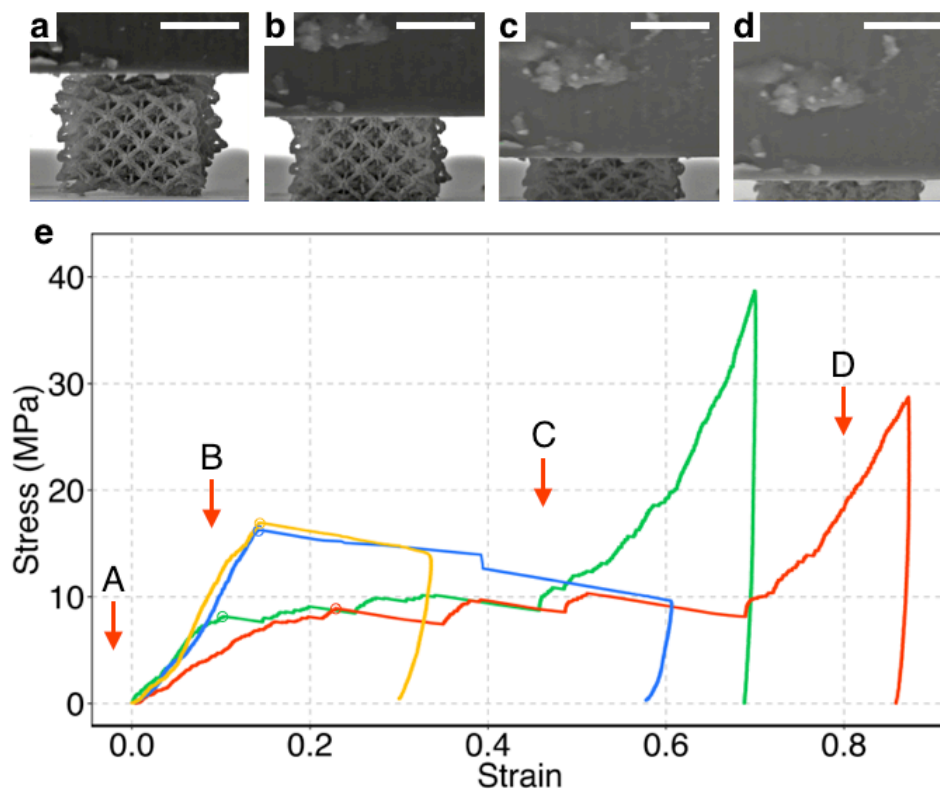


Figure 3.3. *In-situ* uniaxial compression of 3D printed nickel octet nanolattices.

**a-d** SEM images of the nickel structure during the compression test **a** before full contact, **b** in the elastic regime, **c** during layer-by-layer collapse, and **d** during densification. **e** Stress-strain diagram showing compression of four nickel nanolattices. Letters on the graph correspond to the regions represented by **a-d**. See Appendix A for data and references. Scale bars are 5 μm for **a-d**.

The strength of Ni nanolattices was defined as the maximum stress prior to the first buckling event, marked by open circles in the data in Figure 3.3e, and ranged from 6.9 MPa to 18.2 MPa. The elastic region was followed by layer-by-layer collapse up to 65% strain (region C); two of the four samples were unloaded at 30 and 60% strain. The two other samples were

compressed to 70-85% strains, reached densification (region D) and then unloaded (see Supplementary Movie 1). None of the nanolattices recovered after deformation.

**Comparison of the specific strength to state-of-the-art AM processes**

Figure 3.4 shows the specific strength of Ni nanolattices fabricated in this work and those of the metallic lattices fabricated using other metal AM processes as a function of beam diameter on a log-log plot (see Appendix A for details).
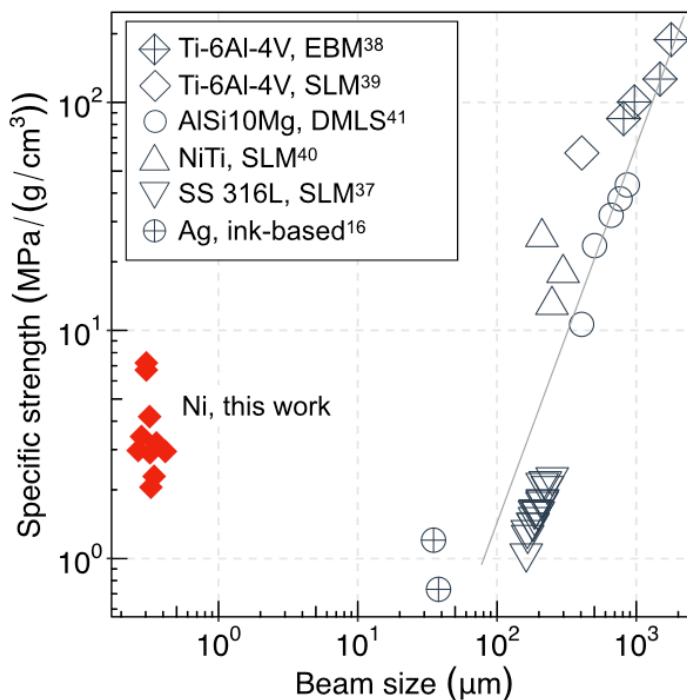


Figure 3.4. Specific strength-beam size plot showing properties of nickel nanolattices compared to other metal AM processes.

Metallic lattices fabricated using Selective Laser Melting (SLM), Direct Metal Laser Sintering (DMLS), Electron Beam Melting (EBM), and ink-based methods are shown for comparison.

Specific strength values shown in Appendix A were calculated as the lattice strength divided by the lattice density. Lattice density values were taken from refs. [29,119,120]

as reported. For structures in refs. [121–123] the lattice density was estimated as a product of the material density and the relative density of the structure. The material density of SLM NiTi was provided in ref. [121]. The material density of EBM Ti-6Al-4V in ref. [122] was assumed to be similar to Grade 5 Ti-6Al-4V, 4.43 $g/cm^3$, the closest material to Arcam Ti-6Al-4V ELI used in that work[124]. The material density of DMLS AlSi10Mg in ref. [123], 2.67 $g/cm^3$, was taken from the material datasheet[125]. Beam diameter values in refs. [29,119,121,122] were taken as reported. Beam diameters for AlSi10Mg lattices were estimated from Fig. 10 and Fig. 12 in ref. [123]. Beam diameters for SLM Ti-6Al-4V were measured from Fig. 2 in ref. [120]. For electroplated copper meso-lattices in ref. [11] specific strengths were calculated assuming bulk copper density of 8.96 $g/cm^3$.

This plot reveals that the specific strength of metallic lattices in refs.[29,119–123] decreases by a factor of 280 as the beam diameter is reduced from 1.78 to 0.04 mm, with the lowest reported specific strength of 0.7 $MPa/(g/cm^3)$ for octahedral silver lattices. Nanocrystalline Ni nanolattices in this work have the specific strength of 2.1-7.2 $MPa\ g^{-1}\ cm^3$, which is ~2-10x higher than that of octahedral silver lattices with ~40 μm-diameter beams[29] and ~2-7x higher than the stainless steel lattices with ~200 μm-diameter beams[119]. It appears to be on the same order as NiTi octahedral lattices with ~250 μm-diameter beams[121] and AlSi10Mg diamond lattices with ~400 μm beams[123]. The specific strength calculations were performed with the assumption of monolithic beams, which leads to its underestimation because the nanocrystalline Ni within the beams has 10-30% residual porosity. This suggests that the AM process developed in this work is

capable of producing architectures with feature sizes that are an order of magnitude smaller than those fabricated using existing AM processes while retaining high strength.

**Discussion**

EDS analysis revealed that the fabricated nanolattices have a composition of 91.8 wt% Ni, 5.0 wt% O, and 3.2 wt% C. It is reasonable to expect traces of carbon in the pyrolyzed structures caused by the high solubility of carbon in Ni at 1000°C [126], which leads to carbon precipitation at nickel surface upon cooling down to room temperature. TEM analysis revealed that the carbon also exists in the form of 5 nm-sized $Ni_3C$ precipitates within the beams (Fig. 3e). The accuracy of EDS in quantifying the carbon content may not be sufficient because it is sensitive to the spurious carbon deposited in the SEM chamber[127]. The presence of 5.0 wt% O in the nanolattice can be attributed to formation of a native oxide on Ni surface and to full oxidation of small (<6 nm) Ni surface nanoparticles [128].

The specific strength of the Ni nano-lattices in this work is 50-80% lower than that of Cu meso-lattices with a similar relative density reported in ref. [11], which likely stems from the lattice strength being governed by that of the monolithic, fully-dense beams with grains spanning full beam width. The strength of nanoporous Au stochastic foams in ref. [129] was reported to be close to that of monolithic gold because each ligament is a virtually defect-free, single crystalline beam, whose strength approaches ideal strength of gold [129]. These foams have a fundamentally different microstructure compared to the nanolattices in this work in that they are stochastic foams with relatively slender, curved single-crystalline pristine beams. A direct comparison between the compressive strengths of nanocrystalline Ni nanolattices in this work and those of hollow lattices reported in

refs. [12,14,15,117,130] may be misleading, because this work is focused on solid-beam metallic nanolattices, which deform via compression and plastic flow upon uniaxial compression; the others contain hollow shell beams and undergo a different deformation mechanism upon compression that includes shell buckling and layer-by-layer collapse.

To summarize, we developed an additive manufacturing (AM) process to create 3D nano-architected metals using an effective lithography-based approach. Using this process, we fabricated Ni octet-lattices with 2 μm unit cells, 300-400 nm beams and 30 nm layers. The resolution of this method allows printing metal features with 25-100 nm dimensions, which is an order of magnitude smaller than feature sizes produced using all other 3D-capable metal AM methods. This nanoscale metal AM method is not limited to nickel: other organometallics can be used to derive UV-curable metal-based photoresists using similar chemical synthesis (see Figure 2.6). The following chapter explores synthesizing and utilizing titanium-based hybrid materials for nanoscale AM in more detail.

# CHAPTER 4 : **NANOSCALE AM** OF METAL OXIDE CERAMICS: PHOTONICS

**Chapter Summary**

Material choice for nanoscale AM remains extremely limited; in particular, a dearth of transparent materials with high refractive index exists. State-of-the-art AM processes for high refractive index materials suffer from high stochastic porosity, poor repeatability, and/or require complex experimental procedures. In this chapter, we developed an AM process to fabricate complex 3D architectures out of fully dense titanium dioxide ($TiO_2$) with features as small as 120 nm. We synthesize a hybrid organic-inorganic precursor to formulate a pre-ceramic photoresist that is shaped into a designed 3D structure using two-photon lithography (TPL). The 3D pre-ceramic sample is then pyrolyzed in air at 750-900°C, which yields a ~60% linearly shrunk replica of the original structure. We demonstrate this process by fabricating woodpile face-centered tetragonal (FCT) architectures with beam dimensions between 300 and 600 nm and lateral periods of 0.84 and 1.47 μm. Energy-Dispersive Spectroscopy (EDS), Raman spectroscopy, and Transmission Electron Microscopy reveal this material to be nanocrystalline rutile TiO2, with an average grain size of 110 nm and <1% porosity. Plane Wave Expansion (PWE) simulations and Fourier-transform Infrared Spectroscopy (FTIR) reveal that these woodpile structures exhibit a full photonic bandgap centered at 1.8-2.9 μm. The AM process developed in this work allows the creation of fully dense $TiO_2$, which has

significant impact on enabling 3D MEMS, micro-optics, and rapid prototyping of 3D

dielectric PhCs.

**Process for nanoscale AM of titanium dioxide**

To prepare titania pre-ceramic photopolymer, we first used a ligand exchange reaction

between titanium (IV) ethoxide and acrylic acid in 1:4 molar ratio to synthesize titanium

(IV) acrylate (Figure 4.1a).
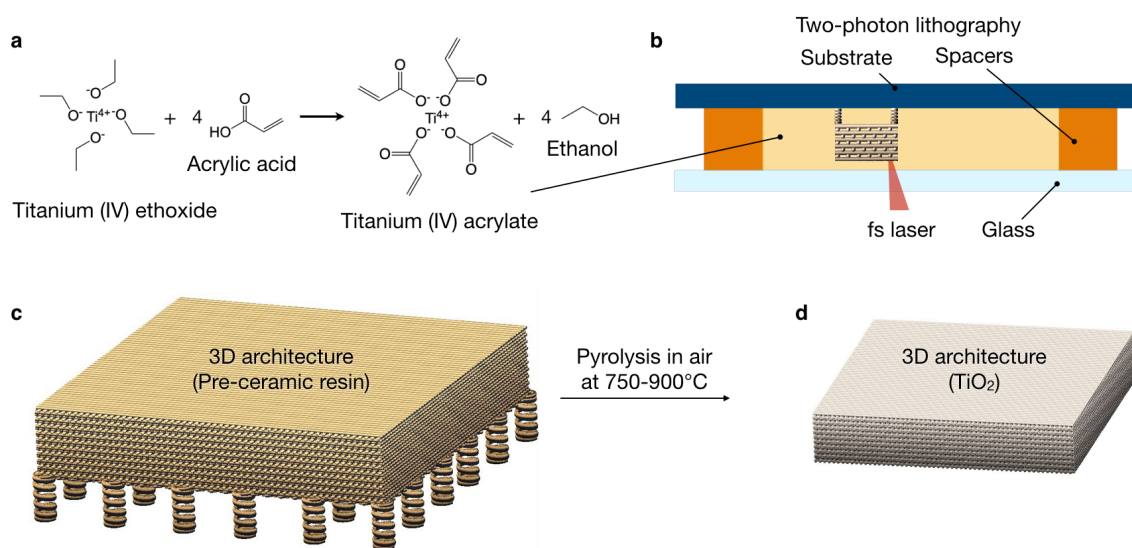


Figure 4.1. Process for nanoscale additive manufacturing (AM) of titanium dioxide

**a** Ligand exchange reaction between titanium (IV) ethoxide and acrylic acid is used to synthesize a liquid $TiO_2$ precursor in the photopolymer. **b** Titania pre-ceramic photopolymer is used in a two-photon lithography process to fabricate pre-ceramic 3D architectures. **c** Schematic of a pre-ceramic woodpile architecture supported by a set of springs that decouple it from the substrate. **d** Titania woodpile structure is formed by calcination of the pre-ceramic part.

The reaction was conducted in a glovebox to minimize exposure to oxygen and water.

The solution was then placed in a vacuum antechamber of the glovebox for 30 min to

remove ethanol produced as the result of the ligand exchange reaction. The resulting

hybrid organic-inorganic $TiO_2$ precursor can be embedded in a polymer network during free-radical polymerization. The solution was then taken out of the glovebox, mixed with 300 mg of 2-methoxyethanol and 1.2 g of pentaerythritol triacrylate, agitated for 30 s using a vortex mixer, and moved to a yellow-light area. 30 mg of 7-diethylamino-3-thenoylcoumarin was then dissolved in 150 mg of DCM and added to the mixture, followed by another agitation in the vortex mixer for 30 s. The resulting resist was then let to rest for 5 min to release air bubbles trapped as the result of the agitation.

This liquid photopolymer was then drop cast onto a silicon substrate and 3D printed in a TPL system (Photonic Professional GT, Nanoscribe GmbH). Architected samples were designed to rest on top of a 2D lattice layer supported by a spring-and-pillars array that decoupled the architecture from the substrate during pyrolysis and minimized its distortion during shrinkage [72,131] (Figure 4.1b, c). The samples were developed in 2-methoxyethanol overnight, followed by 15 min in PGMEA and 3 min in filtered IPA. The samples were then transferred to a critical point dryer (Autosamdri-931) followed by pyrolysis in air in a tube furnace using an open-ended 2" OD quartz tube. The temperature was ramped up to 900°C at 3°C/min, kept at 900°C for 1 hour, and then the furnace was let to cool down at a natural rate. (Figure 4.1d).

Two-photon lithography of custom hybrid organic-inorganic materials is a technically challenging process, and a variety of printing defects occur in attempts to fabricate 3D architectures. Figure 4.2 shows representative failed prints that occurred as the result of using inadequate process parameters, namely the laser power and the scanning speed, that define the exposure dose. Photopolymer overexposure leads to excessive polymer shrinkage that results in structure warping and delaminating from the substrate (Figure

4.2, left). Resist underexposure results in smaller and weaker features that may no longer be connected to each other, leading to the loss of connectivity throughout the part (Figure 4.2, right). The following section explores the ability to predict and reliably control feature dimensions in hybrid materials using a model that links voxel dimensions to process parameters in TPL.

**Post-printing shrinkage**　　　　　　　　　　**Lack of connectivity**
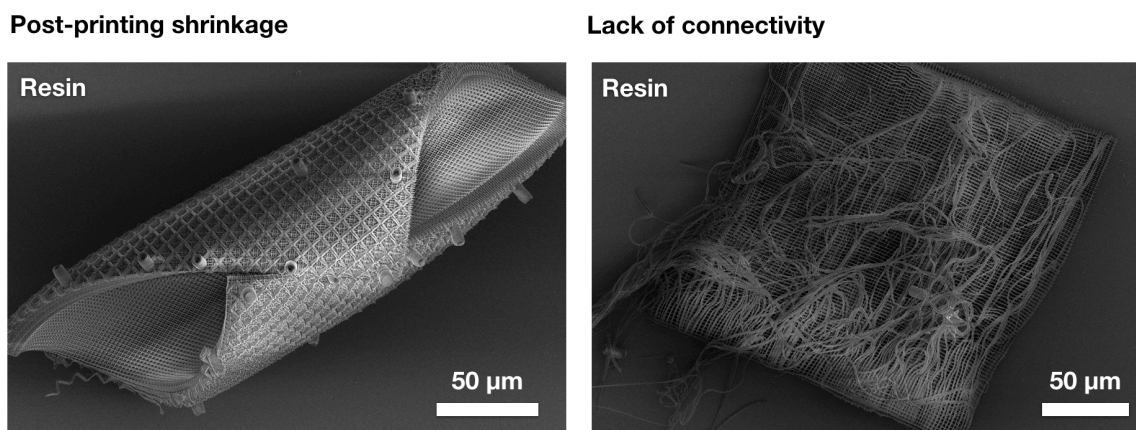


Figure 4.2. SEM images of TPL-fabricated resin 3D structures showing representative printing defects

**Predicting voxel dimensions in two-photon lithography of hybrid materials**

Print defects described above stem from a poor choice of the laser power and/or the scanning speed used for selective cross-linking of the photopolymer. In addition to the print success, these process parameters affect the minimal feature size that can be attained in TPL. Previous studies [132–134] reported strong non-linear dependence of the dimensions of the polymerized material, or voxel (Figure 4.3, left), on the laser power (LP) and the exposure time (ET) in two-photon lithography. This relationship, which was shown to be unique for each photopolymer, ultimately defines the feature dimensions and how well a 3D geometry can be replicated by hatching and stacking individual cross-

linked lines in the resist  (Figure 4.3, center and right). To ensure high accuracy of

geometric dimensions in devices fabricated using this AM process, we carefully studied

the influence of process parameters on the size of individual features.

**Single voxel**  **Feature**  **Layer-by-layer**

Axial diameter, L

Lateral diameter, d

Hatching distance

Layer Thickness
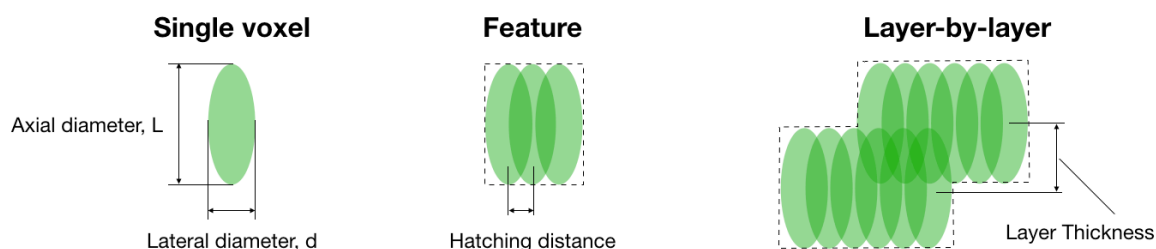
Figure 4.3. The importance of predicting the voxel size for control of
feature dimensions in two-photon lithography

Voxel axial diameter, L and lateral diameter, d (left) determine the minimal feature
dimensions (center) and how closely a 3D geometry can be replicated (right)

We used ascending scan experiments [132] to evaluate the voxel width and height for this

hybrid photoresist for LP between 12.5 and 20 mW and ET between 0.5 and 10 ms.

Figure 4.6 shows that for ET between 1 ms and 10 ms at 20 mW, the voxel width varied

from 440 to 560 nm, its height changed from 1.6 to 3.2 µm, and the voxel aspect ratio

varied from 3.8 to 5.3.

Estimating polymerization volume in two-photon lithography generally requires

numerical simulations that take into account radical generation and inhibition, oxygen

diffusion, local heating, and many other factors [134]. We studied the dependence of the

voxel dimensions on the exposure parameters by examining polymerization kinetics

inside the voxel volume at millisecond time scales. Mueller et al. [135] experimentally

showed that at exposure times between 1 and 10 ms two-photon polymerization is

primarily driven by radical generation. Uppal et al. found that the generated radicals

remain mostly confined to the voxel volume during the exposure [134]. Mueller et al.

[136] has demonstrated that the temperature inside the polymerizing voxel did not increase by more than 5K at 20 mW laser power. These previous studies allowed us to adopt a modeling approach by Serbin et al. [133] for an isothermal system with no diffusion to predict the voxel dimensions in our system.

We start by assuming a Gaussian shape of the laser beam that is focused through a 63x microscope objective (NA=1.4). Photon flux for the pulsed Gaussian beam $N(r, z, t)$ can be expressed as

$$N(r, z, t) = N_0(t) \frac{w_0}{w(z)} e^{-\frac{2z_R^2}{w(z)^2}}$$
(4.1)

where $z_R$ is the Rayleigh distance [nm], $w_0$ is the laser beam waist [nm], $N_0(t)$ is the photon flux in time, and $w(z)$ is the beam width in the z direction. Figure 4.4 shows a schematic that illustrates the beam shape profile along the axial direction (z).
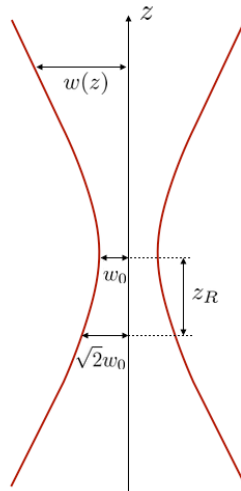


Figure 4.4. Schematic of a focused Gaussian beam used for modeling the exposure pattern in TPL

For a two-photon process, the density of radicals generated with time $\rho(r,z,t)$ depends on the square of the photon flux as

$$\frac{\partial \rho(r,z,t)}{\partial t} = \sigma_2(\rho_0 - \rho(r,z,t))N(r,z,t)^2 \tag{4.2}$$

where $\sigma_2$ is the effective two-photon cross-section [cm$^4$ s], and $\rho_0$ is the photoinitiator density [wt%].

We assume that the material is cross-linked within the volume where the density of radicals reaches $\rho_{th}$, the threshold density of radicals required for polymerization [wt%] (see Figure 4.5).
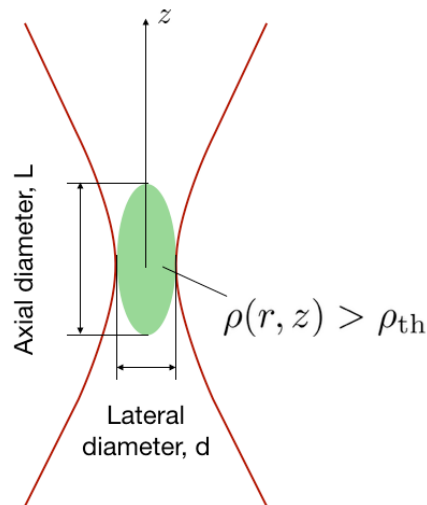


Figure 4.5. Modeling voxel dimensions using radical concentration profile within a focused Gaussian beam.

Voxel is defined as a volume of the photopolymer where the density of radicals reaches a threshold value

To solve for the voxel width $d$, or the lateral diameter (see Figure 4.5), we consider the photon flux profile (Equation (4.1)) for $z = 0$:

$$N(r,t) = N_0(t)e^{-\frac{2z_R{}^2}{w_0{}^2}} \tag{4.3}$$

Similarly, to solve for the voxel height $L$, or the axial diameter (see Figure 4.5), we consider the photon flux profile (Equation (4.1)) for $r = 0$:

$$N(z,t) = \frac{N_0(t)}{\frac{z^2}{z_R{}^2} + 1} \tag{4.4}$$

As discussed above, the generated radicals remain mostly confined to the voxel volume between femtosecond laser pulses [134], so the photon flux $N_0(t)$ can be expressed as average photon flux over the exposure time:

$$N_0(t) = N_0 = \frac{2(P\Gamma)}{(\pi w_0{}^2 \tau_L)(v\hbar\omega_L)} \tag{4.5}$$

where $N_0$ is the average photon flux, $P$ is the laser power, $\Gamma$ is the fraction of light reaching the photoresist, $\omega_L$ is the laser frequency, $v$ is the laser pulse repetition rate [Hz], and $\tau_L$ is the laser pulse duration [s].

The solution of Equation (4.2) subject to condition (4.3) and $\rho(r,z) > \rho_{th}$ gives us the voxel width $d$:

$$d = w_0 \sqrt{\log\frac{v N_0^2 \sigma_2 t \tau_L}{C}} \tag{4.6}$$

where $C = \log\frac{\rho_0}{\rho_0 - \rho_{th}}$, and $t$ is the exposure time [s].

Similarly, the solution of Equation (4.2) subject to condition (4.4) and $\rho(r,z) > \rho_{th}$ gives us the voxel height $L$:

$$L = 2z_R \sqrt{\sqrt{\frac{\nu N_0^2 \sigma_2 t \tau_L}{C}} - 1} \qquad (4.7)$$

This means that the voxel height $L$ and the voxel width $d$ can be ultimately expressed as a function of the laser power $P$ and the exposure time $t$ as

$$L = 2z_R \sqrt{\sqrt{\alpha t P^2} - 1} \qquad (4.8)$$

$$d = w_0 \sqrt{\log[\alpha t P^2]} \qquad (4.9)$$

where $\alpha = \frac{\nu \sigma_2}{C \tau_L} \left[\frac{2\Gamma}{(\pi w_0{}^2)(\nu \hbar \omega_L)}\right]^2$.

Based on the experimental setup, we set $\tau_L = 80\ fs$, $\lambda = 780\ nm$, $\nu = 80\ MHz$, and assume $\Gamma = 0.15$, and $\sigma_2/C = 2.76 * 10^{-54} cm^4\ s$. The fit parameters for the model shown Figure 4.6 were $z_R = 430\ nm$, $w_0 = 245\ nm$.
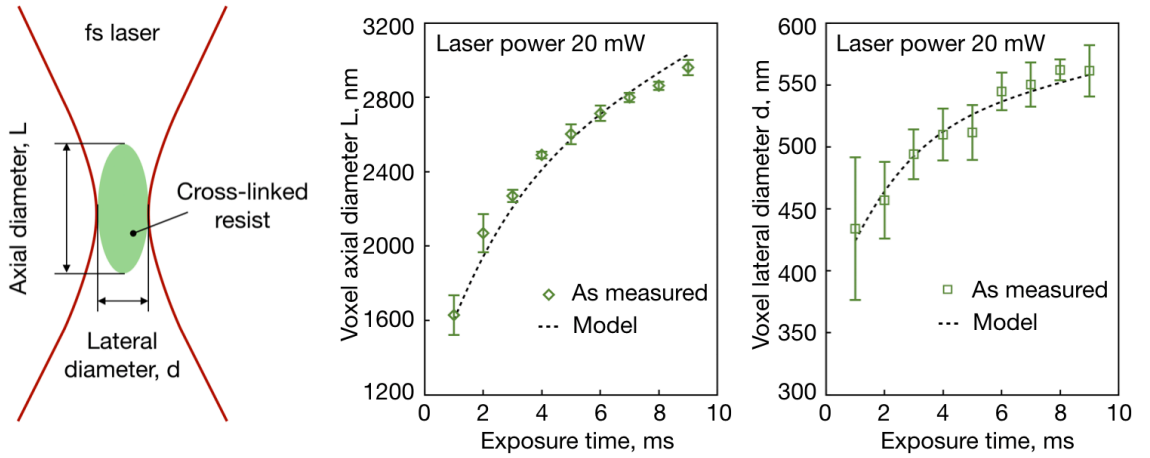


Figure 4.6. Predicted and measured voxel dimensions for the hybrid titania resist for a constant laser power of 20 mW as a function of the exposure time.

Figure 4.6 demonstrates that experimentally measured voxel dimensions are in good agreement with this model, which provides a quantifiable way to tailor the laser exposure parameters to achieve target feature dimensions.

**Accuracy and repeatability of geometrical features**

We demonstrate the efficiency of this approach by fabricating 3D architectures with tetragonal woodpile geometry that has overall dimensions of 220 x 220 µm, a lateral period $x_L$ of 3.7 µm, an axial factor (defined as the ratio of the axial period $x_a$ to the lateral period $x_L$) of 1.1, and rectangular beams with 1.3 x 1.5 µm cross-sections (Figure 4.7a, c).
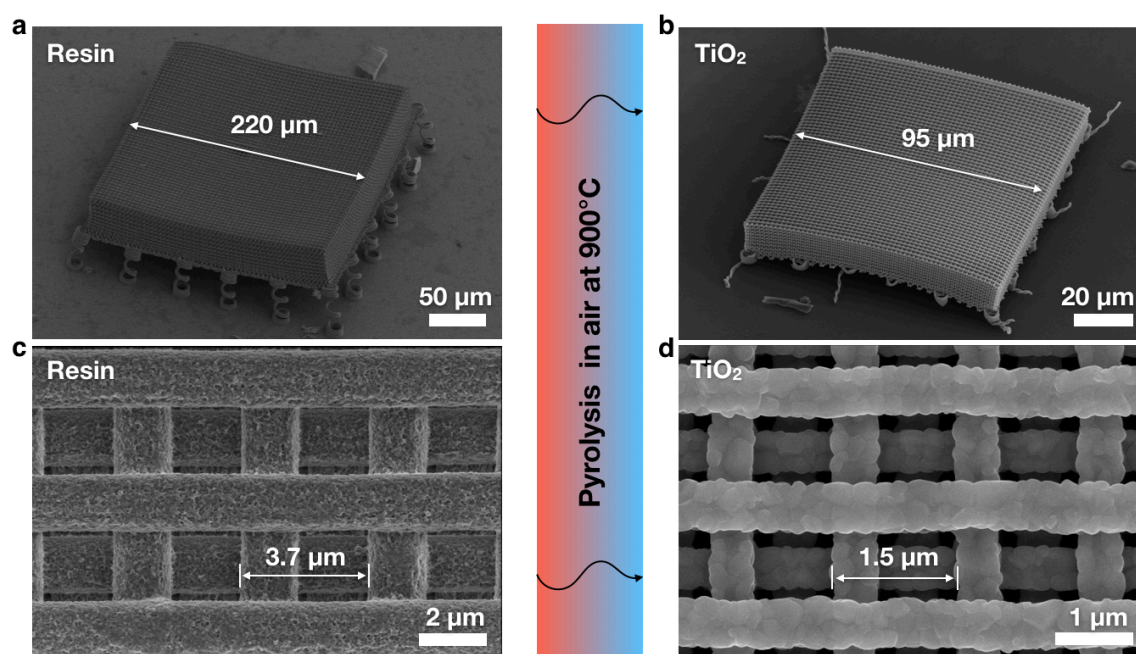


Figure 4.7. SEM characterization of as-fabricated $TiO_2$ 3D architectures.

**a, c** Representative SEM images of pre-ceramic woodpile architectures. **b, d** Representative $TiO_2$ woodpile architectures after calcination at 750-900°C.

Figure 4.7b, d shows SEM images of a representative woodpile structure after pyrolysis that contains 60 periods in the lateral direction and 9 periods in the axial direction. The beams in this sample had 530 x 600 nm rectangular cross-sections, a lateral period of 1.47 μm, and overall lateral dimensions were 95 x 95 μm. The features appeared to be uniform, and the shrinkage post-pyrolysis appeared to be isotropic.

To quantify the effect of shrinkage on geometrical distortions within the structure, we analyzed the variability of geometric dimensions in axial and lateral directions in the woodpile using SEM measurements (Figure 4.8).
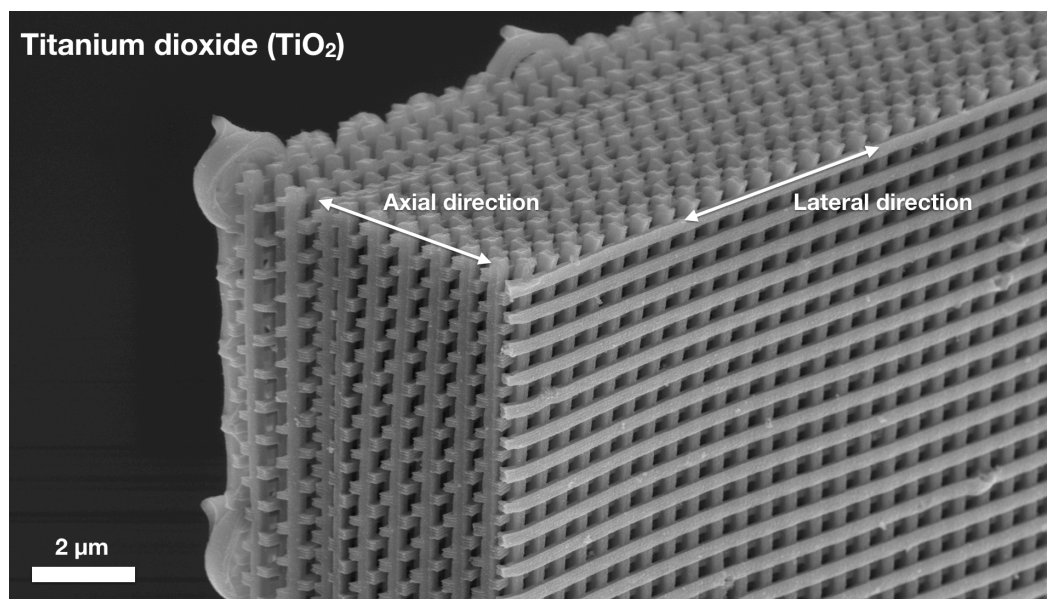


Figure 4.8. SEM image of as-fabricated woodpile FCT architecture showing lateral and axial directions within the crystal
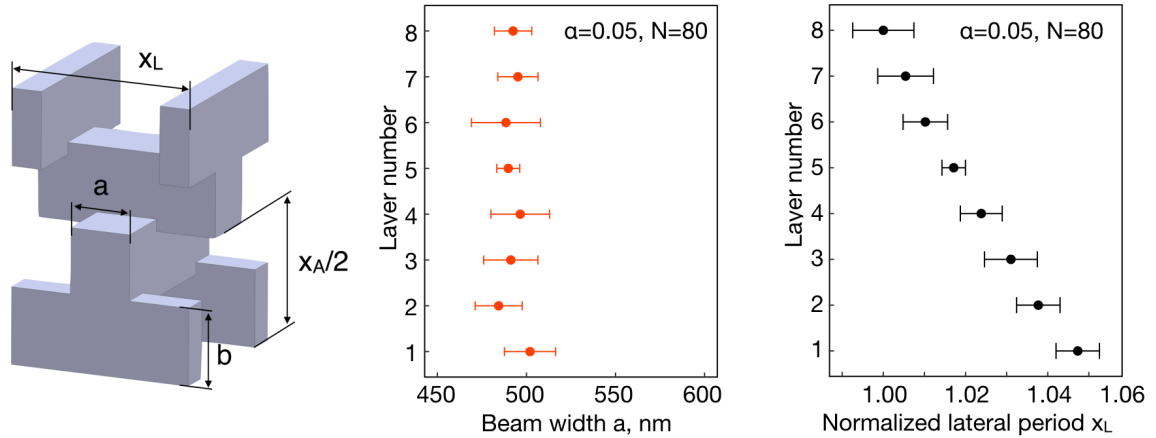
Figure 4.9. Beam widths and lateral periods in the axial direction of as-fabricated titania woodpile as measured by SEM

We found that in the axial direction the lateral period did not vary by more than 5%, with no statistically significant deviations in the average beam width (see Figure 4.9).

In the lateral direction, we analyzed the variability of the lateral period using analysis of variance (ANOVA) [137]. The experimental setup for ANOVA used a nested design with three locations within the part (the center of the structure and two off-center locations), three magnifications at which the SEM measurements were taken, and eight measurements of the average lateral period at each magnification (see Figure 4.10). The underlying model for the measured lateral period took into account the effect of location, the effect of SEM image magnification, and the error (see Figure 4.10).
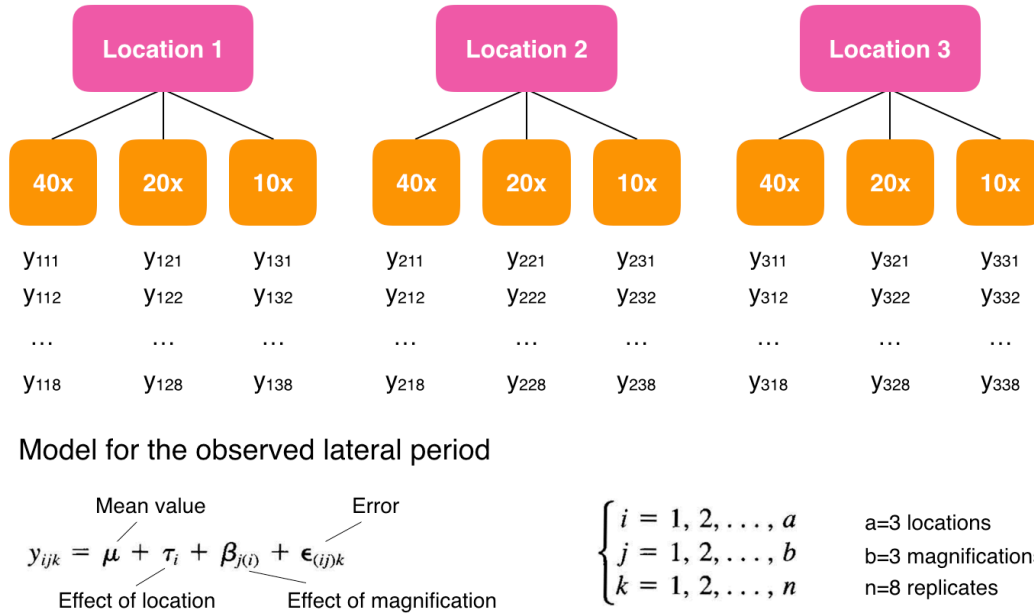
Figure 4.10. Experimental design for a nested variance analysis of geometric feature size variation in the lateral direction

The results of ANOVA and nested variance analysis are shown in Table 4.1. We found a strong effect of the location within the structure ($p<0.01$) and no effect of SEM magnification ($p>0.5$), suggesting spatial variation of the measured lateral period. The analysis revealed a total variability of 25 nm, or 1.7% of the target dimension, across the entire sample. We also found that the contribution of spatial variability of the lateral period was only 13 nm, or less than 1% of the target. The implications of spatial variation of geometrical parameters for the optical properties of photonic crystals are further discussed in the Optical behavior of as-fabricated photonic crystals and Discussion sections of this chapter.

Table 4.1. Nested variance analysis of the lateral period in the top layer of as-fabricated woodpile structure

| Source of variation | Sum of squares | Degrees of freedom | Mean square error, MSE | F0 | p-value |
|---|---|---|---|---|---|
| Locations | 8536.38 | 2 | 4268.19 | 11.33 | **0.009** |
| Magnifications | 2259.64 | 6 | 376.61 | 0.86 | 0.529 |
| Error | 27581.52 | 63 | 437.80 | | |
| Total | 38377.53 | 71 | | | |

| | Sigma, nm | Contribution |
|---|---|---|
| Error | 20.92 | 73.0% |
| Magnification | | |
| Location | 12.73 | 27.0% |
| Total | 24.49 | 100.0% |

**Material characterization**

To characterize the chemical composition of as-fabricated material, we conducted energy-dispersive X-ray spectroscopy (EDS) on a representative sample with in-plane dimensions of 95 x 95 μm and a lateral period of 1.5 μm (Figure 4.11a). SEM EDS was conducted using Zeiss 1550VP FESEM equipped with Oxford X-Max SDD. SEM EDS maps (Figure 4.11b-d) show a uniform distribution of Ti and O throughout the structure with no apparent segregations into titanium- or oxygen-rich phases. EDS spectrum taken from a 20 x 20 μm area in the center of the sample (Figure 4.11e) reveal the chemical composition to be 66.8 at% oxygen and 33.2 at% titanium. Silicon substrate was excluded from the composition estimate.
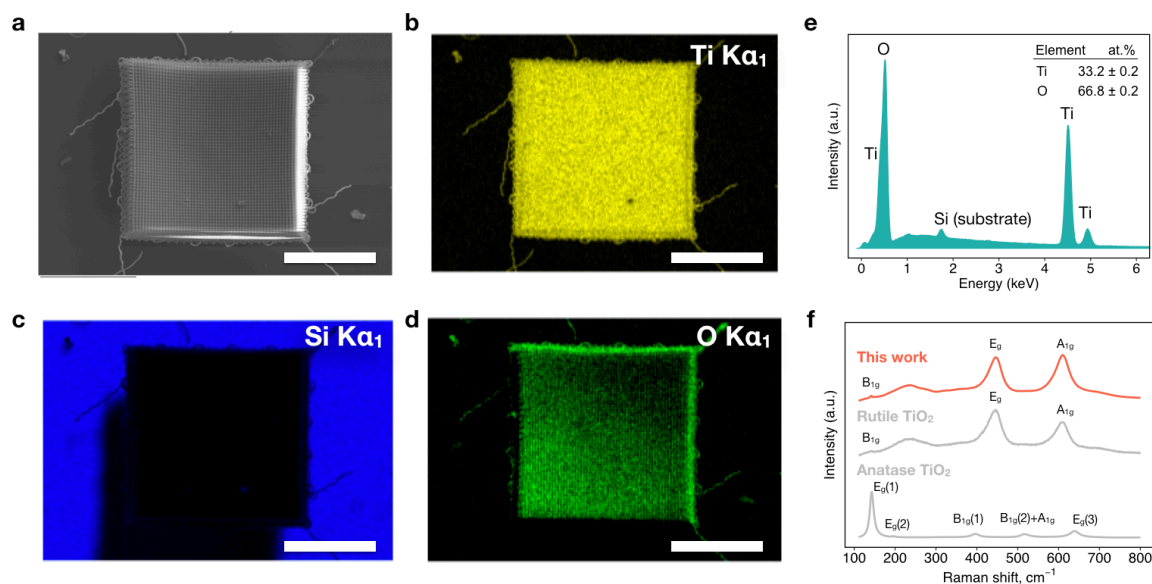
Figure 4.11. Characterization of chemical composition and phase of $TiO_2$ using SEM EDS and Raman spectroscopy.

**a-d** SEM EDS mapping of a representative woodpile architecture fabricated on a silicon substrate reveals uniform distribution of titanium and oxygen. **e** Estimation of chemical composition from a representative EDS spectrum shows 1:2 at% ratio of titanium to oxygen consistent with $TiO_2$. **f** Raman spectrum of as-fabricated TiO2 compared to reference spectra of rutile and anatase. Scale bars are 50 µm for **a-d**

To evaluate the phase composition, Raman spectra were collected from the as-fabricated 3D architectures using a 514 nm laser focused through a 50x microscope objective. Raman spectra were collected using Renishaw M1000 MicroRaman Spectrometer. Samples of rutile and anatase titanium dioxide for reference Raman spectra were provided by Prof. George Rossman (Caltech). Figure 4.11f shows a representative Raman spectrum along with the reference spectra collected from rutile and anatase samples. The Raman signature revealed peaks at 145 $cm^{-1}$, 448 $cm^{-1}$, and 613 $cm^{-1}$ that match the rutile reference spectrum.

We analyzed the atomic-level microstructure of as-fabricated $TiO_2$ structures using Transmission Electron Microscopy (TEM) and electron diffraction. We prepared a 100 nm-thick cross-section of a sample whose beams had 960 x 150 nm elliptical cross-

sections, lateral periodicities of 1090 nm, and a footprint of 70 x 70 μm using Focused

Ion Beam (FIB) lift out procedure (Figure 4.12a). High-resolution (Figure 4.12b) and

dark-field (Figure 4.12c) TEM images reveal that a typical beam cross-section is >99%

dense and is comprised of nanocrystallites with a mean size of 110 nm (see Figure

4.12d). Electron diffraction pattern (Figure 4.12b, inset) confirms the crystalline phase of

$TiO_2$ to be rutile.
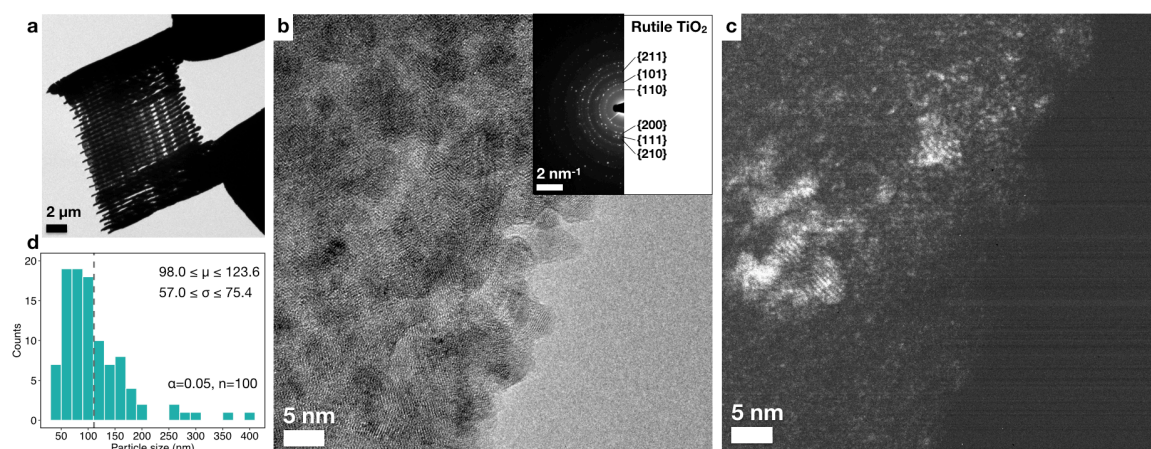


Figure 4.12. TEM characterization of as-fabricated $TiO_2$ 3D architectures.

**a** Low-magnification TEM image showing a 100 nm thick cross-section of a $TiO_2$ woodpile structure prepared using FIB lift-out procedure. **b** HRTEM image of a cross-section of an individual beam, an electron diffraction pattern (inset), and **c** a corresponding dark-field TEM image reveal that the beams consist predominantly out of nanocrystalline rutile $TiO_2$. **d** Grain size histogram for n=100 particles measured from an SEM image showing 95% confidence intervals on the mean grain size (μ) and the standard deviation (σ)

We characterized optical properties of as-fabricated titania using ellipsometry. A 2 x 2

mm thin film of titanium dioxide with approximately 100 nm thickness for ellipsometry

measurements was fabricated on silicon using the method described above. Figure 4.13

(left) shows a representative SEM image of as-fabricated titania films on silicon and

reveals that the film is porous. Ellipsometry data was collected at wavelengths between

275 nm and 2 μm with a 0.5 mm spot size. The n, k data fitted using Forouhi-Bloomer model[138] with $\varepsilon_\infty$=4.2344, A = 0.06053, B = 7.6778, C = 15.8439, and Eg = 0.09476 ($\chi^2$=39.1) is shown in Figure 4.13 (right) . Comparison between the collected n,k data and TiO2 properties found in the literature can be found in the Discussion section of the manuscript.
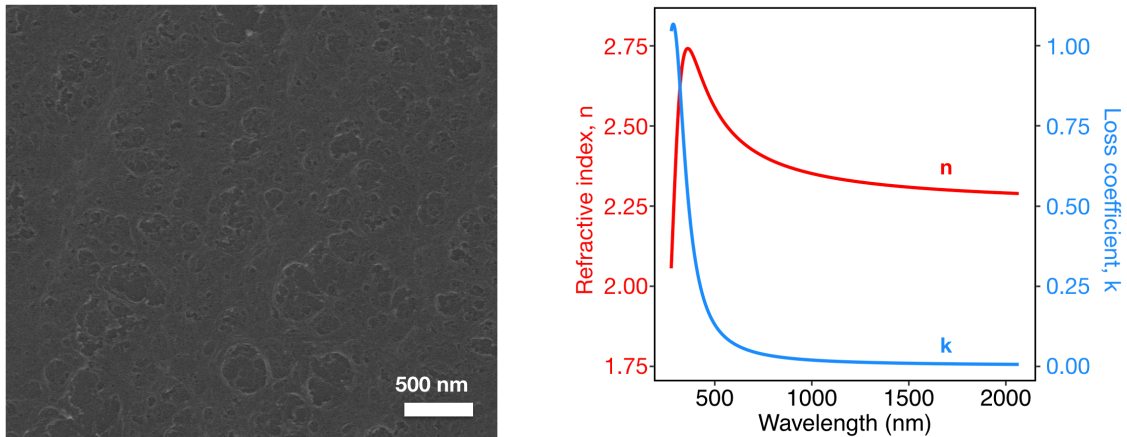


Figure 4.13. SEM image of a 100 nm-thick film of TiO$_2$ on Si prepared for ellipsometry measurements and ellipsometry data for wavelengths between 275 nm and 2 μm

**Optical behavior of as-fabricated photonic crystals**

We used Plane Wave Expansion (PWE) simulations and Fourier Transform Infrared Spectroscopy (FTIR) measurements to investigate the optical behavior of TiO$_2$ woodpiles. We chose experimentally-equivalent geometric parameters extracted from images in Figure 4.7d and a refractive index of 2.3, obtained by ellipsometry measurements on as-fabricated films (Figure 4.13) for PWE simulations.

Figure 4.14 and Figure 4.15c show the  band diagram calculated for an FCT woodpile architecture (Figure 4.15a) with these dimensions. The corresponding Brillouin zone is

shown in Figure 4.15b. PWE simulations reveal that this woodpile architecture exhibits a full photonic bandgap between frequencies of $0.465(2\,\pi c/x_L)$ and $0.474(2\,\pi c/x_L)$, where $x_L$ is the lateral period of the woodpile and c is the speed of light. Woodpiles with $x_L$ of 1.47 μm have gap edges at 3.10 and 3.16 μm (see Table 4.2).
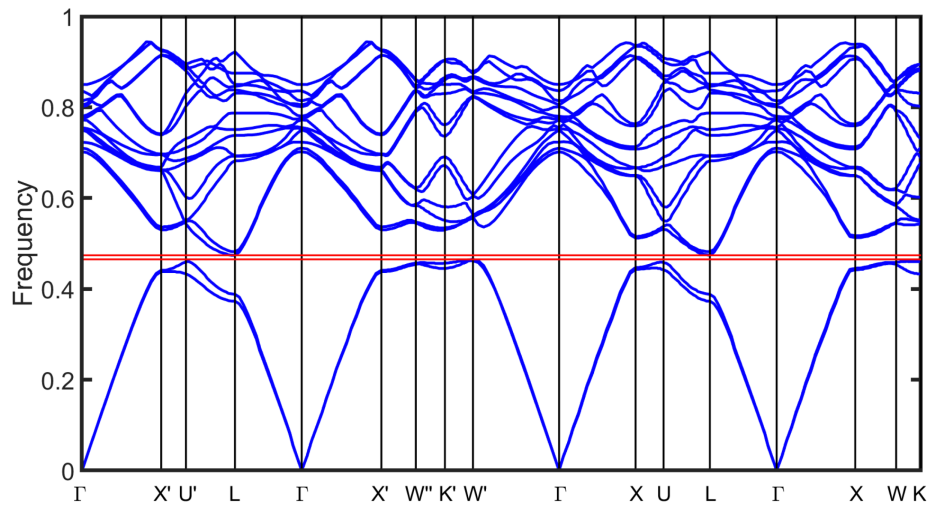


Figure 4.14. Band diagram from PWE showing the emergence of a full photonic bandgap in a simulated woodpile tetragonal architecture

To probe the simulation results experimentally, we measured the reflectance and transmittance of the as-fabricated woodpiles using FTIR with a Cassegrain objective with an angle range between 16° and 35.5° within a 30 x 30 μm area at the center of the sample. Reflectance and transmittance spectra were collected using Nicolet iS50 FT-IR spectrometer equipped with a Nicolet Continuum Infrared Microscope, a calcium fluoride beam splitter, and an infrared light source. Background signal was collected from double-sided polished silicon that served as a substrate for the samples. Reflectance spectra were normalized by the maximum value of reflectance within the high reflectance band.

Previous experimental studies revealed that the position of FTIR reflectance bands is influenced by the stop-band positions that are being probed simultaneously at off-normal light incidences [76]. We calculated the expected stop-band edges from the woodpile band diagram probed along X'-U'-L and X'-W'-K' at experimental off-normal incidence angles to be between $0.418(2\,\pi c/x_L)$ and $0.544(2\,\pi c/x_L)$, which corresponds to the wavelengths of 2.7 to 3.5 µm (Table 4.2). Figure 4.15d contains FTIR spectra that reveal a high reflectance/low transmittance band centered at ~2.9 µm, plotted along with the computed position of a full photonic bandgap (gray rectangle) and the range of stop-band positions for the 16°-35.5° incidence angles (vertical dash lines). The position of the high reflectance band was found to be within 7% from the expected full photonic bandgap.
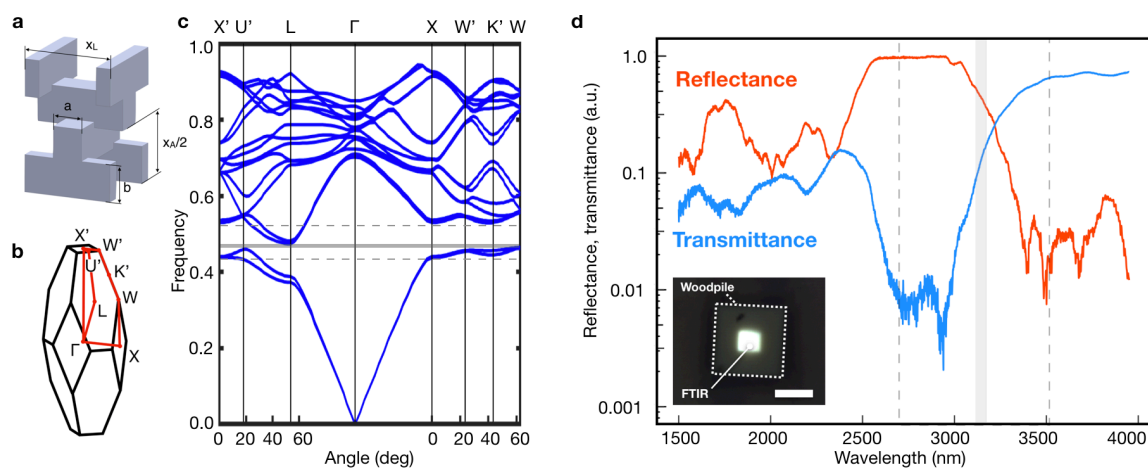


Figure 4.15. Optical characterization of 3D photonic crystals fabricated using the developed nanoscale AM process

**a** Schematic of a woodpile unit cell and **b** the corresponding Brillouin zone. **c** Calculated band structure of the fabricated woodpile FCT architecture. Grey band shows the position of a full photonic band gap. **d** FTIR reflectance and transmittance spectra taken from a woodpile structure showing the emergence of high reflectance and low transmittance bands centered at 2.9 µm.

Varying the $TiO_2$ precursor loading in the photopolymer enables control over the amount of post-pyrolysis linear shrinkage and of the structural feature sizes, which enables access to multiple wavelengths. We fabricated 3D photonic crystals with reduced lateral periods of 1.12, 1.03, and 0.84 μm by starting with the same pre-ceramic 3D sample and varying the TiO2 precursor loading by 50-83% (Figure 4.16). These structures were replicas of the titania woodpiles with $x_L$=1.47 μm shown in Figure 4.7b, d. Figure 4.16 shows FTIR reflectance spectra for these samples, as well as the computed bandgap positions, that revealed high reflectance bands centered at 1.8 um, 2.2 um, and 2.4 um, which are within 0.3%, 4.8%, and 3.0% of the target full photonic bandgap positions (Table 4.2).
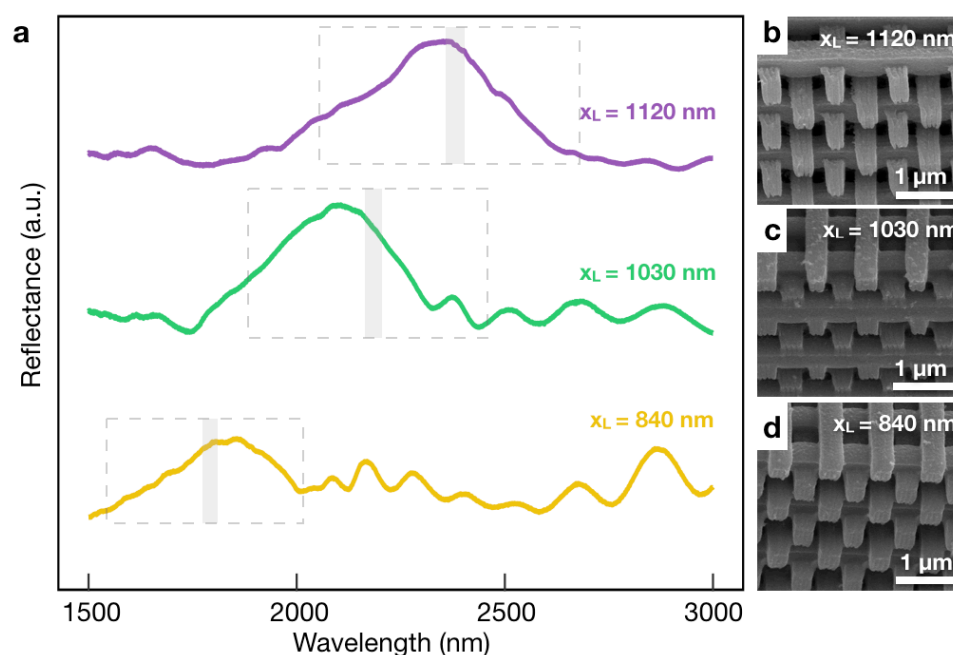


Figure 4.16. FTIR characterization of 3D woodpile architectures fabricated using a reduced precursor amount approach.

**a** FTIR reflectance spectra for as-fabricated woodpile structures with varying periodicities showing passive tuning of the reflectance band position between 1.8 and 2.4 μm. **b-d** SEM of representative woodpile structures with 1120 nm, 1030 nm, and 840 nm lateral periods fabricated using the developed AM method.

Table 4.2. Full and partial photonic bandgap edges (nm) for woodpile structures with lateral periods between 840 nm and 1470 nm

| Direction | Angle | Frequency | Woodpile lateral period, nm | | | |
|---|---|---|---|---|---|---|
| | | | 1470 | 1120 | 1030 | 840 |
| X'-U'-L | | 0.544 | 2700 | 2054 | 1883 | 1545 |
| | 16 | 0.457 | 3215 | 2445 | 2242 | 1839 |
| | | 0.492 | 2986 | 2271 | 2082 | 1708 |
| | 35.5 | 0.418 | 3521 | 2678 | 2455 | 2014 |
| X'-W'-K' | | 0.543 | 2708 | 2060 | 1888 | 1549 |
| | 16 | 0.451 | 3260 | 2479 | 2273 | 1865 |
| | | 0.530 | 2771 | 2108 | 1933 | 1586 |
| | 35.5 | 0.457 | 3217 | 2446 | 2243 | 1840 |
| Full bandgap | | 0.465 | 3161 | 2404 | 2204 | 1809 |
| | | 0.474 | 3101 | 2359 | 2162 | 1774 |

**Discussion**

We developed an AM process to produce three-dimensional networks of fully dense sub-micron features out of a transparent, high refractive index material that can be used to fabricate 3D dielectric photonic crystals. Compositional and microstructural analysis suggests that as-fabricated material is composed of fully dense nano-crystalline rutile $TiO_2$ with minimal carbon content. EDS revealed the chemical composition of 33.2 at% Ti and 66.8 at% O, which corresponds to a 1:2 atomic ratio of Ti to O characteristic of titanium dioxide. It is not possible to accurately determine C content using EDS because of its low sensitivity to light elements and because of inevitable carbon contamination in the SEM chamber [127]. Inclusion of the carbon peak in the EDS spectrum fit did not result in the fit improvement, which further corroborates extremely low at% C. Processes based on laser-driven formation of $TiO_2$/carbon composites yielded a substantial amount of carbon [82] that can lower the material transparency.

TEM electron diffraction and Raman spectroscopy identified $TiO_2$ to be in its rutile phase. Raman spectrum taken from a representative architected sample revealed peaks that are in good agreement with first-order vibration modes found in rutile titania [139] ($B_{1g}$ at 145 $cm^{-1}$, $E_g$ at 448 $cm^{-1}$, and $A_{1g}$ at 613 $cm^{-1}$), as well as with characteristic second-order scattering around 240 $cm^{-1}$ (see Figure 4.11f). This finding is also consistent with other works that studied phase transformation in sol-gel derived titanium dioxide [38,140]. For example, dry sol-gels of $TiO_2$ were found to convert from anatase into rutile at 550°C, with full transformation occurring at 800°C [140]. These studies suggest rutile as the predominant expected phase of titania resulting from a heat treatment at 900°C. Previous attempts to develop a titania AM process resulted in partially converted $TiO_2$ (e.g., rutile/anatase mix of 47 wt%/53 wt% in ref. [38]) and porous features with 10-16% air content [38,60], which lowered the effective refractive index of individual features.

FTIR reflectance and transmittance spectra of four woodpile samples (Figure 4.15d, Figure 4.16a) revealed that the observed high reflectance peaks were centered within 0.3% to 7% from the expected position of full photonic bandgaps predicted by PWE (Figure 4.15c). The observed deviations can be attributed to (i) the variability of geometric dimensions throughout the sample and (ii) the uncertainty of the refractive index measured by ellipsometry and used in PWE simulations. The SEM measurements and nested variance analysis showed ~1% in-plane (Table 4.1) and ~5% out-of-plane (Figure 4.9) deviations of the lateral period throughout the woodpile, and the measured refractive index of a $TiO_2$ film of 2.3 is 4-15% lower than the expected index of 2.40-2.71 for rutile $TiO_2$ within a 1500-3000 nm range [81]. This could be caused by some

inherent porosity in the $TiO_2$ film (Figure 4.13, left) used for ellipsometry measurements; the beams that comprise $TiO_2$ PhCs are fully dense. Uncertainty in the geometrical dimensions of up to 5% and in the refractive index of up to 15% can contribute to the observed deviations between experimental and simulated peak positions.

Table 4.3. Comparison between fabrication methods for 3D photonic crystals in the infrared and visible

| Reference | Process | Materials | Key aspects |
|---|---|---|---|
| [80] | Micromanipulation and stacking | GaAs | Manual stacking of individually fabricated 2D layers; high refractive index material (n~3.7 at 700 nm) |
| [60,76] | Single- and Double-inversion | Si, $TiO_2$ | TPL of a polymer template followed by a multi-step inversion procedure; complex 3D structures; up to 16% porosity |
| [39,40,42,141] | Two-photon lithography | Polymers, Silica with Zr, Zn, and Ge heteroatoms | Siloxane-based chemistry of the photoresist; low refractive index (n<1.6) |
| [59] | Direct Laser Writing of chalcogenide glasses | $As_2S_3$ | Direct writing using photo-induced metastability; challenging control of feature sizes; high refractive index material (n~2.5) |
| [58] | Direct Laser Writing of metal oxides | ZnO | Aqueous metal-containing resin; shrinkage up to 87%; refractive index n~1.9 |
| [38] | Direct Ink Writing | $TiO_2$ | Sol-gel ink; sub-micron features with 10% porosity; complex 3D structures; half of a lower-index anatase phase |
| [71] | Laser-induced insolubility | $TiO_2$ | Partial decomposition of a liquid precursor; poor adhesion to the substrate; loss of 3D structures |
| [82] | Laser-induced decomposition | carbon/$TiO_2$ | 2D patterning; presence of lossy carbon; 3 micron features for crystalline $TiO_2$ |
| This work | Nanoscale AM | $TiO_2$ | TPL of organic-inorganic material followed by calcination; complex 3D structures; <1% porosity; refractive index n>2.3 |

In summary, we developed an additive manufacturing process to create 3D nano-architected titania with a sub-micron resolution. We demonstrate the feasibility and efficiency of this process using a woodpile FCT architecture with individual feature widths of 150 nm as a model system. The as-fabricated material is carbon-free and consists homogeneous, fully dense nanoscrystalline rutile $TiO_2$. Taking advantage of the high refractive index and transparency of titania, we prototyped several PhCs with sub-micron lateral periods and full photonic bandgaps centered at 1.8-2.9 μm, consistently confirmed by PWE simulations and FTIR measurements. A comparison between the developed AM process method and other methods of PhC fabrication is shown in Table 4.3 and Figure 4.17.
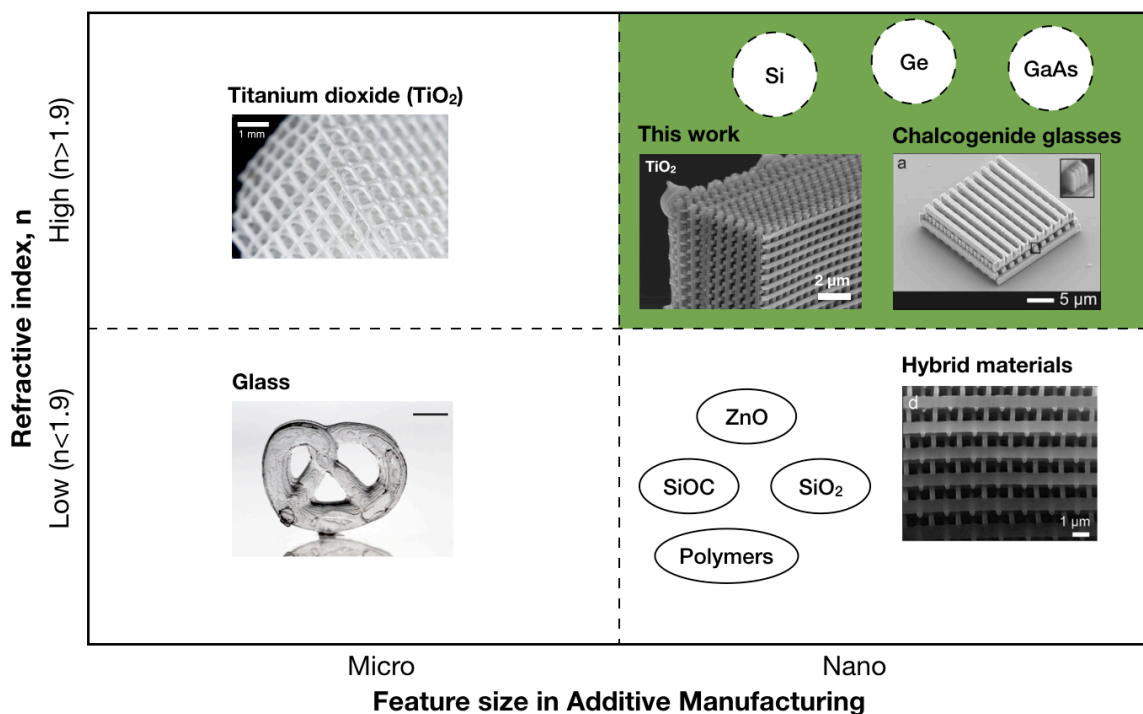


Figure 4.17. AM process landscape showing micro- and nanoscale AM processes of low- and high-refractive index materials

Fabricating PhCs with full photonic bandgaps in the visible requires lateral periods of ~300 nm [60], which can be achieved by extending the developed process to smaller feature sizes using the precursor loading approach demonstrated here. As a freeform fabrication method, this AM process is not limited to woodpile geometries and can be applied for direct fabrication of other 3D architectures. This nano-scale AM process is also not limited to $TiO_2$: other hybrid organic-inorganic-based photopolymers can be formulated to print a variety of materials, including other dielectrics, metals, and semiconductors. AM of 3D nano-architected titania is poised to enable facile fabrication of components for a much broader set of applications, including micro-optics, 3D MEMS, and minimally invasive tools and procedures.

# CHAPTER 5 : **MICROSCALE AM** OF METAL OXIDE CERAMICS: PHOTOCATALYTIC MATERIALS

**Chapter Summary**

This chapter presents an additive manufacturing (AM) process to create strong, self-supporting 3D photocatalytic titania architectures that enable feasible reactors for household solar water disinfection. Solar disinfection of drinking water (SODIS) is an approach for water purification widely used in households with limited access to fresh water. SODIS relies on microorganism deactivation triggered by sunlight energy in the UV spectrum and requires processing times of up to 48 hr. Water treatment rate is drastically increased by using photocatalytic materials, such as $TiO_2$, which can harvest sunlight to promote generation of reactive oxygen species (ROS) that inactivate bacteria within few hours. One main challenge that impedes the insertion of photocatalysts in most water treatment approaches is the need to populate the catalyst particles on a three-dimensional (3D) structure with a high-surface area that is stable under water flow.

We develop an additive manufacturing (AM) process for titania and propose an efficient design of a solar water disinfection device based on architected $TiO_2$ that does not require expensive filtering of the catalyst. We synthesize titanium monomers using a ligand exchange reaction between titanium alkoxide and acrylic acid and utilize these to prepare a pre-ceramic titania photoresist. We then use this photoresist in a commercial stereolithography apparatus to define complex 3D architectures, which are then pyrolyzed to

remove organic content. The resulting structure has ~40% reduced dimensions compared with its as-fabricated counterpart and has a chemical composition of 46 wt% Ti, 31 wt% O, and 23 wt% C, as measured at the surface by Energy-Dispersive Spectroscopy (EDS). Using this methodology, we fabricated 3D structures with periodic cubic and octet geometries whose unit cells range from 0.65 to 1.14 mm, beam lengths of 115-170 μm, and relative densities of 11-31%. Transmission Electron Microscopy (TEM) analysis reveals the microstructure of these lattices is nanoscrystalline titania (rutile) with a mean grain size of ~60 nm. Mechanical experiments reveal that these cubic titania microlattices, whose density is 350-365 kg/m$^3$, achieve compressive strengths of up to 4.3 MPa, which is several times stronger than what is reported for titania foams with comparable density.

We finally demonstrate how the developed AM process can be modified to reduce carbon content and produce >99 wt% titania parts. Photocatalytic characterization of as-fabricated 3D architected titanium dioxide shows that >99% of E.Coli can be deactivated and >97% of an organic contaminant (methynene blue) can be removed from water after 2 hours of simulated solar irradiation. Experiments to compare stochastic and deterministic architectures were conducted using superoxide radical generation, but quantification of the effect of 3D architecture was hindered by high variability in the radical generation data. High surface area, strong, self-supported architected photocatalytic structures have a potential to enable efficient solar water disinfection throughout the whole volume of the reactor without the need for expensive catalyst filtration.

**Concept of a household solar water disinfection device**

As discussed in Chapter 1, key aspects of household use of a photocatalytic reactor include the need for ultrafiltration of nanoparticles and the need for light access to the whole volume of the reactor. In the absence of ultrafiltration membranes and means of reactor agitation, a safe use of a photocatalytic reactor necessitates the use of catalysts with deterministic architectures (see Figure 1.11). A concept rendition of an architected titania device for household solar water disinfection is shown in Figure 5.1. A three-dimensional titania scaffold is placed inside of an optically transparent (e.g., PET) filled water bottle and placed in the sunlight (Figure 5.1a). The light interacts with the titania photocatalyst, which promotes the reaction with water and dissolved oxygen to produce hydroxyl ($^\bullet$OH) and superoxide radicals ($^\bullet$O$_2^-$) that deactivate bacteria (Figure 5.1b).
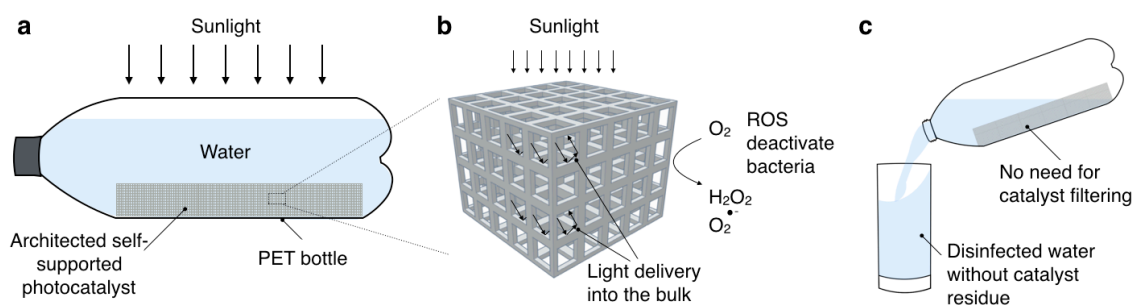


Figure 5.1. Concept of a household solar water disinfection device.

**a** Architected self-supported titania is placed inside an optically transparent bottle filled with water under the sunlight. **b** The photocatalyst promotes generation of ROS that deactivate microorganisms. The architecture allows for the light to be delivered into the bulk of the photocatalyst, supporting the disinfection throughout the whole volume of the reactor. **c** After disinfection is complete, the water can be consumed right away, without the need to filter out the catalyst.

The designed open-cell architecture of the scaffold allows the light to propagate throughout the bulk of the photocatalyst, which promotes the generation of ROS throughout the entire liquid volume and efficiently disinfects the water. High strength of the architected structure ensures that the catalytic material is not released to the treated water, so that it can be readily consumed after the disinfection (Figure 5.1c).

High efficiency of solar water treatment enabled by 3D architected photocatalyst will stem from

- water treatment throughout the whole volume of the reactor that is allowed by light delivery into the bulk of the architected photocatalyst (Figure 5.1b),

- efficient light harvesting that is allowed by multiple scattering (Figure 5.1b), and

- accelerated catalytic reactions due to hierarchical porosity of the catalyst: nano-scale pores in the beams provide high surface area, while meso-scale pores allow for facilitated mass transport.

This will effectively provide a high surface-area, strong, self-supported photocatalyst that will have a minimal risk of release in the environment or in the consumed water. Eliminating the need for expensive catalyst filtration and using abundant sunlight as the energy source can enable scalable and cost-effective household solar water disinfection.

**Process for stereolithography-based AM of titanium dioxide**

Acrylic acid (17.3 g) was slowly added to titanium(IV) ethoxide (13.7 g) in a glovebox (Fig. 2a), and the solution was manually agitated (Figure 5.2). The color of the solution changed from yellow to orange, which is indicative of a ligand exchange reaction [114]. This mix was then placed in a vacuum antechamber of the glovebox for 15 min to remove

excess ethanol. The resulting solution was taken out of the glovebox and mixed with 87.7

g of an open-source Autodesk PR48 formulation (39.776 wt% Allnex Ebecryl 8210,

39.776 wt% Sartomer SR 494, 0.4 wt% 2,4,6-Trimethylbenzoyl-diphenylphosphineoxide,

19.888 wt% Rahn Genomer 1122, 0.160 wt% 2,2'-(2,5-thiophenediyl)bis(5-

tertbutylbenzoxazole); Colorado Photopolymer Solutions) and stirred at room

temperature for 1 hr (Figure 5.2).
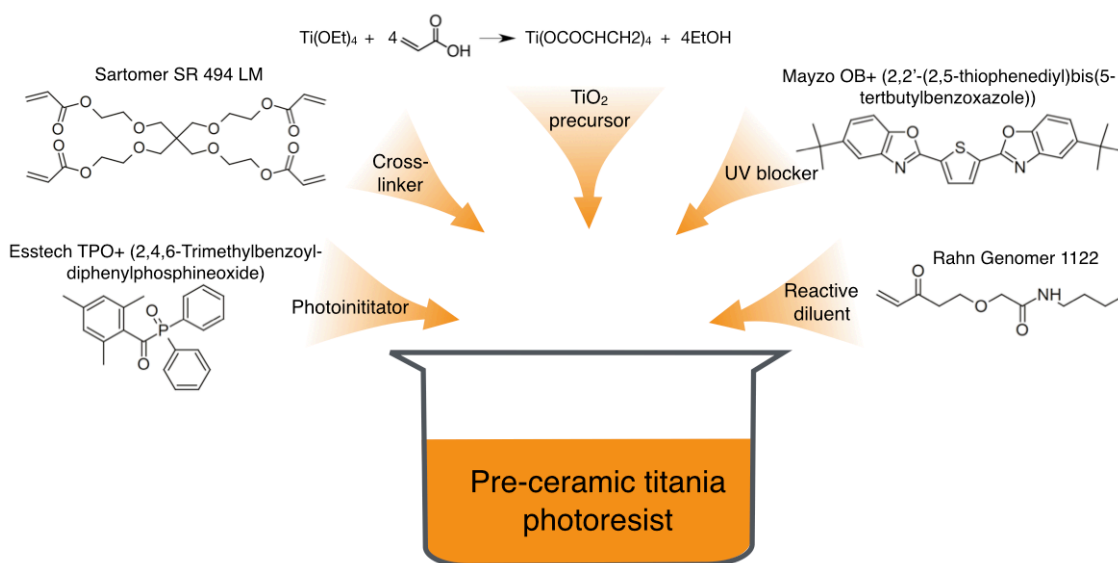


Figure 5.2. Pre-ceramic photopolymer formulation for SLA-based 3D
printing of titanium dioxide

We used a stereolithography-based 3D printer (Autodesk Ember) to pattern the

synthesized titanium-rich photoresist using a layer-by-layer approach with 25μm layer

thickness (Figure 5.3a). Structures with different geometries were printed, with the UV

exposure of the first layer for 14.0 s, four consequent layers for 9.0 s, and all remaining

layers for 3.5 s. Printed structures were developed in PGMEA for 15 min, followed by

IPA wash for 10 min. Figure 5.3b shows a representative titanium-containing polymer

scaffold after development.
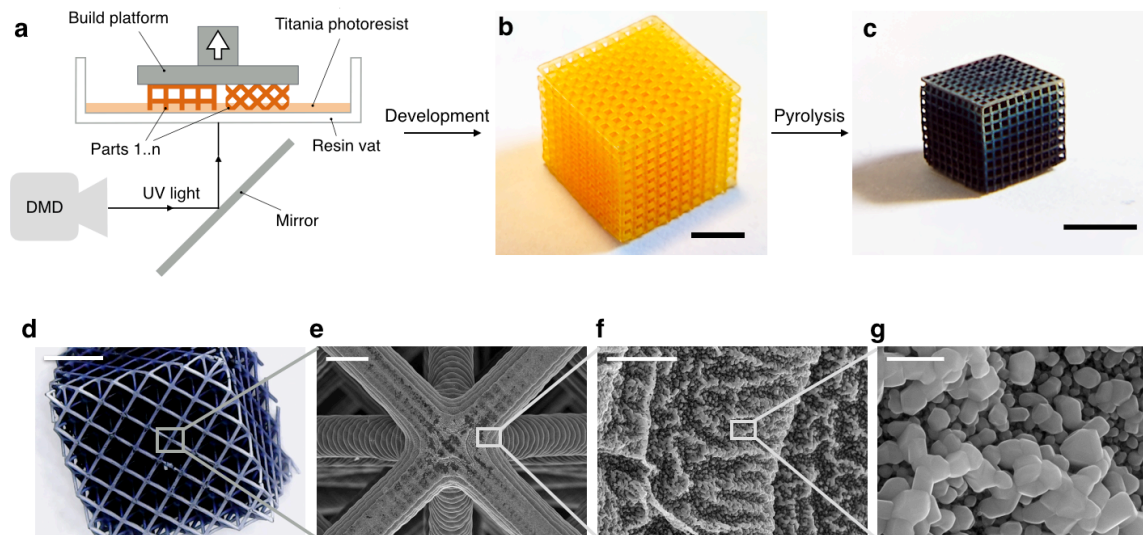
Figure 5.3. Process for AM of titania and SEM characterization of printed titania structures.

**a** Schematic of the SLA instrument to pattern titanium-containing photoresist into complex 3D geometries. Optical images of a cubic lattice made from titanium-containing polymer **b** before and **c** after pyrolysis. **d** Top view of a titania octet lattice (optical image). Colors in the optical image indicate the change of titania absorbance in the visible spectrum. SEM images of **e** a representative node in the unit cell of an octet lattice and **f, g** titania nano-crystallites on the surface of the structure. Scale bars are 5 mm for **b**, (d), 2 mm for **d**, 100 μm for **e**, 5 μm for **f**, and 500 nm for **g**

The final step in this AM process involved pyrolyzing the printed titanium-containing

polymer structures in a tube furnace using 4" quartz tube under 1 L/min argon flow. The

temperature was ramped up to 1000°C at 2°C/min, kept at 1000°C for 1 hour, and the

furnace was then cooled down to room temperature at a natural rate. Figure 5.3c, d show

representative titania structures after pyrolysis.

**Morphology, chemical composition, and microstructural characterization of**

**TiO$_2$/carbon composites**

We fabricated samples with two geometries: (1) 10x10x10-unit cell cubic lattices with unit

cell dimensions of 1.16 ± 0.10 mm and beam diameters of 393 ± 17 μm (Figure 5.3b) and

(2) 5x5x5-unit cell octet lattices with $1.71 \pm 0.17$ mm unit cell dimensions and $179 \pm 5$ μm beam diameters. These samples had relative densities that range from 11% to 31%. All samples were pyrolyzed in Ar atmosphere at 1000°C, which led to linear shrinkage of 39.0 $\pm$ 5.9% and a mass loss of 74.2 $\pm$ 2.5%. The final products were cubic titania lattices with unit cell sizes of $0.66 \pm 0.01$ mm and beam diameters of $170 \pm 5$ μm (Figure 5.3c) and octet lattices with unit cell sizes of $1.14 \pm 0.01$ mm and beam diameters of $115 \pm 4$ μm (Figure 5.3d). These 3-dimensional titania architectures appeared white, blue, black and other colors (Figure 5.3c, d), which likely stems from (i) a change in the visible light absorption of titania as a function of doping with carbon, sulfur and nitrogen, all of which are present in the initial photoresist, and (ii) a contribution to the the light absorption by the residual carbon.

Figure 5.3e-g show Scanning Electron Microscopy (SEM) (FEI Versa 3D DualBeam) images of the resulting morphology of the pyrolized titania octet lattices at different magnifications. These images reveal uniformly sized unit cells and beams with visible layer-to-layer transition patterns, which are inherent for the utilized SL printer (Figure 5.3e). The surface of the strucuture is covered by porous nanocrystalline formations with clearly visible facets and crystals ranging from 20 to 150 nm in size (Figure 5.3f, g).

SEM Energy-Dispersive X-Ray Spectroscopy (EDS) characterization was conducted with Zeiss 1550VP FESEM equipped with Oxford X-Max SDD using a 10 kV electron beam. Figure 5.4a, b, d, e shows EDS maps of the of the pyrolyzed titania lattices, which convey a uniform distribution of Ti, O and C throughout the structure. This EDS spectrum suggests a chemical composition of 46 wt% of Ti, 31 wt% of O, and 23 wt% of C (Figure 5.4c). Raman spectroscopy (Renishaw M1000 MicroRaman Spectrometer, 514.5 nm laser) conducted on

the surface of the pyrolyzed samples showed predominantly rutile signature (Figure 5.4f). Carbon content in the structure can be further reduced to <1 wt% by high-temperature oxidation in air (see 3D printing of carbon-free TiO2), leading to >99 wt% titanium and oxygen content. Further microstructural characterization and compression experiments were conducted using 3D printed titania samples with 23 wt% of C.
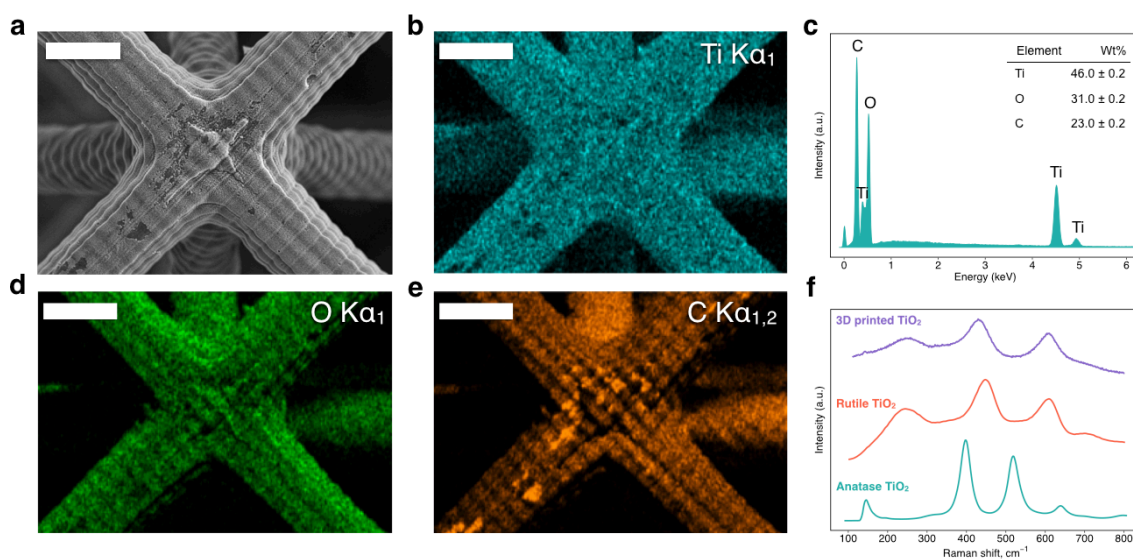


Figure 5.4. EDS and Raman characterization of printed titania structures.

**a** SEM image of an octet lattice node where EDS maps were taken. EDS maps of **b** titanium, **d** oxygen, and **e** carbon within the structure. **c** EDS spectrum taken from one of the beams shows mostly titanium and oxygen content by weight. **f** Raman spectrum of a 3D printed structure compared to reference spectra of anatase and rutile $TiO_2$ indicates mostly rutile phase of titania. Scale bars are 100 µm for **a**, **b**, **d**, and **e**

Figure 5.5 shows the results of microstructural analysis performed on a compressed titania lattice in a Transmission Electron Microscope (FEI Tecnai F30ST, 300 kV). The sampled titania particles, most likely, belong to the beam surface, since the crystal size considerably diminishes further away from the surface of the structure, as seen on an SEM image of a beam cross-section (Figure 5.5a). TEM images reveal the presence of $TiO_2$ crystals (Figure

5.5d) with a mean crystal size of 59.2 ± 8.0 nm (see Figure 5.5b for particle size histogram).

Electron diffraction pattern from a mostly crystalline region of the sample (Figure 5.5e)

corroborates rutile titania as the predominant phase (see Figure 5.5f). High-resolution TEM

image in Figure 5.5c demonstrates the presence of crystalline and amorphous regions within

the sample. FFT analysis of a crystalline region confirms the material to be rutile $TiO_2$, with

3.20Å lattice spacing that corresponds to (110) and ($\bar{1}$10) orientations (Figure 5.5c, top

right). Amorphous regions closer to the beam center correspond to $TiO_{1-x}C_x$, with oxygen

content varying as a function of depth, as seen on the EDS line spectrum of a beam cross-

section (see Figure 5.6).
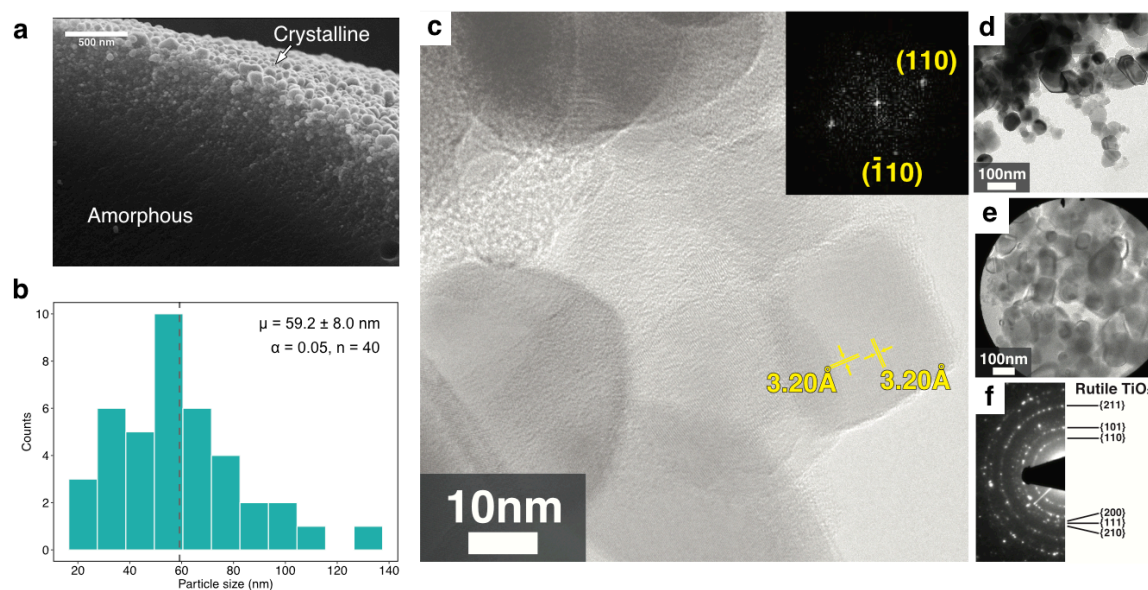


Figure 5.5. TEM and SEM characterization of printed titania structures.

**a** SEM image of a beam cross-section shows that the size of titania crystals gets smaller closer to the beam center. **b** Titania grain size histogram for n=40 particles measured from a TEM image showing 95% confidence intervals for the mean grain size ($\mu$) **c** HRTEM image showing titania particles. FFT analysis was used to determine the orientation and lattice spacings for one of the crystals. **d** Low-magnification TEM image of titania nanoparticles from the printed structure. **e** TEM image of the area where electron diffraction pattern was taken. **f** Electron diffraction pattern indicates mostly rutile titania
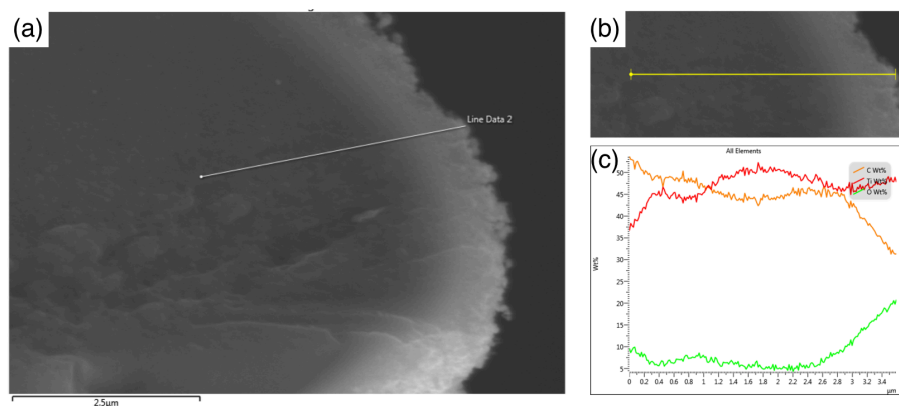
Figure 5.6. EDS characterization of a beam cross-section of a 3D printed titania octet lattice.

**a, b** SEM images of the beam cross-section where EDS line spectrum was taken. **c** Chemical composition within the beam along the line shown in **b** acquired by analysis of the line EDS spectrum.

**Compression of as-fabricated $TiO_2$/carbon microlattices**

Uniaxial compression tests on pyrolyzed cubic lattices were performed using Instron 5569 electromechanical testing machine equipped with an Instron 2525-802 load cell (R.C. 50 kN) at a displacement rate of 0.15-0.5 mm/min. The collected load vs. displacement data was converted into engineering stresses and strains using the height and the footprint of the structure measured from optical images before compression. Figure 5.7 shows optical images of the structure during compression (Figure 5.7a-d) and representative stress-strain data (Figure 5.7e). This data demonstrates that each compression began with a toe region corresponding to the sample settling into full contact followed by linear elastic regime up to 1-2% strain. Further compression resulted in gradual brittle failure of individual beams and unit cells (see Figure 5.7e and Supplementary Video 2).

The loading slope was used to calculate the structural elastic modulus to be 0.21-0.37 GPa. The strength was measured as the maximum stress achieved during initial elastic loading and

ranged from 2.1 to 4.3 MPa. These strengths and moduli are comparable to strongest reported titania foams with 2x higher densities, up to 2.5 MPa at 700 kg/m³ [142], and 2.1 to 5.6 times stronger than titania foams with comparable densities (0.8-1.0 MPa at 350 kg/m³) [142]. The mechanical properties of the architected titania lattices in this work may be further improved by using a high-temperature annealing step (≥1500°C) that would induce better sintering of titania particles.
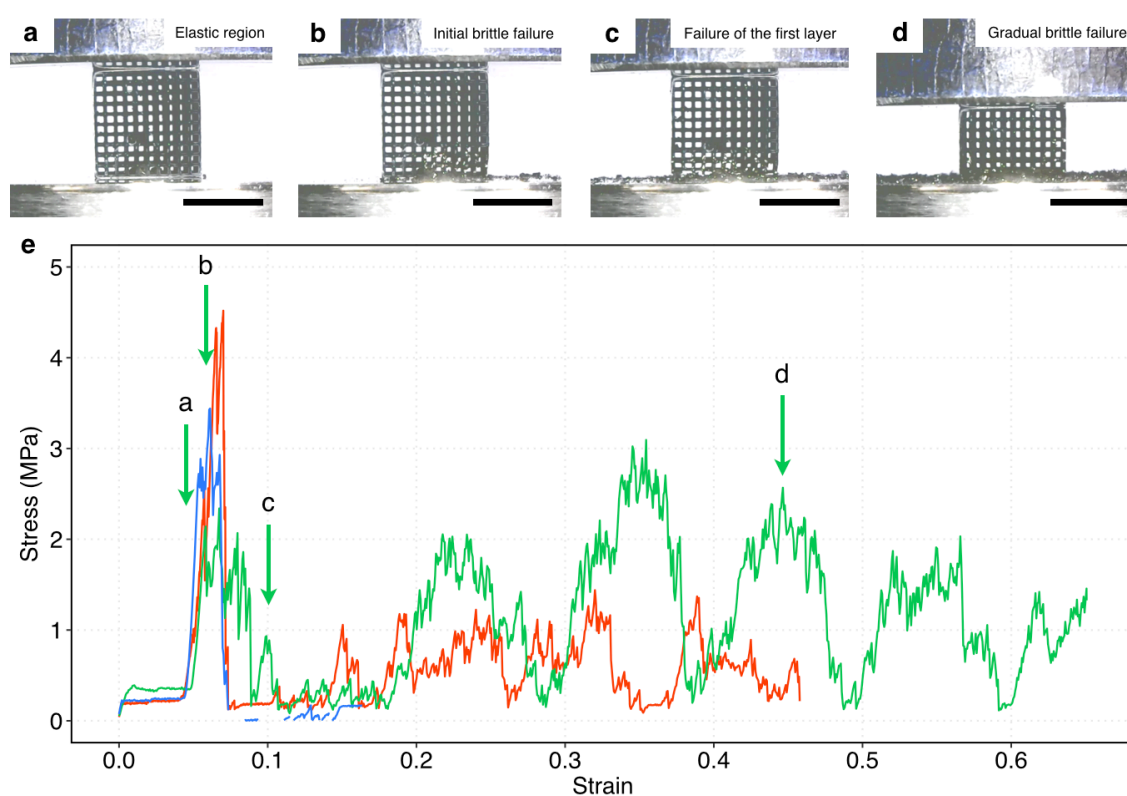


Figure 5.7. Uniaxial compression test of printed titania/carbon cubic lattices.

**a-d** Optical images of the structure during uniaxial compression showing different stages during the compression test: elastic region **a**, followed by brittle failure of the first layer **b, c** and gradual brittle failure of individual beams and layers **d**. **e** Stress-strain data for three cubic lattices. Scale bars for **a-d** are 5 mm.

**3D printing of carbon-free TiO$_2$**

Preparing carbon-free titanium dioxide 3D architectures required development of a pyrolysis schedule that allowed for full removal of carbon using calcination in air after initial volatilization of organic constituents and sample consolidation in inert gas. Titania cubic lattice structures with a cylindrical net shape shown in Figure 5.8 (17 unit cells in diameter, 10 unit cells in height, 0.6 mm unit cell size) were prepared using the 3D printing method described above followed by sample oxidation in air. The sample was placed in a tube furnace, and the temperature was ramped up to 1000°C at 5°C/min under 1 L/min argon flow. Argon flow was then turned off, allowing the air to slowly diffuse into the quartz tube at high temperature. The sample was kept at 1000°C for 6 hours and then cooled down to room temperature at a natural rate. Optical images shown in Figure 5.8a-c convey that the 3D printed lattice structures are uniformly white, which is characteristic of high titanium dioxide content. EDS spectrum taken from one of the beams (Figure 5.8d) suggests a chemical composition of 60.4 wt% of Ti, 39.0 wt% of O, and 0.5 wt% of P, which further corroborates predominantly titania content of the structure. Carbon-free TiO2 architectures provided a simple and well-studies material for investigation of the effect of architecture on photocatalytic performance.
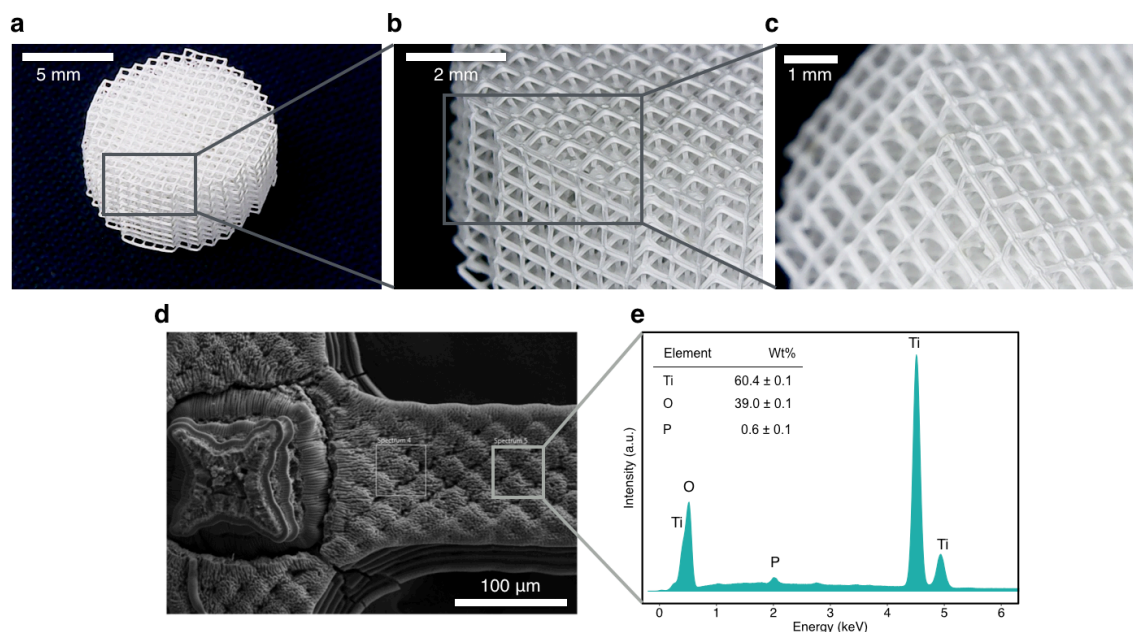
Figure 5.8. 3D printed titania cylinder comprised of simple cubic unit cells with unit cell dimensions of 600 μm and beam diameters of 150-200 μm.

**a - c** Optical images of 3D printed titania lattice that show uniform white color indicative of high titania and low carbon contents. **d** SEM image of a representative location on the lattice where **e** EDS spectrum was collected that reveals >99 wt% titania content.

## Photocatalytic activity of 3D architected titanium dioxide

Titania cubic lattice samples shown in Figure 5.8 were utilized for proof-of-concept tests of photocatalytic activity (with Priya K. Chittur, Kornfield lab). Gram negative bacterium *E. coli* was used for the antibacterial activity tests. Methylene blue (MB) solution in water (7.5 x $10^{-5}$ M) was used to test decomposition of organic contaminants. The bacteria were cultured with Luria-Bertani broth at 37 °C, and washed and suspended in 0.9% NaCl solution before use. Bacteria were then diluted to achieve $10^6$-$10^7$ CFU/mL initial concentration. Lattice samples were placed in a 24-well plate and 2 mL of bacterial suspension was added. The agitated suspension (rocker) was then subjected to solar irradiation (JCAP solar simulator)

for 2 hours. Samples were covered with aluminum foil for the dark experiments. The solution

was sampled every 30 min for 120 min; serial dilution was performed and the dilution was

then pipetted onto culture agar plates (2 replicates). The plates were kept at 37 °C for 16

hours and the formation of colonies was observed. Colonies were then counted using

OpenCFU. MB experiment started by one hour in the dark followed by two hours under

simulated solar irradiation. MB concentration was evaluated with UV-Vis spectroscopy

using absorbance values at 663 nm. The solution was sampled every 20 min.
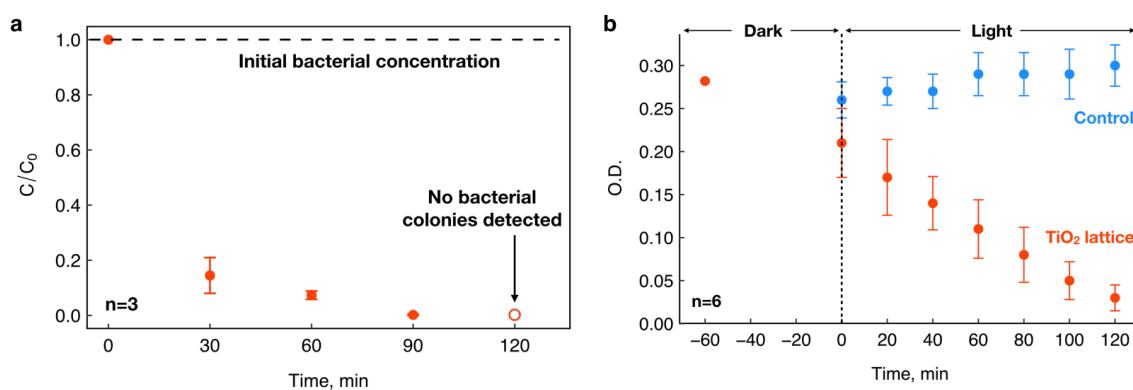


Figure 5.9. Proof-of-concept E. Coli and methylene blue (MB)
experiments to evaluate photocatalytic activity of 3D micro-architected
titanium dioxide.

**a** Normalized bacteria concentration in water with architected $TiO_2$ decreases by two orders of
magnitude after two hours of solar irradiation. **b** Methylene blue (MB) concentration drops by
97% compared to control after two hours of solar irradiation. Data courtesy Priya K. Chittur

Figure 5.9 shows the data for proof-of-concept photocatalytic experiments for 3D architected

titanium dioxide. Disinfection experiments (Figure 5.9a) showed at least a log2 reduction in

CFU values after 2 hours. Decomposition of MB using 3D architected $TiO_2$ (Figure 5.9b)

showed the removal of at least 97% of MB after 2 hours. These results suggest that as-

fabricated    3D microlattice architectures can be used for further photocatalytic characterization.

The idea of using meso-scale architectures to efficiently guide light in functional components has been explored for transparent electrodes in solar cells by Saive and Atwater (2018). Previous studies on the effect of architecture on light delivery through metal grid contacts showed that it is possible to design 2D grids that let >99% of solar energy through while maintaining ~5% of areal coverage by highly reflective metallic structures [143]. This was achieved by changing the beam cross-section in the grid from rectangular to triangular, which helped to guide the light through the contact grid not only through the openings in the grid, but also for the portion of light that was reflected and scattered by triangular beams preferentially into the solar cell.

We adopted the idea of using meso-scale architecture for guiding light by choosing two deterministic architectures that are natural extensions of 2D grids explored by Saive and Atwater: a woodpile FCT architecture with rectangular beams (see Figure 5.10a, c) and a woodpile FCT architecture with triangular beams, or effectively translucent architecture (see Figure 5.10b, d). Each layer of these architectures is essentially a 2D grid that interacts with light before it gets to the next 2D grid layer, with the main difference being the beam cross-section; samples with rectangular beams are expected to screen more light due to  reflections back from the top surface of the rectangular beams.
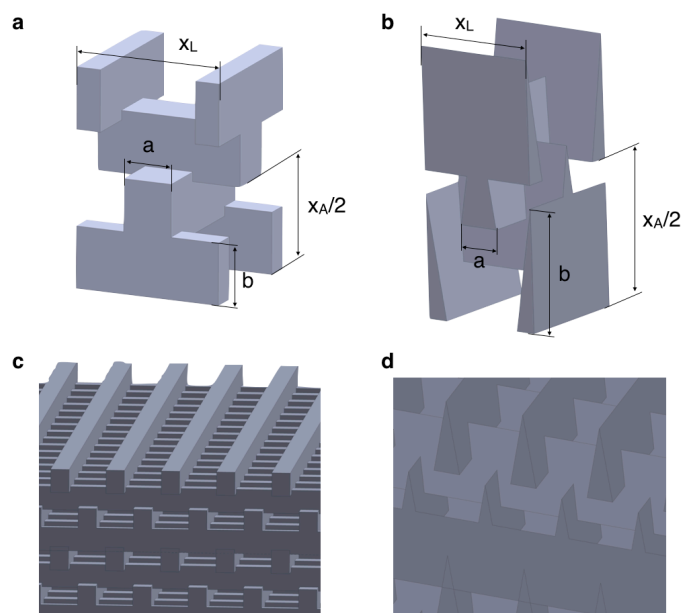
Figure 5.10. Deterministic 3D architectures considered for photocatalytic experiments

**a** Unit cell of **c** a woodpile FCT architecture. **b** Unit cell of **d** an effectively translucent (ET) architecture

To quantify the effect of architecture on photocatalytic performance, we compared these two deterministic structures with a stochastic one, spinodal, that served as a baseline (see Figure 5.11). To isolate the effect of 3D architecture, we designed the deterministic architectures to have (1) equal surface areas and (2) equal pore sizes to the stochastic one. This allowed to keep the mass transport and the number of reaction sites similar between the three geometries while controlling the light transport using architecture.

For a woodpile unit cell (Figure 5.10a) with lateral period $x_L$, axial period $x_A$, and rectangular beams of width $a$ and height $b$, we can calculate relative density $\rho$ as the ratio between the volume of the material in the unit cell and the volume of the unit cell as

$$\rho = \frac{4abx_L - 4a^2(b - b - \frac{x_A}{4})}{x_A x_L{}^2} \tag{5.1}$$

We can also calculate the surface-to-volume ratio $\psi$ as the ratio between the area of the exposed surface and the volume of the unit cell as

$$\psi = \frac{8(a + b)x_L - 8a(2a\left(b - \frac{x_A}{4}\right) + a)}{x_A x_L{}^2} \tag{5.2}$$

Similarly, for the ET architecture (Figure 5.10b) with lateral period $x_L$, axial period $x_A$, and triangular beams of width $a$ and height $b$, we can calculate relative density $\rho$ as

$$\rho = \frac{2(abx_L - \frac{a^2(b - \frac{x_A}{4})^2}{b})}{x_A x_L{}^2} \tag{5.3}$$

and surface-to-volume ratio $\psi$ as

$$\psi = \frac{4(-2a\sqrt{\frac{a^2}{4b^2} + 1}\left(b - \frac{x_A}{4}\right) - \frac{a^2(b - \frac{x_A}{4})}{b} + \left(2\sqrt{\frac{a^2}{4} + b^2} + a\right)x_L - \frac{a(b - \frac{x_A}{4})^2}{b})}{x_A x_L{}^2} \tag{5.4}$$

For different architectures with the same net dimensions, equal catalyst loading would then correspond to having the same $\rho$, and having the same surface area – to having equal $\psi$. For pre-pyrolysis woodpile and ET structures we can set the same lateral periods $x_L = 1.2\ mm$, pore sizes $x_L - a = 0.8\ mm$, and surface area-to-volume ratios $\psi = 2.97\ mm^{-1}$. Using Equations (5.2) and (5.4) we can calculate $a = 0.4\ mm$, $b = 0.51\ mm$ for the FCC woodpile and a$= 0.4\ mm$, $b = 1.2\ mm$, and $x_A = 2.6\ mm$ for the ET architecture.

Assuming isotropic shrinkage during pyrolysis, we can reasonably expect the pore sizes and the surface areas of as-designed architectures to remain equal to each other after ~60% linear shrinkage. Figure 5.11a-c shows the resulting designs. Optical images of as-fabricated titanium dioxide 3D architectures are shown in Figure 5.11d-f.
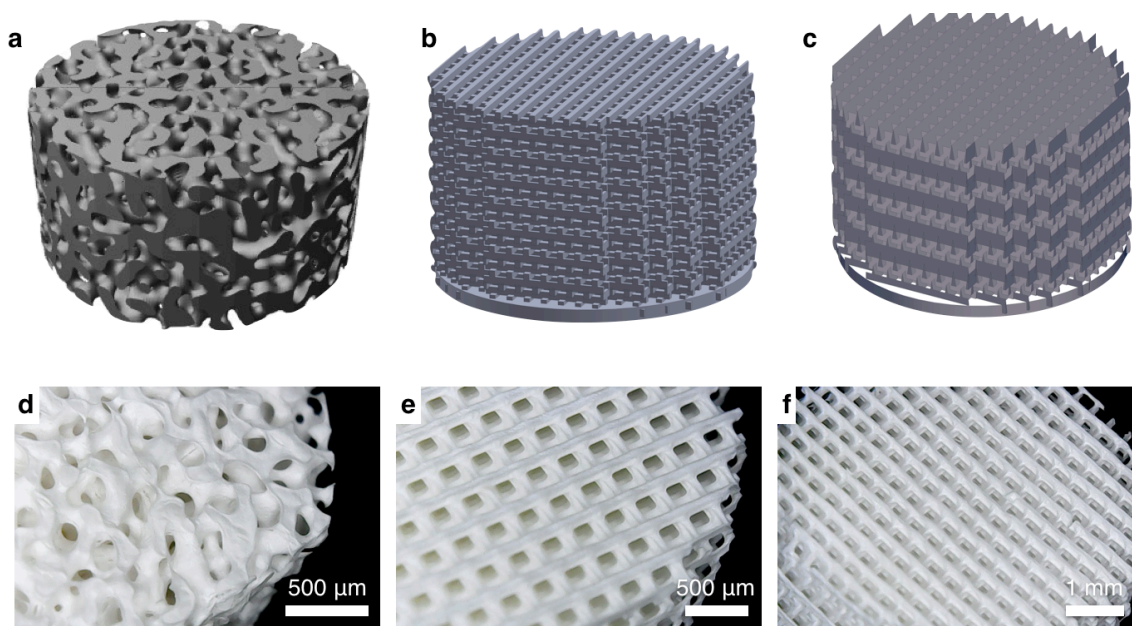


Figure 5.11. Stochastic and deterministic architectures fabricated for photocatalytic experiments

**a** Spinodal (S), **b** Woodpile (W), and **c** Effectively Translucent (ET) architectures designed for photocatalytic experiments. **d-f** Corresponding optical images of as-fabricated titanium dioxide lattices

To determine the effect of architecture, we analyzed the variability of XTT formazan generation rate using analysis of variance (ANOVA). Figure 5.12 shows experimental setup for ANOVA using a design with three architectures, namely spinodal (S), woodpile (W), and effectively translucent (ET), three lattice heights, and two replicates each. The height of Medium (M) samples was twice the height of the Small (S) ones, and Large (L) samples had three times the height The underlying model for the observed change in

absorbance took into account the effect of architecture, the effect if sample height, and the error.
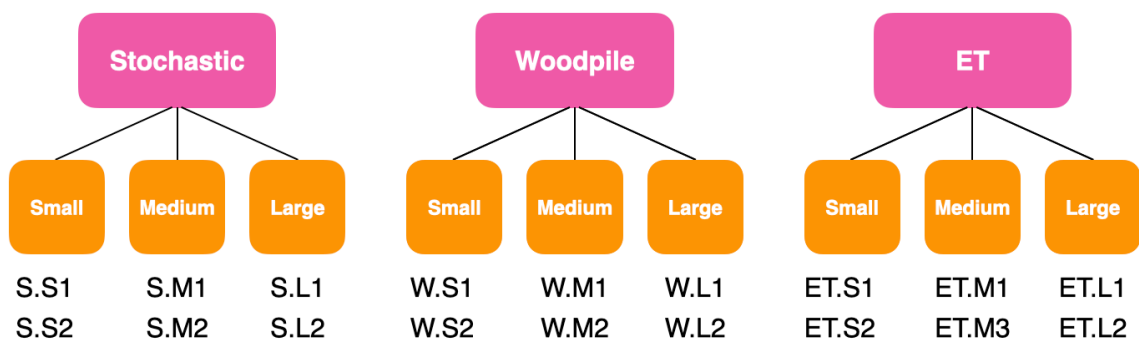


Figure 5.12. Experimental design for an ANOVA study of the effect of architecture and lattice height on photocatalytic performance of 3D architected titanium dioxide

Sample labels used throughout this study (usually preceded by Ti5) are shown below.

Figure 5.13 shows experimental setup for photocatalytic experiments. Decomposition of XTT sodium salt into XTT formazan was used to selectively quantify superoxide radical generation [144]. Quartz cuvette was filled by 2 mL of aqueous solution of XTT and a $TiO_2$ lattice sample was placed in contact with the cuvette wall (Figure 5.13a). A pen-ray UV lamp (254 nm) was placed at 10 mm distance from the quartz cuvette (Figure 5.13b). UV-Vis spectroscopy was used to measure the absorbance at 470 nm every 5 min for 20 min, which was used to quantify XTT formazan concentration. A control XTT solution without photocatalyst, or 'blank', was also exposed to UV and served as a control (Figure 5.13c)
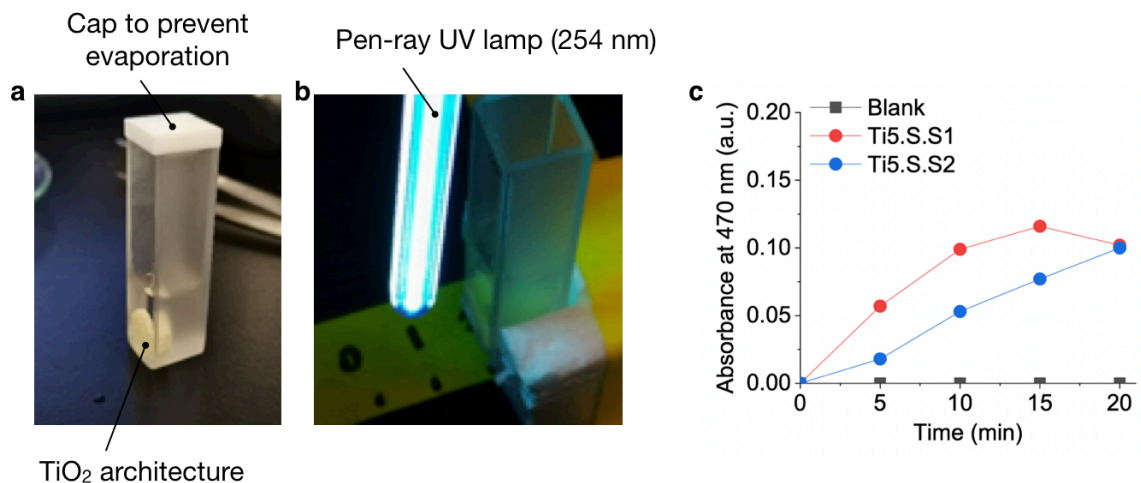
Figure 5.13. Experimental setup for photocatalytic characterization of 3D architected titanium dioxide

**a, b** Quartz cuvette with an aqueous solution of XTT and titanium dioxide architecture was subjected to UV light (254 nm). **c** Representative absorbance versus time data for superoxide-driven decomposition of XTT of two replicates. Photos and data courtesy of Dr. Kai Liu, Caltech.

Following the experimental design shown in Figure 5.12, we have tested samples with three architectures, three sample heights, and two replicates each; a total of eighteen samples was tested. Representative XTT formazan generation data for the three architectures and small (S), medium (M), and large (L) sample heights is shown in Figure 5.14. All absorbance curves started with a linear region (up to 5-10 min, depending on the sample) followed by non-linear region with a decreasing rate of XTT formazan concentration change, leading, in some cases, to almost full disappearance of XTT formazan (e.g., see Figure 5.14c). This likely stems from further XTT formazan decomposition by hydroxyl radicals formed directly by UV light in water and photocatalytically on the surface of titanium dioxide architectures. The slope of the linear portion of the absorbance vs time curve was used to calculate the apparent rate of XTT formazan formation. This rate was used for comparison between different architectures and sample heights using ANOVA structure shown in Figure 5.12.
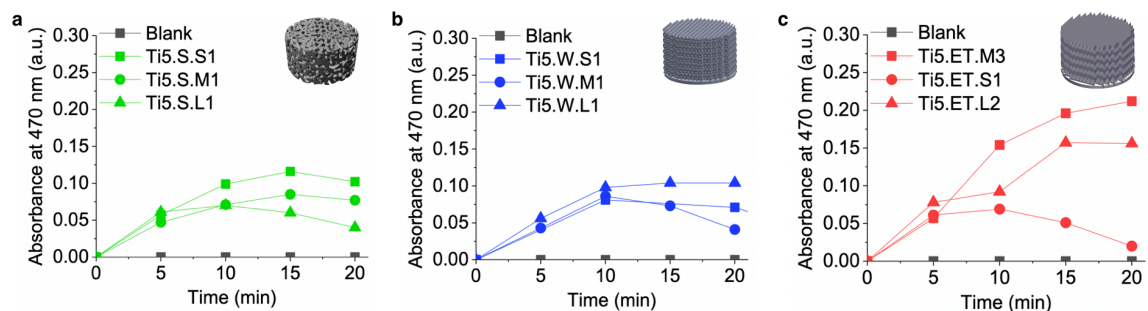
Figure 5.14. Representative data for photocatalytic superoxide-driven decomposition of XTT for stochastic and deterministic titanium dioxide architectures

Data shown for **a** Spinodal (S), **b** Woodpile (W), and **c** Effectively Translucent (ET) architectures of small (S), medium (M), and large (L) sample heights

The results of ANOVA are shown in Table 5.1. We can see that the effect of the architecture (p~0.71) and the effect of sample height (p~0.18) cannot be discerned in a statistically significant way. This means that that based on the eighteen samples tested the variability in photocatalytic performance can be fully explained by error. The implications of this result are explored in Discussion and Future Work.

Table 5.1. ANOVA results for the effect of architecture and the sample size on photocatalytic performance of 3D architected titanium dioxide

| Source of variation | Sum of squares | Degrees of freedom | Mean square error, MSE | F0 | p-value |
|---|---|---|---|---|---|
| Architecture | 1433.44 | 2 | 716.72 | 0.36 | 0.713 |
| Size | 11984.33 | 6 | 1997.39 | 1.94 | 0.178 |
| Error | 9254.50 | 9 | 1028.28 | | |
| Total | 22672.28 | 17 | | | |

**Discussion and Future Work**

In summary, we synthesized transparent titanium-rich photoresist and demonstrated a process for AM of polymer-derived titania by fabricating octet and cubic lattice structures with 115-170 μm beams, 0.65-1.50 mm unit cells, and 11-31% relative densities. We showed that the microstructure of these lattices is nanocrystalline rutile titanium dioxide with 60 nm

mean grain size. We demonstrated titania contents in the resulting structure between 77 wt% and >99 wt% depending on the pyrolysis conditions. We found that the strengths of 3D printed titania lattices is several times higher than that of titania foams with comparable relative densities.

Proof-of-concept photocatalytic experiments revealed that 3D architected titanium dioxide deactivated >99% E. Coli and removed >97% of methylene blue within 2 hours of simulated solar irradiation. Further quantification of superoxide radical generation by the photocatalysts was conducted using stochastic and deterministic architectures with the same surface area and the same pore size. ANOVA showed no statistical significance of the effect of architecture nor of the effect of catalyst loading. The effect of the sample height, or the photocatalyst loading, is expected to be significant for twice and thrice the amount of titanium dioxide in medium and large samples, correspondingly, when compared to small samples. This suggests that the high variability of the acquired data masked the effects of both the architecture and the loading, and a more precise protocol to quantify radical generation needs to be adopted.

Using AM of titania to produce 3D structures with high strength and architected porosity is also of interest for photocatalytic water splitting for hydrogen production [145], fuel generation from $CO_2$ [146], solar cells [147], and scaffolds for tissue engineering [142].

# CHAPTER 6 : SUMMARY AND OUTLOOK

**Summary**

The objective of this thesis was to develop micro- and nanoscale metal and ceramic AM processes that can efficiently manipulate three types of materials: (1) metals, (2) transparent, high refractive index materials, and (3) photocatalysts (see Significance of micro- and nanoscale AM). We started by developing the AM Process Framework that included three main components: material feedstock, energy source, and shape definition. We analyzed established AM processes using this framework and showed that the choice of material feedstock limits the minimal feature dimensions achievable by the process. We further discussed state-of-the-art nanoscale metal and ceramic AM processes and showed how alternative metal feedstocks allowed for fabrication of sub-micron features out of several inorganic materials.

Following this, we demonstrated an AM process for fabrication of 3D nano-architected nickel. First, we synthesized nickel-containing hybrid organic-inorganic materials and used them to formulate photopolymers that are amenable to two-photon lithography (TPL). We then employed TPL to create the desired 3D architectures. We pyrolyzed the samples to remove organic constituents and to reduce and consolidate the remaining nickel. This resulted in smaller replicas of these 3D architectures that consisted of nanocrystalline, nanoporous nickel with ~300 nm feature dimensions. *In situ* nanomechanical testing of as-fabricated 3D nickel octet lattices revealed that the specific structural strength of these architectures is comparable to that of beam-based lattice structures made by established AM

processes with two orders of magnitude larger feature dimensions (see Figure 3.4). We further showed that the throughput of this process is at least an order of magnitude higher than that of other nanoscale metal AM techniques (see Figure 2.5 for comparison).

We further explored how the developed nanoscale AM process can be extended to incorporating other metals and metalloids (see Figure 2.6) and ultimately printing other inorganic materials. We have demonstrated AM of 3D nano-architected titanium dioxide ($TiO_2$), a transparent, high-refractive index ceramic that can be used to create 3D dielectric photonic crystals in the visible and the infrared. We formulated a hybrid photopolymer rich in titanium, sculpted it using TPL, and used calcination in air to convert the green part to a ceramic architecture that consisted out of fully dense nanocrystalline rutile titanium dioxide with feature dimensions down to 120 nm. We systematically studied and modeled the relationship between the process parameters and feature dimensions, and then used this model to achieve precise dimensional control required for fabrication of photonic crystals. As a result, we were able to fabricate 3D photonic crystals with a full photonic bandgap in the infrared, which was confirmed by optical characterization of as-fabricated structures and by modeling their band structure. Nanoscale AM of fully dense $TiO_2$ has significant impact on enabling rapid prototyping of micro-optics and 3D dielectric PhCs.

Finally, we developed a microscale AM process for titanium dioxide and used it to study the effect of meso-scale architecture on performance of 3D architected photocatalysts. We synthesized a titanium-based hybrid organic-inorganic material using the approach developed in Chapter 4 and formulated a liquid photopolymer amenable to stereolithography (SLA). SLA-printed 3D architectures were pyrolyzed in inert atmosphere followed by

calcination in air at temperatures up to 1300°C, which yielded $TiO_2$ structures with feature sizes down to 115 μm and relative densities down to 11%. We showed that these 3D photocatalytic microlattice architectures can remove >99% of *E. Coli* and >97% of an organic contaminant (methylene blue) after 2 hours under simulated solar irradiation. Our further quantification of the effect of 3D architecture on the photocatalytic performance has, so far, not been elucidating. The experimental data from superoxide radical generation contains too much variation, potentially masking any statistically significant effects of architecture and material loading.

All three processes developed in this work, including nanoscale AM of nickel and nano- and microscale AM of titanium dioxide, used the same key concept of selectively cross-linking hybrid organic-inorganic materials. Synthesizing and utilizing these hybrid materials as material feedstock is the key factor that ultimately allows to achieve sub-micron resolution by controlling few atom-sized metal oxo-clusters (see Figure 1.5 for the role of material feedstock). We examine how the AM processes developed in this work fit into the AM framework introduced in Chapter 1 (Figure 6.1).

All three processes developed in this work used locally delivered light as the energy source. For the TPL-based nanoscale AM processes the light source was a pulsed fs infrared laser, while for the SLA-based microscale AM of titanium dioxide — a UV light source. In all cases, shape definition was achieved by moving or shaping the energy source, i.e. by scanning the focused laser within the photopolymer using a galvo mirror system (TPL-based processes) or by shaping the light using Digital Light Processing (DLP). The choice of light as the energy source and scanning the energy source for shape definition is what ultimately

allowed for an order of magnitude faster throughput than for other nanoscale metal AM techniques (Figure 2.5).
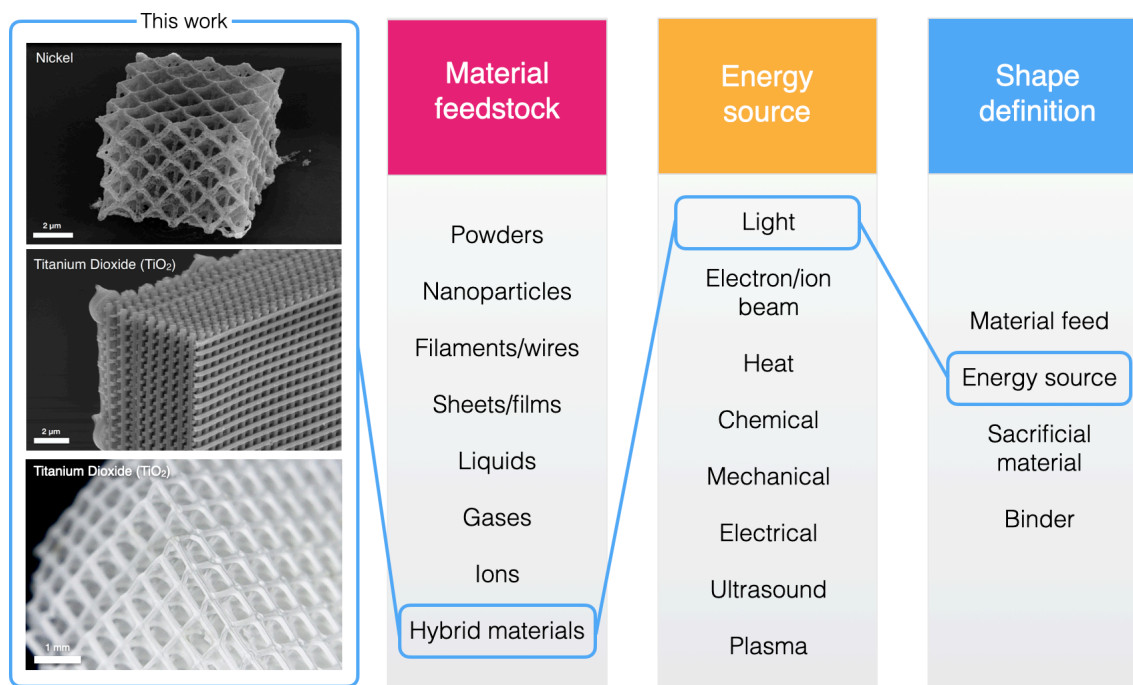


Figure 6.1. Nanoscale and microscale AM processes developed in this work and how they fit into the AM process framework

Next, we discuss the limitations of the AM processes developed in this work and some open questions. We also discuss how further examination of this AM framework can help identify new opportunities in development of new AM processes, increasing the throughput of existing AM, and new material development for AM.

**Open questions**

In this work we focused on developing new micro- and nanoscale AM processes for metals and ceramics, investigating microstructure and chemical composition of as-fabricated materials, and characterizing mechanical, optical, and photocatalytic properties of the printed

structures. Other key aspects that remained out of scope of this work include process limitations of the developed AM techniques, investigation of exceptional mechanical strength of flawed nickel nanolattices, and further characterization of the effect of architecture on the performance of photocatalytic materials. These are briefly discussed below.

*Process limitations*

There are several limitations of the developed AM processes that have not been investigated in detail in this work, namely (1) control of material quality, (2) further reduction in minimal feature dimensions, and (3) extending the processes to other materials.

Depending on the application, material quality requirements can include material density, surface roughness, optical quality, etc. Structural strength of nickel nanolattices from Chapter 3 is a function of nickel grain size, surface roughness, beam porosity, and material inclusions, such as nickel oxide and nickel carbide (see Structural strength of 3D nanocrystalline, nanoporous nickel for a more detailed discussion). Optical response of 3D dielectric PhCs from Chapter 4 depends on surface roughness of the individual beams and optical properties of the constituent material, i.e. refractive index and loss coefficient, which are, in turn, determined by phase composition, grain size distribution, and porosity. These aspects of material microstructure and the presence of defects are a function of the pyrolysis conditions. Thermal and chemical profiles during hybrid material conversion to metals and ceramics need to be carefully considered to control the microstructure and the defects in as-fabricated structures.

An important factor that contributed to the minimum feature sizes attainable by the developed AM processes is the shrinkage that reduced linear dimensions of as-printed features by 57-80%. As the result, we were able to fabricate 3D architectures with features down to ~120 nm and 2D grids and wires with ~25 nm widths. It remains unclear whether additional material removal can be utilized to shrink the feature dimensions beyond that. Several factors that are important during pyrolysis, including premature volatilization of organic constituents and loss of percolating network of solid material, grain coarsening, and non-isotropic shrinkage, can lead to the loss of a 3D architecture. Stability of 3D architectures after ~90% reduction in linear dimensions has been demonstrated [58], but the resolution limit as a function of shrinkage remains to be investigated.

Another important aspect of the developed process is whether it can be used for other materials other than Ni, carbon, and $TiO_2$. Based on the choice of material feedstock, namely hybrid organic-inorganic materials, we expect that this process could be extended to transition d metals, with notable examples including V, Mn, Cr, W, Cu, and Zn; to metalloids, such as Si and Ge; and to corresponding oxides, nitrides, and sulfides (see Figure 2.6 for some examples demonstrated in this work). Similar to the approach demonstrated in Chapter 4, oxides can be potentially prepared by calcination of the target metal-containing hybrid in air. 3D nitrides can be fabricated by converting metals and oxides during pyrolysis; for example, TiN and GaN can be printed by nitridation of titanium dioxide or gallium oxide using $NH_3$. Finally, sulfides can be fabricated by incorporating sulfur atoms into the photopolymer using thiol-based chemistry. However, the success of printing a particular material will depend on the stability of the corresponding hybrid organic-inorganic materials

and the ability to convert them to the target material. We discuss this further in AM of New Materials section of this chapter.

*Structural strength of 3D nanocrystalline, nanoporous nickel*

Despite the detrimental microstructure that comprises nickel nanolattices in Chapter 3, their specific strength was 2-7x higher than that of stainless steel beam-based architectures with three orders of magnitude thicker beams. The microstructure of as-fabricated nickel structures is nanocrystalline and nanoporous and has different levels of pore hierarchy. Each individual beam is nanocrystalline and contains stochastic nanopores, and the entire structure contains deterministic nanopores. This microstructure within the individual beams stems from sintering of the Ni nanoparticles after the organic components volatilize; it is in distinct contrast to the monolithic metallic beams in all other works on the deformation of nanoporous materials discussed in Chapter 3. This leads to detrimental effects on the structural strength of these architectures.

This microstructure is detrimental to the overall structural strength in two ways: (1) the additional porosity within the beams lowers the overall relative density of the architecture and (2) upon mechanical deformation, each sintered junction experiences a localized stress, which creates a stress concentration in the material at an adjacent pore. The pores that border these regions of local stress concentrations can be viewed as "notches" or "flaws" that serve as locations of failure initiation upon mechanical loads. The distribution of nano-pores in each beam that comprises the nanolattices in this work leads to a distribution in the local failure strengths, which — in combination with the detrimental effects of lower relative density and the presence of junctions — serves to lower the overall structural strength.

Some of the existing literature on the deformation of nano-porous metallic foams [129] and individual metallic nano-pillars [10,148], report higher strengths upon uniaxial compression than ones reported in this work. The key difference between the strength reported in this work and those in previous reports is that it is representative of the structural strength of the nanolattice, where each beam has heterogeneous porous microstructure, as well as each nodal junction, and both are subjected to a complex stress state upon global compression. These foams have a fundamentally different microstructure compared to the nanolattices in this work; they are stochastic and have single-crystalline pristine ligaments, which makes a direct comparison challenging. The relationship between microstructure and strength of as-fabricated nanoporous, nanocrystalline nickel remains to be investigated.

*Effect of 3D architecture on photocatalytic performance*

The goal of developing a micro-scale AM process for $TiO_2$ was to investigate the effect of 3D architecture on the efficiency of photocatalytic water treatment. While proof-of-concept experiments showed photocatalytic activity of 3D architected titanium dioxide, a more rigorously designed study that compared a stochastic design with two deterministic ones did not reveal a significant difference in superoxide radical generation between the structures. This likely stems from the variation in the observed photocatalytic data masking the differences between architectures, which was suggested by an ANOVA study with different lattice heights, or catalyst loadings. A more repeatable characterization approach could reduce the variation in photocatalytic performance and allow to observe statistically significant differences between the structures. Establishing a reliable testing protocol for 3D architected structures would allow to experimentally quantify the effect of architecture and to begin designing 3D photocatalysts with a maximized radical generation rate and a

minimized volume of 'sun shelters' that could harbor pathogens. This could be achieved by topological optimization based on ray tracing combined with reasonable estimates of quantum efficiency of the light-driven radical generation process. Next steps require further experimental and numerical investigation of the effect of 3D architecture on photocatalytic efficiency.

**Future work**

We have already examined how the processes developed in this work fit into the AM framework introduced in Chapter 1 (see Figure 6.1). We further discuss how this framework can assist in increasing AM throughput, in adopting new materials for AM, and for developing novel AM processes.

*Increasing Throughput of AM*

One of the key aspects of using an AM process for a particular application is the process throughput. To compare between AM processes at the same scale, one can use volumetric throughput (see Figure 1.2). We have discussed in Chapter 2 that comparison between AM processes that operate at different scales is more useful in terms of voxels $s^{-1}$ (see Figure 2.5), which indicates the rate of shape definition at the relative scale of the AM process. For example, moving a robotic arm with a wire feeder and a plasma arc in RPD is slow and limits the throughput to just a few voxels per second. We can compare this to the throughput of beam-based techniques, such as EBM and DMLS, where electron and laser beams can be scanned at thousands of voxels per second (see Figure 2.5). This comparison reveals that at multiple scales the process throughput is the function of the rate of the underlying shape definition step.

The shape definition time is often limited by the rate of the underlying physical process in the AM technique. This rate can be increased significantly by switching to an alternative shape definition approach. For example, meniscus-confined electroplating is a very slow process (0.04-1.0 voxels s$^{-1}$) limited by the rate of stable electroplating. In the AM framework (Figure 1.3), this process represents a combination of Metal Ions, Electrical Energy, and Material Feed. In contrast, EFAB (Metal Ions + Electrical Energy + Sacrificial Material) relies on the same physical process, i.e. electroplating, but uses lithographically fabricated patterns to define the geometry of individual layers. This allows to increase the throughput of this AM process to >10000 voxels s$^{-1}$ (see Figure 2.5).

The shape definition time can also significantly reduced by adopting parallelization rather than changing the shape definition mechanism. For example, state-of-the-art binder jet processes, such as Digital Part Materialization and Digital Metals, utilize hundreds of nozzles depositing binder material at >$10^5$ voxels s$^{-1}$ (see Figure 2.5). Other AM processes based on droplet deposition from a single nozzle, such as EHD, achieve throughputs of only 0.05-300 voxels s$^{-1}$, or at least three orders of magnitude slower. The advantage of parallelization has been utilized in recent works that developed new AM processes with light as the Energy Source. The Spadaccini group has shown that using optically-addressable light valve allows to melt and consolidate a large area of the powder bed, which can potentially increase the throughput of metal SLM by an order of magnitude [149]. In another work, Kelly et al. showed how a single light exposure can help create macroscale polymer objects in several seconds via tomographic reconstruction [150]. Carefully examining the shape definition

approach in the context of AM Process Framework can help identify opportunities in increasing the throughput of AM by parallelization or by using alternative shape definition.

*AM of New Materials*

Adopting an existing AM process to 3D print a new material can be very challenging and require an amount of effort comparable to developing an altogether new process. For example, it took many years to achieve reliable printing of copper components using powder bed processes due to high thermal conductivity and high reflectivity of Cu [151]. Extension of an AM process to other materials is limited by specific aspects of manipulating the chosen material feedstock. Limitation of hybrid organic-inorganic materials synthesized and utilized in this work is that the metal atom that is incorporated into the polymer backbone is in inherently in an oxidized state; converting to a non-oxidized state without the loss of 3D geometry is not guaranteed.

For example, consider developing an AM process for Si using hybrid organic-inorganic materials. Silicon atoms can be incorporated into the polymer network using siloxanes, and a photopolymer based on free-radical polymerization of acrylates can formulated. In fact, this approach has been demonstrated by HRL for 3D printing of SiC and SiOC [28] and has even been extended to nanoscale AM [152]. Converting the resulting 3D hybrid material to 3D silicon is very challenging using thermal processing. Hydrothermal reduction of silicon oxide and silicon oxycarbide to silicon is not thermodynamically favorable, and carbothermal reduction of silicon oxide to silicon requires high temperatures that will melt away the 3D geometry. It appears that hybrid materials might not be the best material feedstock for 3D printing of silicon. Examining alternative material feedstocks that can

enable nanoscale resolution (Figure 1.5) reveals that selective decomposition of a liquid or gas precursor (e.g., tetrachlorosilane, $SiCl_4$) can potentially be a better candidate for nanoscale AM of Si. The choice of material feedstock needs to be carefully evaluated to consider whether an existing AM process can be extended to 3D print a novel material.

*Development of New AM Processes*

The AM Process Framework can be a useful tool for evaluating the emerging nanoscale AM processes, as well as in potentially designing new AM processes. Examining different combinations of a material feedstock, an energy source, and a shape definition approach can yield novel AM process candidates. As an example, we can consider some of the most recent advances in AM that utilize material feedstocks that allow for nanoscale 3D printing, namely liquid photopolymers, metal-containing gases, and metal ions (see Figure 1.5). These recent processes and their fit into the AM process framework are illustrated in Figure 6.2.

Cross-linking hydrogels with a focused X-ray beam allowed for nanoscale polymer 3D printing using a scanning X-ray microscope system [153]. Local decomposition of a metal-containing gas precursor with a focused electron beam at cryogenic temperatures, or Cryo-FEBID, enabled nanofabrication of 3D metal/carbon composites [50]. Two-photon lithography of metal-ion-based photoresins followed by calcination allowed for AM of 3D nano-architected metal oxides [58]. Needless to mention that selecting a random combination of a material feedstock, an energy source, and a shape definition method does not guarantee a viable AM process candidate. However, it can provide a valuable first iteration of the future AM process together with reasonable expectations of the resolution, the minimal feature size, and the throughput.
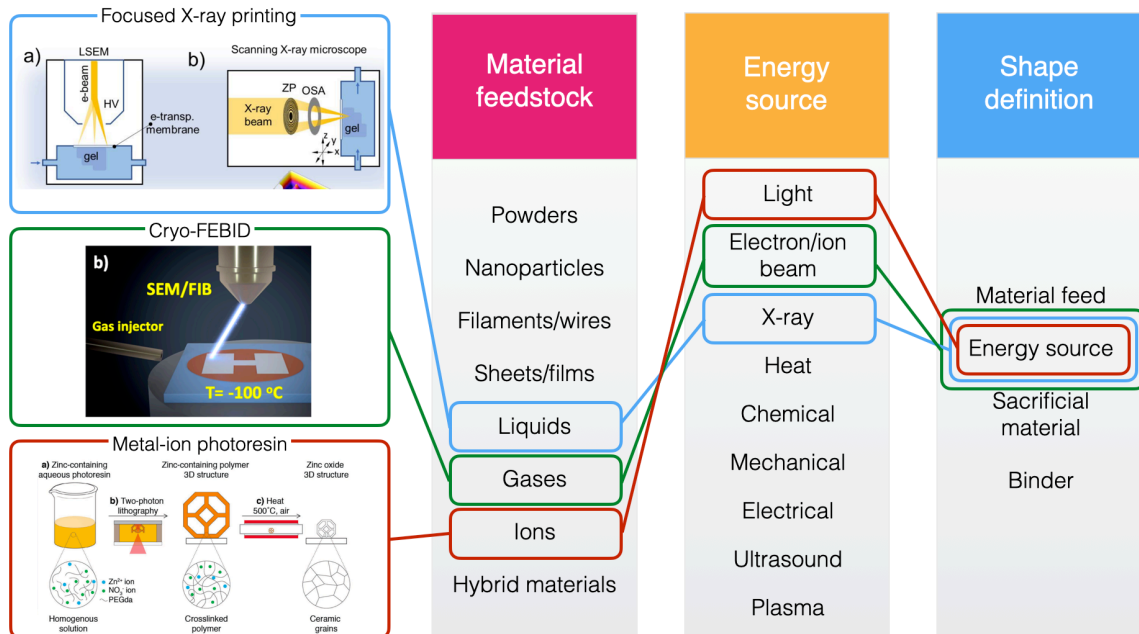
Figure 6.2. Recent nanoscale AM processes and how they fit into the AM process framework.

Inset images reproduced from [58] with permission from John Wiley and Sons, from [50] (MDPI, open-source), and [153] with permission from Dr. Andrei Kolmakov

This work established a versatile and efficient pathway to create three-dimensional nano-architected metals and ceramics and to investigate their mechanical, optical, and photocatalytic properties. Nanoscale AM of 3D nano-architected metals and ceramics will become the enabling technology for efficient 3D microelectromechanical systems (MEMS), 3D micro-battery electrodes, 3D electrically small antennae, micro-optical components, and photonics.

# BIBLIOGRAPHY

[1]     A. Zocca, P. Colombo, C.M. Gomes, J. Günster, Additive Manufacturing of Ceramics: Issues, Potentialities, and Opportunities., J. Am. Ceram. Soc. 98 (2015) 1983–2001. http://10.0.4.87/jace.13700.

[2]     F.P.W. Melchels, M.A.N. Domingos, T.J. Klein, J. Malda, P.J. Bartolo, D.W. Hutmacher, Additive manufacturing of tissues and organs, Prog. Polym. Sci. 37 (2012) 1079–1104. doi:https://doi.org/10.1016/j.progpolymsci.2011.11.007.

[3]     W.E. Frazier, Metal Additive Manufacturing: A Review, J. Mater. Eng. Perform. 23 (2014) 1917–1928. doi:10.1007/s11665-014-0958-z.

[4]     F. Martina, J. Mehnen, S.W. Williams, P. Colegrove, F. Wang, Investigation of the benefits of plasma deposition for the additive layer manufacture of Ti–6Al–4V, J. Mater. Process. Technol. 212 (2012) 1377–1386. doi:http://doi.org/10.1016/j.jmatprotec.2012.02.002.

[5]     P. Heinl, L. Müller, C. Körner, R.F. Singer, F.A. Müller, Cellular Ti–6Al–4V structures with interconnected macro porosity for bone implants fabricated by selective electron beam melting, Acta Biomater. 4 (2008) 1536–1544. doi:http://doi.org/10.1016/j.actbio.2008.03.013.

[6]     M. Vaezi, H. Seitz, S. Yang, A review on 3D micro-additive manufacturing technologies, Int. J. Adv. Manuf. Technol. 67 (2013) 1721–1754. doi:10.1007/s00170-012-4605-2.

[7]     L. Hirt, A. Reiser, R. Spolenak, T. Zambelli, Additive Manufacturing of Metal Structures at the Micrometer Scale, Adv. Mater. (2017) 1604211-n/a. doi:10.1002/adma.201604211.

[8]     C. Fei Guo, T. Sun, F. Cao, Q. Liu, Z. Ren, Metallic nanostructures for light trapping in energy-harvesting devices, Light Sci Appl. 3 (2014) e161. http://dx.doi.org/10.1038/lsa.2014.42.

[9]     R. Maaß, S. Van Petegem, D. Ma, J. Zimmermann, D. Grolimund, F. Roters, et al., Smaller is stronger: The effect of strain hardening, Acta Mater. 57 (2009) 5996–6005. doi:http://dx.doi.org/10.1016/j.actamat.2009.08.024.

[10]   X.W. Gu, C.N. Loynachan, Z. Wu, Y.-W. Zhang, D.J. Srolovitz, J.R. Greer, Size-Dependent Deformation of Nanocrystalline Pt Nanopillars, Nano Lett. 12 (2012) 6385–6392. doi:10.1021/nl3036993.

[11]   X. Wendy Gu, J.R. Greer, Ultra-strong architected Cu meso-lattices, Extrem. Mech. Lett. 2 (2015) 7–14. doi:10.1016/j.eml.2015.01.006.

[12]   T.A. Schaedler, A.J. Jacobsen, A. Torrents, A.E. Sorensen, J. Lian, J.R. Greer, et al., Ultralight Metallic Microlattices, Science (80-. ). 334 (2011) 962 LP – 965. http://science.sciencemag.org/content/334/6058/962.abstract.

[13]   D. Jang, L.R. Meza, F. Greer, J.R. Greer, Fabrication and deformation of three-dimensional hollow ceramic nanostructures, Nat. Mater. 12 (2013) 893–898. doi:10.1038/nmat3738.

[14]   L.C. Montemayor, J.R. Greer, Mechanical Response of Hollow Metallic Nanolattices: Combining Structural and Material Size Effects, J. Appl. Mech. 82

(2015) 71010–71012. http://dx.doi.org/10.1115/1.4030361.

[15]   R. Liontas, J.R. Greer, 3D nano-architected metallic glass: Size effect suppresses catastrophic failure, Acta Mater. 133 (2017) 393–407. doi:https://doi.org/10.1016/j.actamat.2017.05.019.

[16]   R.A. Sobieszek, Sculpture as the Sum of its Profiles: François Willème and Photosculpture in France, 1859–1868, Art Bull. 62 (1980) 617–630. doi:10.1080/00043079.1980.10787818.

[17]   J.E. BLANTHER, Manufacture of contour relief-maps, US473901A, 1892. https://patents.google.com/patent/US473901A/en (accessed April 13, 2020).

[18]   D.L. Bourell, Perspectives on Additive Manufacturing, Annu. Rev. Mater. Res. 46 (2016) 1–18. doi:10.1146/annurev-matsci-070115-031606.

[19]   B.K. Singh, S. Rupinder, S. Harwinder, Development of rapid tooling using fused deposition modeling: a review, Rapid Prototyp. J. 22 (2016) 281–299. doi:10.1108/RPJ-04-2014-0048.

[20]   K.P. Karunakaran, A. Bernard, S. Suryakumar, L. Dembinski, G. Taillandier, Rapid manufacturing of metallic objects, Rapid Prototyp. J. 18 (2012) 264–280. doi:10.1108/13552541211231644.

[21]   M-Flex, (n.d.). http://www.exone.com/Portals/0/Systems/M-Flex/X1_MFlex_US.pdf (accessed April 13, 2017).

[22]   Digital Metal. Additive manufacturing of small and complex metal parts, (n.d.). https://www.hoganas.com/globalassets/media/sharepoint-documents/BrochuresanddatasheetsAllDocuments/Additivemanufacturingofsmallandcomplexmetalparts_July_2016_1666HOG.pdf (accessed April 13, 2017).

[23]   Fabrisonic's SonicLayer 7200 Fully Automated System is a large-format metal 3D printer, (n.d.). http://www.plantservices.com/vendors/products/2015/fabrisonics-soniclayer-7200-fully-automated-system/ (accessed April 13, 2017).

[24]   S. Pereira, M. Wegener, G. von Freymann, C.M. Soukoulis, K. Busch, M. Deubel, Direct laser writing of three-dimensional photonic-crystal templates for telecommunications, Nat. Mater. 3 (2004) 444–447. doi:10.1038/nmat1155.

[25]   E. Kritchman, H. Gothait, T. Shmal, S. Yitzhaik, System and method for delivering ink into a 3d printing apparatus, US20180264731A1, 2018. https://patents.google.com/patent/US20180264731A1/en (accessed April 14, 2020).

[26]   D.D. Gu, W. Meiners, K. Wissenbach, R. Poprawe, Laser additive manufacturing of metallic components: materials, processes and mechanisms, Int. Mater. Rev. 57 (2012) 133–164. doi:10.1179/1743280411Y.0000000014.

[27]   K.M. Taminger, R.A. Hafley, Electron Beam Freeform Fabrication for Cost Effective Near-Net Shape Manufacturing, in: NATO/RTO AVT-139 Spec. Meet. Cost Eff. Manuf. via Net Shape Process. 15-17 May 2006; Amsterdam; Netherlands, 2006: p. 19p. https://ntrs.nasa.gov/archive/nasa/casi.ntrs.nasa.gov/20080013538.pdf (accessed April 25, 2017).

[28]   Z.C. Eckel, C. Zhou, J.H. Martin, A.J. Jacobsen, W.B. Carter, T.A. Schaedler, Additive manufacturing of polymer-derived ceramics, Science (80-. ). 351 (2016) 58–62. doi:10.1126/science.aad2688.

[29]    M.S. Saleh, C. Hu, R. Panat, Three-dimensional microarchitected materials and devices using nanoparticle assembly by pointwise spatial printing, Sci. Adv. 3 (2017). http://advances.sciencemag.org/content/3/3/e1601986.abstract.

[30]    C.-H. Wang, H.-L. Tsai, Y.-C. Wu, W.-S. Hwang, Investigation of molten metal droplet deposition and solidification for 3D printing techniques, J. Micromechanics Microengineering. 26 (2016) 095012. doi:10.1088/0960-1317/26/9/095012.

[31]    A. Cohen, R. Chen, U. Frodis, M. Wu, C. Folk, Microscale metal additive manufacturing of multi-component medical devices, Rapid Prototyp. J. 16 (2010) 209–215. doi:10.1108/13552541011034889.

[32]    T. Tanaka, Two-photon-induced reduction of metal ions for fabricating three-dimensional electrically conductive metallic microstructure, Appl. Phys. Lett. 88 (2006) 81107. doi:10.1063/1.2177636.

[33]    S. Shukla, E.P. Furlani, X. Vidal, M.T. Swihart, P.N. Prasad, Two-Photon Lithography of Sub-Wavelength Metallic Structures in a Polymer Matrix, Adv. Mater. 22 (2010) 3695–3699. doi:10.1002/adma.201000059.

[34]    P. Regenfuss, A. Streek, L. Hartwig, S. Klötzer, T. Brabant, M. Horn, et al., Principles of laser micro sintering, Rapid Prototyp. J. 13 (2007) 204–212. doi:10.1108/13552540710776151.

[35]    M.S. Onses, E. Sutanto, P.M. Ferreira, A.G. Alleyne, J.A. Rogers, Mechanisms, Capabilities, and Applications of High-Resolution Electrohydrodynamic Jet Printing, Small. 11 (2015) 4237–4266. doi:10.1002/smll.201500593.

[36]    T. Takai, H. Nakao, F. Iwata, Three-dimensional microfabrication using local electrophoresis deposition and a laser trapping technique, Opt. Express. 22 (2014) 28109–28117. doi:10.1364/OE.22.028109.

[37]    M.A. Skylar-Scott, S. Gunasekaran, J.A. Lewis, Laser-assisted direct ink writing of planar and 3D metal architectures, Proc. Natl. Acad. Sci. . 113 (2016) 6137–6142. doi:10.1073/pnas.1525131113.

[38]    E.B. Duoss, M. Twardowski, J.A. Lewis, Sol-gel inks for direct-write assembly of functional oxides, Adv. Mater. 19 (2007) 3485–3489. doi:10.1002/adma.200701372.

[39]    K.H. Haas, H. Wolter, Synthesis, properties and applications of inorganic-organic copolymers (ORMOCER®s), Curr. Opin. Solid State Mater. Sci. 4 (1999) 571–580. doi:10.1016/S1359-0286(00)00009-7.

[40]    L. Jonušauskas, D. Gailevičius, L. Mikoliunaite, D. Sakalauskas, S. Šakirzanovas, S. Juodkazis, et al., Optically clear and resilient free-form μ-optics 3D-printed via ultrafast laser lithography, Materials (Basel). 10 (2017) 1–18. doi:10.3390/ma10010012.

[41]    C.C. Yeh, H.C. Liu, W. Heni, D. Berling, H.W. Zan, O. Soppera, Chemical and structural investigation of zinc-oxo cluster photoresists for DUV lithography, J. Mater. Chem. C. (2017). doi:10.1039/C6TC05201K.

[42]    M. Malinauskas, A. Ukauskas, V. Purlys, A. Gaidukeviiut, Z. Baleviius, A. Piskarskas, et al., 3D microoptical elements formed in a photostructurable germanium silicate by direct laser writing, Opt. Lasers Eng. 50 (2012) 1785–1788. doi:10.1016/j.optlaseng.2012.07.001.

[43]  K.K.B. Hon, L. Li, I.M. Hutchings, Direct writing technology—Advances and developments, CIRP Ann. - Manuf. Technol. 57 (2008) 601–620. doi:http://doi.org/10.1016/j.cirp.2008.09.006.

[44]  F. Khodabakhshi, A.P. Gerlich, Potentials and strategies of solid-state additive friction-stir manufacturing technology: A critical review, J. Manuf. Process. 36 (2018) 77–92. doi:https://doi.org/10.1016/j.jmapro.2018.09.030.

[45]  S.K. Seol, D. Kim, S. Lee, J.H. Kim, W.S. Chang, J.T. Kim, Electrodeposition-based 3D Printing of Metallic Microarchitectures with Controlled Internal Structures, Small. 11 (2015) 3896–3902. doi:10.1002/smll.201500177.

[46]  L. Hirt, S. Ihle, Z. Pan, L. Dorwling-Carter, A. Reiser, J.M. Wheeler, et al., Template-Free 3D Microprinting of Metals Using a Force-Controlled Nanopipette for Layer-by-Layer Electrodeposition, Adv. Mater. 28 (2016) 2311–2315. doi:10.1002/adma.201504967.

[47]  B.W. An, K. Kim, H. Lee, S.-Y. Kim, Y. Shim, D.-Y. Lee, et al., High-Resolution Printing of 3D Structures Using an Electrohydrodynamic Inkjet with Multiple Functional Inks, Adv. Mater. 27 (2015) 4322–4328. doi:10.1002/adma.201502092.

[48]  J. Schneider, P. Rohner, D. Thureja, M. Schmid, P. Galliker, D. Poulikakos, Electrohydrodynamic NanoDrip Printing of High Aspect Ratio Metal Grid Transparent Electrodes, Adv. Funct. Mater. 26 (2016) 833–840. doi:10.1002/adfm.201503705.

[49]  J. Hu, M.F. Yu, Meniscus-confined three-dimensional electrodeposition for direct writing of wire bonds, Science (80-. ). 329 (2010) 313–316. doi:10.1126/science.1190496.

[50]  J.M. De Teresa, P. Orús, R. Córdoba, P. Philipp, Comparison between focused electron/ion beam-induced deposition at room temperature and under cryogenic conditions, Micromachines. 10 (2019) 799. doi:10.3390/mi10120799.

[51]  K. Murakami, M. Takai, Nano electron source fabricated by beam-induced deposition and its unique feature, Microelectron. Eng. 132 (2015) 74–82. doi:10.1016/j.mee.2014.10.004.

[52]  M. Zenou, A. Sa'ar, Z. Kotler, Laser jetting of femto-liter metal droplets for high resolution 3D printed structures, Sci. Rep. 5 (2015) 1–10. doi:10.1038/srep17265.

[53]  E. Blasco, J. Müller, P. Müller, V. Trouillet, M. Schön, T. Scherer, et al., Fabrication of Conductive 3D Gold-Containing Microstructures via Direct Laser Writing, Adv. Mater. 28 (2016) 3592–3595. doi:10.1002/adma.201506126.

[54]  M.G. Stanford, B.B. Lewis, J.H. Noh, J.D. Fowlkes, P.D. Rack, Inert Gas Enhanced Laser-Assisted Purification of Platinum Electron-Beam-Induced Deposits, ACS Appl. Mater. Interfaces. 7 (2015) 19579–19588. doi:10.1021/acsami.5b02488.

[55]  M. Zenou, Z. Kotler, Printing of metallic 3D micro-objects by laser induced forward transfer, Opt. Express. 24 (2016) 1431–1446. doi:10.1364/OE.24.001431.

[56]  J.H. Pikul, H. Gang Zhang, J. Cho, P. V Braun, W.P. King, High-power lithium ion microbatteries from interdigitated three-dimensional bicontinuous nanoporous electrodes, Nat. Commun. 4 (2013) 1732. http://dx.doi.org/10.1038/ncomms2747.

[57]  B.J. Nelson, I.K. Kaliakatsos, J.J. Abbott, Microrobots for Minimally Invasive Medicine, Annu. Rev. Biomed. Eng. 12 (2010) 55–85. doi:10.1146/annurev-

bioeng-010510-103409.

[58] D.W. Yee, M.L. Lifson, B.W. Edwards, J.R. Greer, Additive Manufacturing of 3D-Architected Multifunctional Metal Oxides, Adv. Mater. 1901345 (2019) 1–9. doi:10.1002/adma.201901345.

[59] S. Wong, M. Deubel, F. Pérez-Willard, S. John, G.A. Ozin, M. Wegener, et al., Direct laser writing of three-dimensional photonic crystals with a complete photonic bandgap in chalcogenide glasses, Adv. Mater. 18 (2006) 265–269. doi:10.1002/adma.200501973.

[60] A. Frölich, J. Fischer, T. Zebrowski, K. Busch, M. Wegener, Titania woodpiles with complete three-dimensional photonic bandgaps in the visible, Adv. Mater. 25 (2013) 3588–3592. doi:10.1002/adma.201300896.

[61] B.Y. Ahn, E.B. Duoss, M.J. Motala, X. Guo, S. Il Park, Y. Xiong, et al., Omnidirectional printing of flexible, stretchable, and spanning silver microelectrodes, Science (80-. ). 323 (2009) 1590–1593. doi:10.1126/science.1168375.

[62] P. Richner, H. Eghlidi, S.J.P. Kress, M. Schmid, D.J. Norris, D. Poulikakos, Printable Nanoscopic Metamaterial Absorbers and Images with Diffraction-Limited Resolution, ACS Appl. Mater. Interfaces. 8 (2016) 11690–11697. doi:10.1021/acsami.6b01585.

[63] G. Von Freymann, A. Ledermann, M. Thiel, I. Staude, S. Essig, K. Busch, et al., Three-dimensional nanostructures for photonics, Adv. Funct. Mater. 20 (2010) 1038–1052. doi:10.1002/adfm.200901838.

[64] M. Gavagnin, H.D. Wanzenboeck, S. Wachter, M.M. Shawrav, A. Persson, K. Gunnarsson, et al., Free-standing magnetic nanopillars for 3D nanomagnet logic, ACS Appl. Mater. Interfaces. 6 (2014) 20254–20260. doi:10.1021/am505785t.

[65] H.C. George, T.A. Orlova, A.O. Orlov, G.L. Snider, Novel method for fabrication of nanoscale single-electron transistors: Electron beam induced deposition of Pt and atomic layer deposition of tunnel barriers, J. Vac. Sci. Technol. B, Nanotechnol. Microelectron. Mater. Process. Meas. Phenom. 29 (2011) 06FB01. doi:10.1116/1.3640752.

[66] B. Bin Xu, H. Xia, L.G. Niu, Y.L. Zhang, K. Sun, Q.D. Chen, et al., Flexible nanowiring of metal on nonplanar substrates by femtosecond-laser-induced electroless plating, Small. 6 (2010) 1762–1766. doi:10.1002/smll.201000511.

[67] M. Focsan, A.M. Craciun, S. Astilean, P.L. Baldeck, Two-photon fabrication of three-dimensional silver microstructures in microfluidic channels for volumetric surface-enhanced Raman scattering detection, Opt. Mater. Express. 6 (2016) 1587. doi:10.1364/ome.6.001587.

[68] A. Camposeo, L. Persano, M. Farsari, D. Pisignano, Additive Manufacturing: Applications and Directions in Photonics and Optoelectronics, Adv. Opt. Mater. 7 (2019). doi:10.1002/adom.201800419.

[69] J. Liu, M. Ueda, High refractive index polymers: fundamental research and practical applications, J. Mater. Chem. 19 (2009) 8907. doi:10.1039/b909690f.

[70] W.L. Bond, Measurement of the refractive indices of several crystals, J. Appl. Phys. 36 (1965) 1674–1677. doi:10.1063/1.1703106.

[71] S. Passinger, M.S.M. Saifullah, C. Reinhardt, K.R. V Subramanian, B.N.

Chichkov, M.E. Welland, Direct 3D patterning of TiO2 using femtosecond laser pulses, Adv. Mater. 19 (2007) 1218–1221. doi:10.1002/adma.200602264.

[72] A. Vyatskikh, S. Delalande, A. Kudo, X. Zhang, C.M. Portela, J.R. Greer, Additive manufacturing of 3D nano-architected metals, Nat. Commun. 9 (2018) 593. doi:10.1038/s41467-018-03071-9.

[73] S. John, Strong localization of photons in certain disordered dielectric superlattices, Phys. Rev. Lett. 58 (1987) 2486–2489. doi:10.1103/PhysRevLett.58.2486.

[74] E. Yablonovitch, Inhibited Spontaneous Emission in Solid-State Physics and Electronics, Phys. Rev. Lett. 58 (1987) 2059–2062. doi:10.1103/PhysRevLett.58.2059.

[75] Susumu Noda, Katsuhiro Tomoda, Noritsugu Yamamoto, Alongkarn Chutinan, Full Three-Dimensional Photonic Bandgap Crystals at Near-Infrared Wavelengths, Science (80-. ). 289 (2000) 604–606. doi:10.1126/science.289.5479.604.

[76] I. Staude, M. Thiel, S. Essig, C. Wolff, K. Busch, G. von Freymann, et al., Fabrication and characterization of silicon woodpile photonic crystals with a complete bandgap at telecom wavelengths., Opt. Lett. 35 (2010) 1094–6. doi:10.1364/OL.35.001094.

[77] C. Luo, S.G. Johnson, J.D. Joannopoulos, All-angle negative refraction in a three-dimensionally periodic photonic crystal, Appl. Phys. Lett. 81 (2002) 2352–2354. doi:10.1063/1.1508807.

[78] K.M. Ho, C.T. Chan, C.M. Soukoulis, R. Biswas, M. Sigalas, Photonic band gaps in three dimensions: New layer-by-layer periodic structures, Solid State Commun. 89 (1994) 413–416. doi:10.1016/0038-1098(94)90202-X.

[79] V.F. Chernow, R.C. Ng, J.R. Greer, Designing core-shell 3D photonic crystal lattices for negative refraction, Proc. SPIE. 10112 (2017). doi:10.1117/12.2251545.

[80] K. Aoki, D. Guimard, M. Nishioka, M. Nomura, S. Iwamoto, Y. Arakawa, Coupling of quantum-dot light emission with a three-dimensional photonic-crystal nanocavity, Nat. Photonics. 2 (2008) 688–692. doi:10.1038/nphoton.2008.202.

[81] M.W. Ribarsky, - Titanium Dioxide (TiO2) (Rutile), in: E.D.B.T.-H. of O.C. of S. Palik (Ed.), Academic Press, Burlington, 1997: pp. 795–804. doi:https://doi.org/10.1016/B978-012544415-6.50042-X.

[82] S.-Y. Yu, G. Schrodj, K. Mougin, J. Dentzer, J.-P. Malval, H.-W. Zan, et al., Direct Laser Writing of Crystallized TiO2 and TiO2/Carbon Microstructures with Tunable Conductive Properties, Adv. Mater. 30 (2018) 1805093. doi:10.1002/adma.201805093.

[83] UN, The Millennium Development Goals Report 2015, 2015. http://www.un.org/millenniumgoals/2015_MDG_Report/pdf/MDG 2015 rev (July 1).pdf (accessed February 21, 2017).

[84] K.G. McGuigan, R.M. Conroy, H.-J. Mosler, M. du Preez, E. Ubomba-Jaswa, P. Fernandez-Ibañez, Solar water disinfection (SODIS): A review from bench-top to roof-top, J. Hazard. Mater. 235 (2012) 29–46. doi:10.1016/j.jhazmat.2012.07.053.

[85] Water, Sanitation & Hygiene - Bill & Melinda Gates Foundation, (n.d.). http://www.gatesfoundation.org/What-We-Do/Global-Development/Water-

Sanitation-and-Hygiene (accessed February 21, 2017).

[86]  R.P. Sinha, D.P. Häder, UV-induced DNA damage and repair: a review., Photochem. Photobiol. Sci. 1 (2002) 225–36. http://www.ncbi.nlm.nih.gov/pubmed/12661961 (accessed February 21, 2017).

[87]  S. Dong, J. Feng, M. Fan, Y. Pi, L. Hu, X. Han, et al., Recent developments in heterogeneous photocatalytic water treatment using visible light-responsive photocatalysts: a review, RSC Adv. 5 (2015) 14610–14630. doi:10.1039/C4RA13734E.

[88]  M.-S. Wong, W.-C. Chu, D.-S. Sun, H.-S. Huang, J.-H. Chen, P.-J. Tsai, et al., Visible-light-induced bactericidal activity of a nitrogen-doped titanium photocatalyst against human pathogens., Appl. Environ. Microbiol. 72 (2006) 6111–6. doi:10.1128/AEM.02580-05.

[89]  H. Bai, Z. Liu, D.D. Sun, Hierarchical ZnO/Cu "corn-like" materials with high photodegradation and antibacterial capability under visible light, Phys. Chem. Chem. Phys. 13 (2011) 6205. doi:10.1039/c0cp02546a.

[90]  C. Liu, D. Kong, P.-C. Hsu, H. Yuan, H.-W. Lee, Y. Liu, et al., Rapid water disinfection using vertically aligned MoS2 nanofilms and visible light, Nat. Nanotechnol. 11 (2016) 1098. doi:10.1038/nnano.2016.138.

[91]  J. Hoigné, Inter-calibration of OH radical sources and water quality parameters, Water Sci. Technol. 35 (1997) 1–8. doi:http://dx.doi.org/10.1016/S0273-1223(97)00002-4.

[92]  D.A. Keane, K.G. McGuigan, P.F. Ibáñez, M.I. Polo-López, J.A. Byrne, P.S.M. Dunlop, et al., Solar photocatalysis for water disinfection: materials and reactor design, Catal. Sci. Technol. 4 (2014) 1211–1226. doi:10.1039/C4CY00006D.

[93]  D. Spasiano, R. Marotta, S. Malato, P. Fernandez-Ibañez, I. Di Somma, Solar photocatalysis: Materials, reactors, some commercial, and pre-industrialized applications. A comprehensive approach, Appl. Catal. B Environ. 170–171 (2015) 90–123. doi:10.1016/j.apcatb.2014.12.050.

[94]  S.P. Krumdieck, R. Boichot, R. Gorthy, J.G. Land, S. Lay, A.J. Gardecka, et al., Nanostructured TiO 2 anatase-rutile-carbon solid coating with visible light antimicrobial activity, Sci. Rep. 9 (2019) 1–11. doi:10.1038/s41598-018-38291-y.

[95]  E.J.W. Crossland, N. Noel, V. Sivaram, T. Leijtens, J.A. Alexander-Webber, H.J. Snaith, Mesoporous TiO 2 single crystals delivering enhanced mobility and optoelectronic device performance, Nature. 495 (2013) 215–219. doi:10.1038/nature11936.

[96]  Z. Cai, J. Teng, Z. Xiong, Y. Li, Q. Li, X. Lu, et al., Fabrication of TiO2binary inverse opals without overlayers via the sandwich-vacuum infiltration of precursor, Langmuir. 27 (2011) 5157–5164. doi:10.1021/la200111j.

[97]  Y. Li, D.-S. Hwang, N.H. Lee, S.-J. Kim, Synthesis and characterization of carbon-doped titania as an artificial solar light sensitive photocatalyst, Chem. Phys. Lett. 404 (2005) 25–29. doi:https://doi.org/10.1016/j.cplett.2005.01.062.

[98]  *,† Jimmy C. Yu, † Wingkei Ho, † Jiaguo Yu, †,‡ Hoyin Yip, ‡ and Po Keung Wong, J. Zhao§, Efficient Visible-Light-Induced Photocatalytic Disinfection on Sulfur-Doped Nanocrystalline Titania, (2005). doi:10.1021/ES035374H.

[99]  Z. Wang, C. Yang, T. Lin, H. Yin, P. Chen, D. Wan, et al., H-Doped Black Titania

with Very High Solar Absorption and Excellent Photocatalysis Enhanced by Localized Surface Plasmon Resonance, Adv. Funct. Mater. 23 (2013) 5444–5450. doi:10.1002/adfm.201300486.

[100] R. Asahi, T. Morikawa, H. Irie, T. Ohwaki, Nitrogen-Doped Titanium Dioxide as Visible-Light-Sensitive Photocatalyst: Designs, Developments, and Prospects, Chem. Rev. 114 (2014) 9824–9852. doi:10.1021/cr5000738.

[101] Y. Li, X. Li, J. Li, J. Yin, Photocatalytic degradation of methyl orange in a sparged tube reactor with TiO2-coated activated carbon composites, Catal. Commun. 6 (2005) 650–655. doi:https://doi.org/10.1016/j.catcom.2005.06.008.

[102] S. KARINO, J. HOJO, Synthesis and characterization of $TiO_2$-coated $SiO_2$ particles by hydrolysis of titanium alkoxide in alcohol solvents, J. Ceram. Soc. Japan. 118 (2010) 591–596. doi:10.2109/jcersj2.118.591.

[103] M. Pelaez, P. Falaras, V. Likodimos, A.G. Kontos, A.A. de la Cruz, K. O'shea, et al., Synthesis, structural characterization and evaluation of sol–gel-based NF-TiO2 films with visible light-photoactivation for the removal of microcystin-LR, Appl. Catal. B Environ. 99 (2010) 378–387. doi:https://doi.org/10.1016/j.apcatb.2010.06.017.

[104] D.A.H. Hanaor, C.C. Sorrell, Sand Supported Mixed-Phase TiO2 Photocatalysts for Water Decontamination Applications, Adv. Eng. Mater. 16 (2014) 248–254. doi:10.1002/adem.201300259.

[105] S. Malato, P. Fernández-Ibáñez, M.I. Maldonado, J. Blanco, W. Gernjak, Decontamination and disinfection of water by solar photocatalysis: Recent overview and trends, Catal. Today. 147 (2009) 1–59. doi:https://doi.org/10.1016/j.cattod.2009.06.018.

[106] X. Ding, Y. Fan, N. Xu, A new route for the fabrication of TiO2 ultrafiltration membranes with suspension derived from a wet chemical synthesis, J. Memb. Sci. 270 (2006) 179–186. doi:http://dx.doi.org/10.1016/j.memsci.2005.07.003.

[107] M. Marszewski, S. Cao, J. Yu, M. Jaroniec, Semiconductor-based photocatalytic CO2 conversion, Mater. Horizons. 2 (2015) 261–278. doi:10.1039/C4MH00176A.

[108] J. Verran, G. Sandoval, N.S. Allen, M. Edge, J. Stratton, Variables affecting the antibacterial properties of nano and pigmentary titania particles in suspension, Dye. Pigment. 73 (2007) 298–304. doi:10.1016/j.dyepig.2006.01.003.

[109] D. Fattakhova-Rohlfing, A. Zaleska, T. Bein, Three-dimensional titanium dioxide nanomaterials, Chem. Rev. 114 (2014) 9487–9558. doi:10.1021/cr500201c.

[110] X. Wang, J. Feng, Y. Bai, Q. Zhang, Y. Yin, Synthesis, Properties, and Applications of Hollow Micro-/Nanostructures, Chem. Rev. 116 (2016) 10983–11060. doi:10.1021/acs.chemrev.5b00731.

[111] N. Kinadjian, M. Le Bechec, T. Pigot, F. Dufour, O. Durupthy, A. Bentaleb, et al., Photocatalytic TiO 2 macroscopic fibers obtained through integrative chemistry, Eur. J. Inorg. Chem. (2012) 5350–5359. doi:10.1002/ejic.201200731.

[112] S. Bai, J. Jiang, Q. Zhang, Y. Xiong, Steering charge kinetics in photocatalysis: intersection of materials syntheses, characterization techniques and theoretical simulations, Chem. Soc. Rev. 44 (2015) 2893–2939. doi:10.1039/C5CS00064E.

[113] D.W. McComb, B.M. Treble, C.J. Smith, R.M. De La Rue, N.P. Johnson, Synthesis and characterisation of photonic crystals, J. Mater. Chem. 11 (2001)

142–148. doi:10.1039/b003191g.

[114] L. Rozes, C. Sanchez, Titanium oxo-clusters: precursors for a Lego-like construction of nanostructured hybrid materials, Chem. Soc. Rev. 40 (2011) 1006–1030. doi:10.1039/C0CS00137F.

[115] Datasheet, IP-Photoresists, Nanoscribe GmbH, (n.d.). http://www.nanoscribe.de/files/1814/0662/4393/IP-Resist_IP-Dip_web.pdf (accessed August 28, 2017).

[116] D.-W. Wang, F. Li, G.Q. Lu, H.-M. Cheng, Synthesis and dye separation performance of ferromagnetic hierarchical porous carbon, Carbon N. Y. 46 (2008) 1593–1599. doi:10.1016/j.carbon.2008.06.052.

[117] S.-W. Lee, M. Jafary-Zadeh, D.Z. Chen, Y.-W. Zhang, J.R. Greer, Size Effect Suppresses Brittle Failure in Hollow Cu60Zr40 Metallic Glass Nanolattices Deformed at Cryogenic Temperatures, Nano Lett. 15 (2015) 5673–5681. doi:10.1021/acs.nanolett.5b01034.

[118] L.J. Gibson, M.F. Ashby, Cellular Solids, 1997. doi:10.1017/CBO9781139878326.

[119] S. Tsopanos, R.A.W. Mines, S. McKown, Y. Shen, W.J. Cantwell, W. Brooks, et al., The Influence of Processing Parameters on the Mechanical Properties of Selectively Laser Melted Stainless Steel Microlattice Structures, J. Manuf. Sci. Eng. 132 (2010) 41011–41012. http://dx.doi.org/10.1115/1.4001743.

[120] V.J. Challis, X. Xu, L.C. Zhang, A.P. Roberts, J.F. Grotowski, T.B. Sercombe, High specific strength and stiffness structures produced using selective laser melting, Mater. Des. 63 (2014) 783–788. doi:http://dx.doi.org/10.1016/j.matdes.2014.05.064.

[121] M. Speirs, B. Van Hooreweder, J. Van Humbeeck, J.-P. Kruth, Fatigue behaviour of NiTi shape memory alloy scaffolds produced by SLM, a unit cell design comparison, J. Mech. Behav. Biomed. Mater. 70 (2017) 53–59. doi:https://doi.org/10.1016/j.jmbbm.2017.01.016.

[122] E. Hernández-Nava, C.J. Smith, F. Derguti, S. Tammas-Williams, F. Leonard, P.J. Withers, et al., The effect of defects on the mechanical response of Ti-6Al-4V cubic lattice structures fabricated by electron beam melting, Acta Mater. 108 (2016) 279–292. doi:http://dx.doi.org/10.1016/j.actamat.2016.02.029.

[123] C. Yan, L. Hao, A. Hussein, S.L. Bubb, P. Young, D. Raymont, Evaluation of light-weight AlSi10Mg periodic cellular lattice structures fabricated via direct metal laser sintering, J. Mater. Process. Technol. 214 (2014) 856–864. doi:http://dx.doi.org/10.1016/j.jmatprotec.2013.12.004.

[124] Ti6Al4V ELI Titanium Alloy Arcam EBM system, (n.d.). http://www.arcam.com/wp-content/uploads/Arcam-Ti6Al4V-ELI-Titanium-Alloy.pdf (accessed July 5, 2017).

[125] Material data sheet. EOS Aluminium AlSi10Mg for EOSINT M 270, (n.d.). https://www.anubis3d.com/documents/dmls/datasheets/Aluminum-AlSi10Mg.pdf (accessed July 5, 2017).

[126] J.J. Lander, H.E. Kern, A.L. Beach, Solubility and Diffusion Coefficient of Carbon in Nickel: Reaction Rates of Nickel-Carbon Alloys with Barium Oxide, J. Appl. Phys. 23 (1952) 1305–1309. doi:10.1063/1.1702064.

[127] D.N. Leonard, G.W. Chandler, S. Seraphin, Scanning Electron Microscopy, in:

Charact. Mater., John Wiley & Sons, Inc., 2002.
doi:10.1002/0471266965.com081.pub2.

[128] C.-M. Wang, D.R. Baer, S.M. Bruemmer, M.H. Engelhard, M.E. Bowden, J.A. Sundararajan, et al., Microstructure of the Native Oxide Layer on Ni and Cr-Doped Ni Nanoparticles, J. Nanosci. Nanotechnol. 11 (2011) 8488–8497. doi:10.1166/jnn.2011.4964.

[129] J. Biener, A.M. Hodge, J.R. Hayes, C.A. Volkert, L.A. Zepeda-Ruiz, A. V Hamza, et al., Size Effects on the Mechanical Behavior of Nanoporous Au, Nano Lett. 6 (2006) 2379–2382. doi:10.1021/nl061978i.

[130] L.R. Meza, S. Das, J.R. Greer, Strong, lightweight, and recoverable three-dimensional ceramic nanolattices, Science (80-. ). 345 (2014) 1322 LP – 1326. http://science.sciencemag.org/content/345/6202/1322.abstract.

[131] A. Vyatskikh, R.C. Ng, B. Edwards, J.R. Greer, Additive manufacturing of titanium dioxide for dielectric photonic crystals, in: Proc.SPIE, 2019. https://doi.org/10.1117/12.2507076.

[132] H.B. Sun, T. Tanaka, S. Kawata, Three-dimensional focal spots related to two-photon excitation, Appl. Phys. Lett. 80 (2002) 3673–3675. doi:10.1063/1.1478128.

[133] J. Serbin, A. Egbert, A. Ostendorf, B.N. Chichkov, R. Houbertz, G. Domann, et al., Femtosecond laser-induced two-photon polymerization of inorganic–organic hybrid materials for applications in photonics, Opt. Lett. 28 (2003) 301. doi:10.1364/OL.28.000301.

[134] N. Uppal, Modeling of temperature-dependent diffusion and polymerization kinetics and their effects on two-photon polymerization dynamics, J. Micro/Nanolithography, MEMS, MOEMS. (2008). doi:10.1117/1.3033203.

[135] J.B. Mueller, J. Fischer, F. Mayer, M. Kadic, M. Wegener, Polymerization Kinetics in Three-Dimensional Direct Laser Writing, Adv. Mater. 26 (2014) 6566–6571. doi:10.1002/adma.201402366.

[136] J.B. Mueller, J. Fischer, Y.J. Mange, T. Nann, M. Wegener, In-situ local temperature measurement during three-dimensional direct laser writing, Appl. Phys. Lett. 103 (2013). doi:10.1063/1.4821556.

[137] D.C. Montgomery, Design and Analysis of Experiments, John Wiley &#38; Sons, Inc., USA, 2006.

[138] A.R. Forouhi, I. Bloomer, Optical dispersion relations for amorphous semiconductors and amorphous dielectrics, Phys. Rev. B. 34 (1986) 7018–7026. doi:10.1103/PhysRevB.34.7018.

[139] O. Frank, M. Zukalova, B. Laskova, J. Kürti, J. Koltai, L. Kavan, Raman spectra of titanium dioxide (anatase, rutile) with identified oxygen isotopes (16, 17, 18), Phys. Chem. Chem. Phys. 14 (2012) 14567–14572. doi:10.1039/c2cp42763j.

[140] X.Z. Ding, Z.A. Qi, Y.Z. He, Effect of tin dioxide doping on rutile phase formation in sol-gel-derived nanocrystalline titania powders, Nanostructured Mater. 4 (1994) 663–668. doi:10.1016/0965-9773(94)90018-3.

[141] C.-C. Yeh, H.-C. Liu, W. Heni, D. Berling, H.-W. Zan, O. Soppera, Chemical and structural investigation of zinc-oxo cluster photoresists for DUV lithography, J. Mater. Chem. C. 5 (2017) 2611–2619. doi:10.1039/C6TC05201K.

[142] H. Tiainen, S.P. Lyngstadaas, J.E. Ellingsen, H.J. Haugen, Ultra-porous titanium

oxide scaffold with high compressive strength, J. Mater. Sci. Mater. Med. 21 (2010) 2783–2792. doi:10.1007/s10856-010-4142-1.

[143] R. Saive, H.A. Atwater, Mesoscale trumps nanoscale: metallic mesoscale contact morphology for improved light trapping, optical absorption and grid conductance in silicon solar cells, Opt. Express. 26 (2018) A275–A282. doi:10.1364/OE.26.00A275.

[144] R.K. Singh, V. Babu, L. Philip, S. Ramanujam, Disinfection of Water Using Pulsed Power Technique: Effect of System Parameters and Kinetic Study BT - Sustainability Issues in Civil Engineering, in: G.L. Sivakumar Babu, S. Saride, B.M. Basha (Eds.), Springer Singapore, Singapore, 2017: pp. 307–336. doi:10.1007/978-981-10-1930-2_17.

[145] A. Fujishima, X. Zhang, D.A. Tryk, TiO2 photocatalysis and related surface phenomena, Surf. Sci. Rep. 63 (2008) 515–582. doi:https://doi.org/10.1016/j.surfrep.2008.10.001.

[146] Y. Ma, X. Wang, Y. Jia, X. Chen, H. Han, C. Li, Titanium Dioxide-Based Nanomaterials for Photocatalytic Fuel Generations, Chem. Rev. 114 (2014) 9987–10043. doi:10.1021/cr500008u.

[147] X. Chen, S.S. Mao, Titanium Dioxide Nanomaterials: Synthesis, Properties, Modifications, and Applications, Chem. Rev. 107 (2007) 2891–2959. doi:10.1021/cr0500535.

[148] D. Jang, J.R. Greer, Size-induced weakening and grain boundary-assisted deformation in 60 nm grained Ni nanopillars, Scr. Mater. 64 (2011) 77–80. doi:https://doi.org/10.1016/j.scriptamat.2010.09.010.

[149] M.J. Matthews, G. Guss, D.R. Drachenberg, J.A. Demuth, J.E. Heebner, E.B. Duoss, et al., Diode-based additive manufacturing of metals using an optically-addressable light valve, Opt. Express. 25 (2017) 11788–11800. doi:10.1364/OE.25.011788.

[150] H.K.T. Brett E. Kelly, Indrasen Bhattacharya, Hossein Heidari, Maxim Shusteff, Christopher M. Spadaccini, Volumetric additive manufacturing via tomographic reconstruction, 7114 (2019) 21.

[151] F. Singer, D.C. Deisenroth, D.M. Hymas, M.M. Ohadi, Additively manufactured copper components and composite structures for thermal management applications, in: 2017 16th IEEE Intersoc. Conf. Therm. Thermomechanical Phenom. Electron. Syst., 2017: pp. 174–183. doi:10.1109/ITHERM.2017.7992469.

[152] J. Bauer, C. Crook, A. Guell Izard, Z.C. Eckel, N. Ruvalcaba, T.A. Schaedler, et al., Additive Manufacturing of Ductile, Ultrastrong Polymer-Derived Nanoceramics, Matter. 1 (2019) 1547–1556. doi:10.1016/j.matt.2019.09.009.

[153] T. Gupta, E. Strelcov, G. Holland, J. Schumacher, Y. Yang, M. Esch, et al., Focused Electron and X-ray Beam Crosslinking in Liquids for Nanoscale Hydrogels 3D Printing and Encapsulation, ArXiv E-Prints. (2019) arXiv:1904.01652. https://ui.adsabs.harvard.edu/abs/2019arXiv190401652G.

[154] Selective Laser Melting Machine, (n.d.). https://slm-solutions.com/sites/default/files/attachment/page/2016/11/w_slm125_en.pdf (accessed April 13, 2017).

[155] BeAM Mobile Machine, (n.d.). http://www.beam-machines.fr/uploads/files/leaflets

mobile en_10.02.2016.pdf (accessed April 13, 2017).

[156] NORSK TITANIUM MERKE IV, (n.d.). http://www.norsktitanium.com/wp-content/uploads/2016/07/Norsk_Titanium_Brochure.pdf (accessed April 13, 2017).

[157] Metal Additive Manufacturing Systems - EBAM® Systems | Sciaky, (n.d.). http://www.sciaky.com/additive-manufacturing/metal-additive-manufacturing-systems (accessed April 13, 2017).

[158] Sciaky Discusses 2015 3D Printing Plans - 3D Printing Industry, (n.d.). https://3dprintingindustry.com/news/sciakys-john-ohara-ebam-technologys-3d-printing-projects-2015-40284/ (accessed April 13, 2017).

[159] A.B. Kair, K. Sofos, Additive Manufacturing and Production of Metallic Parts in Automotive Industry A Case Study on Technical , Economic and Environmental Sustainability Aspects, 2014.

[160] E. Brandl, U. Heckenberger, V. Holzinger, D. Buchbinder, Additive manufactured AlSi10Mg samples using Selective Laser Melting (SLM): Microstructure, high cycle fatigue, and fracture behavior, Mater. Des. 34 (2012) 159–169. doi:http://doi.org/10.1016/j.matdes.2011.07.067.

[161] C. Kullmann, N.C. Schirmer, M.-T. Lee, S.H. Ko, N. Hotz, C.P. Grigoropoulos, et al., 3D micro-structures by piezoelectric inkjet printing of gold nanofluids, J. Micromechanics Microengineering. 22 (2012) 055022. doi:10.1088/0960-1317/22/5/055022.

[162] C.W. Visser, R. Pohl, C. Sun, G.-W. Römer, B. Huis in 't Veld, D. Lohse, Toward 3D Printing of Pure Metals by Laser-Induced Forward Transfer, Adv. Mater. 27 (2015) 4087–4092. doi:10.1002/adma.201501058.

[163] H. Plank, C. Gspan, M. Dienstleder, G. Kothleitner, F. Hofer, The influence of beam defocus on volume growth rates for electron beam induced platinum deposition, Nanotechnology. 19 (2008) 485302. doi:10.1088/0957-4484/19/48/485302.

[164] M. Bresin, M. Toth, K.A. Dunn, Direct-write 3D nanolithography at cryogenic temperatures, Nanotechnology. 24 (2013) 035301. doi:10.1088/0957-4484/24/3/035301.

# APPENDIX A: SPECIFIC STRENGTH OF SOLID-BEAM METAL LATTICES FABRICATED USING METAL AM PROCESSES AND ELECTROPLATING INTO A TEMPLATE

| Material | Lattice Type | Process | Beam diameter, μm | Strength, MPa | Relative density | Material density, g/cm$^3$ | Lattice density, g/cm$^3$ | Specific strength, MPa/(g/cm$^3$) | Ref. |
|---|---|---|---|---|---|---|---|---|---|
| Ti-6Al-4V | Cubic | Electron Beam Melting (EBM) | 810 | 23.70 | 0.063 | 4.43 | 0.26 | 84.92 | [122] |
| | | | 970 | 34.70 | 0.078 | | 0.32 | 100.42 | |
| | | | 1480 | 89.10 | 0.159 | | 0.65 | 126.50 | |
| | | | 1780 | 180.20 | 0.216 | | 0.88 | 188.32 | |
| Ti-6Al-4V | Topology-optimized | Selective Laser Melting (SLM) | 406 | 30.00 | | n/a | 0.50 | 60.00 | [120] |
| AlSi10Mg | Diamond | Direct Metal Laser Sintering (DMLS) | 405 | 1.42 | 0.050 | 2.67 | 0.12 | 10.63 | [123] |
| | | | 502 | 4.72 | 0.075 | | 0.17 | 23.54 | |
| | | | 659 | 8.54 | 0.100 | | 0.23 | 31.98 | |
| | | | 765 | 12.61 | 0.125 | | 0.29 | 37.76 | |
| | | | 862 | 17.40 | 0.150 | | 0.35 | 43.45 | |
| Stainless steel 316L | BCC | Selective Laser Melting (SLM) | 162 | 0.20 | 0.023 | n/a | 0.19 | 1.05 | [119] |
| | | | 181 | 0.33 | 0.029 | | 0.23 | 1.43 | |
| | | | 181 | 0.33 | 0.029 | | 0.23 | 1.43 | |
| | | | 197 | 0.45 | 0.034 | | 0.28 | 1.61 | |
| | | | 197 | 0.45 | 0.035 | | 0.28 | 1.61 | |
| | | | 212 | 0.58 | 0.040 | | 0.32 | 1.81 | |
| | | | 212 | 0.60 | 0.041 | | 0.33 | 1.82 | |
| | | | 186 | 0.38 | 0.031 | | 0.25 | 1.52 | |
| | | | 210 | 0.55 | 0.039 | | 0.31 | 1.77 | |
| | | | 230 | 0.79 | 0.047 | | 0.38 | 2.08 | |
| | | | 249 | 1.00 | 0.055 | | 0.44 | 2.27 | |
| | | | 165 | 0.32 | 0.030 | | 0.24 | 1.33 | |
| | | | 166 | 0.33 | 0.032 | | 0.26 | 1.27 | |
| | | | 186 | 0.47 | 0.036 | | 0.29 | 1.62 | |
| | | | 188 | 0.46 | 0.034 | | 0.28 | 1.64 | |
| | | | 222 | 0.83 | 0.047 | | 0.38 | 2.18 | |
| | | | 211 | 0.73 | 0.043 | | 0.34 | 2.15 | |
| Silver | Octahedral | Pointwise Spatial Printing | 35 | 0.60 | 0.065 | n/a | 0.50 | 1.20 | [29] |
| | | | 38 | 1.27 | 0.270 | | 1.74 | 0.73 | |
| NiTi | Octahedral Cellular gyroid | Selective laser | 248 | 21.00 | 0.252 | 6.45 | 1.63 | 12.92 | [121] |
| | | | 298 | 29.00 | 0.252 | | 1.63 | 17.84 | |

| | | | | | | | | | |
|---|---|---|---|---|---|---|---|---|---|
| | Sheet gyroid | melting (SLM) | 210 | 44.00 | 0.266 | | 1.72 | 25.65 | |
| Copper | Octet | Electroplating into a template | 1.011 | 221.84 | 0.53 | | 4.72 | 46.95 | [11] |
| | | | 1.025 | 136.29 | 0.54 | | 4.82 | 28.28 | |
| | | | 1.050 | 158.23 | 0.56 | | 5.02 | 31.52 | |
| | | | 1.098 | 179.54 | 0.60 | | 5.35 | 33.54 | |
| | | | 1.164 | 154.11 | 0.65 | 8.96 | 5.80 | 26.57 | |
| | | | 1.178 | 241.14 | 0.66 | | 5.91 | 40.82 | |
| | | | 1.218 | 296.10 | 0.69 | | 6.18 | 47.93 | |
| | | | 1.323 | 266.56 | 0.76 | | 6.83 | 39.02 | |
| | | | 1.340 | 271.62 | 0.77 | | 6.93 | 39.18 | |
| | | | 1.378 | 332.70 | 0.80 | | 7.16 | 46.48 | |
| Nickel | Octet | This work | 0.30 | 18.17 | | | 2.52 | 7.20 | |
| | | | 0.30 | 17.08 | | | 2.55 | 6.71 | |
| | | | 0.28 | 8.91 | | | 2.60 | 3.42 | |
| | | | 0.27 | 8.18 | | | 2.75 | 2.98 | |
| | | | 0.35 | 6.94 | | 8.91 | 3.03 | 2.29 | |
| | | | 0.42 | 9.71 | | | 3.30 | 2.95 | |
| | | | 0.32 | 12.31 | | | 2.94 | 4.19 | |
| | | | 0.36 | 12.87 | | | 4.01 | 3.21 | |
| | | | 0.33 | 7.50 | | | 3.65 | 2.05 | |
| | | | 0.32 | 8.81 | | | 3.03 | 2.91 | |

# APPENDIX B: COMPARISON OF MINIMUM FEATURE SIZES FOR METAL ADDITIVE MANUFACTURING TECHNOLOGIES

| # | Technology/reference | Machine/company/setup | Layer thickness range, μm | | Lateral feature range, μm | | Beam diameter, μm | Ref. |
|---|---|---|---|---|---|---|---|---|
| | | | Min | Max | Min | Max | | |
| 1 | Selective Laser Melting (SLM) | SLM Solutions SLM 125 | 20 | 75 | 140 | | | [154] |
| 2 | Direct Metal Laser Sintering (DMLS) | EOS | 20 | 80 | 300 | 700 | | [20] |
| 3 | Electron Beam Melting (EBM) | Arcam | 50 | 200 | 500 | | | [20] |
| 4 | LaserCUSING | CONCEPT Laser M1 Cusing | 20 | 80 | | | | [20] |
| 5 | Digital Part Materialization | ExOne M-Flex | 100 | | 60 | 63.1 | | [20,21] |
| 6 | Direct Metal Deposition (DMD) | POM DMD 105D | 100 | 1600 | | | | [20] |
| 7 | Laser Engineered Net Shaping (LENS) | Optomec LENS MR-7 | 25 | | | | 250 | [20] |
| 8 | Laser Metal Deposition (LMD) | BeAM MOBILE Machine | 100 | | 800 | 1200 | | [155] |
| 9 | Rapid Plasma Deposition | NORSK TITANIUM MERKE IV | 3000 | 4000 | 8000 | 12000 | | [156] |
| 10 | Electron Beam Free Form Fabrication (EBF3) | Sciaky EBAM 300 | | | 3000 | 10000 | | [157,158] |
| 11 | Ultrasonic Consolidation (UC) | Fabrisonic SonicLayer 7200 | 1500 | 2500 | | | | [23] |
| 12 | Metal Powder Bed Fusion | Renishaw AM250 | 20 | 100 | | | | [159] |
| 13 | Direct Laser Forming | Trumpf TrumaForm LF130 | 50 | | | | 200 | [160] |
| 14 | Digital Metal | Höganäs | 20 | | 40 | | | [6,22] |
| 15 | Electrochemical Fabrication (EFAB) | Microfabrica | 4 | | 10 | | | [31] |
| 16 | Regenfuss et al., 2007 | Powder-based | 10 | | 55 | 60 | | [34] |
| 17 | Kullman et al., 2012 | Wire-based | | | 50 | 250 | | [161] |
| 18 | Saleh et al., 2017 | Inkjet-based | 10 | 20 | 30 | 55 | | [29] |
| 19 | Takai et al., 2014 | Local electrophoresis | | | 0.5 | 2.0 | | [36] |
| 20 | Hirt et al., 2016 | Local electroplating | 0.25 | | 0.8 | 5.0 | | [46] |
| 21 | Visser et al., 2015 | Laser-Induced Forward Transfer (LIFT) | | | 4 | 6 | | [162] |
| 22 | Scylar-Scott et al., 2016 | Laser-assisted Direct Ink Writing (DIW) | | | 0.6 | 20 | | [37] |
| 23 | This work | Nanoscribe Photonic Professional GT | | 0.03 | 0.025 | 0.4 | | |

# APPENDIX C: COMPARISON OF LINEAR AND VOLUMETRIC THROUGHPUTS OF REPRESENTATIVE MICRO- AND NANO-SCALE METAL ADDITIVE MANUFACTURING TECHNOLOGIES

Data adopted from ref.[7]

| # | Technology | Material | Feature size, μm | Writing speed[*] | Ref. |
|---|------------|----------|------------------|-----------------|------|
| 1 | Direct Ink Writing (DIW) | Ag | 0.6-20 | 500-2000 μm s$^{-1}$ | [37] |
| 2 | Electrohydrodynamic (EHD) Printing | Ag, Co, Cu | 0.7-3.0 | 0.16-3.3 μm s$^{-1}$ | [47] |
| 3 | Laser-Induced Forward Transfer (LIFT) | Au, Cu | 4.0-6.0 | 3000 μm$^3$ s$^{-1}$ | [162] |
| 4 | Focused Electron Beam Induced Deposition (FEBID) | Pt | 0.15-0.23 | 0.0002-0.0009 μm$^3$ s$^{-1}$ | [163] |
| 5 | Cryo-FEBID | Pt | 0.022-0.31 | 10 μm$^3$ s$^{-1}$ | [164] |
| 6 | Meniscus-confined electroplating | Cu | 12.0-15.0 | 0.18-0.4 μm s$^{-1}$ | [45] |
| 7 | Local electrophoretic deposition | Au | 0.5-2.0 | 0.30-0.67 μm s$^{-1}$ | [36] |
| 8 | This work | Ni | 0.025-0.4 | 4000-6000 μm s$^{-1}$ | |

*Volumetric (μm$^3$ s$^{-1}$) or linear (μm s$^{-1}$) writing speed is given when available

## APPENDIX D: SUPPLEMENTARY VIDEOS

The following supplementary videos are included.

**Supplementary Video 1**

Description: *In-situ* SEM video (played at 40x speed) of uniaxial compression of a nickel octet nanolattice with ~2 μm unit cells and 300-400 nm-diameter beams to ~85% strain. Elastic deformation (up to ~15% strain) is followed by layer-by-layer collapse (up to ~70% strain) and densification. The nanolattice does not recover after compression.

**Supplementary Video 2**

Description: *In-situ* video (optical) of uniaxial compression of a titania/carbon cubic lattice with unit cell size of $0.66 \pm 0.01$ mm and beam diameters of $170 \pm 5$ μm. Compression started with the sample settling into full contact followed by linear elastic regime up to 1-2% strain. Further compression resulted in gradual brittle failure of individual beams and unit cells.